

1 **Jet-Track Correlation Studies of the Quark Gluon Plasma**

2 BY

3 HALLIE CAUSEY TRAUGER

4 M.Ed. University of Illinois at Chicago, 2015

5 M.S. University of Illinois at Chicago, 2014

6 B.A. University of Chicago, 2010

7 THESIS

8 Submitted in partial fulfilment of the requirements

9 for the degree of Doctor of Philosophy in Physics

10 in the Graduate College of the University of Illinois at Chicago, 2017

11 Chicago, IL

12 DEFENSE COMMITTEE:

13 Olga Evdokimov, Chair and Advisor

14 David Hofman

15 Zhenyu Ye

16 Misha Stephanov

17 Julia Velkovska, Vanderbilt University

18

ACKNOWLEDGEMENTS

19 Thanks go here...

20

HCT

21

CONTRIBUTION OF AUTHORS

- 22 - Note previous publications (HIN-14-016, HIN-15-011, HIN-16-020)
- 23 - Describe CMS authorship policy
- 24 - Outline general CMS inputs (reconstruction etc.) that contributed to work
- 25 - Outline aspects that are my own work (and others' contributions to these as well, esp. Run 2)

CONTENTS

27	1 Introduction	1
28	2 The quark gluon plasma	2
29	2.1 Predictions and early evidence for the quark gluon plasma	2
30	2.2 Thermodynamics of the quark gluon plasma	4
31	2.3 Time-evolution of heavy ion collisions	5
32	2.4 Characterizing collision geometry and event centrality	7
33	2.5 Kinematic variables and coordinates	9
34	2.6 Collective behavior in the QGP	10
35	3 Jets as probes of the quark gluon plasma	13
36	3.1 Measuring suppression of high- p_T particles and jets	14
37	3.2 Jet fragmentation function and jet shape measurements	18
38	3.3 Dijet asymmetry and momentum balance studies	20
39	4 Models of jet energy loss in the quark gluon plasma	24
40	4.1 Survey of theoretical models of jet quenching mechanisms	24
41	4.2 Quenching model comparisons to high- p_T particle and jet observables	25
42	4.3 Theoretical motivations for detailed jet-track correlation studies	25
43	5 The Large Hadron Collider and the CMS detector	26
44	5.1 The Large Hadron Collider	26
45	5.2 The CMS detector	27
46	5.3 Trackers in the CMS detector	27
47	5.4 Calorimeters in the CMS detector	29
48	5.5 The CMS trigger system	30
49	6 Track reconstruction and correction	32
50	6.1 Track reconstruction in pp collisions	32
51	6.2 Track reconstruction in PbPb collisions	33
52	6.3 High purity tracks	34
53	6.4 Tracking efficiency and fake rate evaluation and correction	35
54	7 Jet reconstruction and correction	37
55	7.1 Jet reconstruction with the anti- k_t algorithm	37
56	7.2 Underlying event subtraction in PbPb data	39
57	7.3 Jet energy corrections	40
58	8 Data and Monte Carlo samples	42
59	8.1 Data samples and event selection	42
60	8.2 Collision centrality determination and classes	43
61	8.3 Monte Carlo simulation	44
62	8.4 Jet selection and dijet asymmetry classes	48
63	8.5 Track selection and classes	48
64	8.6 Summary of analysis bins	50

65	9 Jet-track correlation measurements	51
66	9.1 Analysis procedure	51
67	9.2 Jet-track correlation pair-acceptance correction	52
68	9.3 Separation of correlations into long range and short-range components	52
69	9.4 Residual Jet Fragmentation Function correction	56
70	9.5 Background fluctuation bias correction	60
71	9.6 Evaluation of systematic uncertainties	67
72	10 Discussion of results	71
73	10.1 Inclusive jet particle density correlation results	71
74	10.2 Dijet correlation results at 2.76 TeV	82
75	10.3 Jet shapes at 2.76 TeV and 5.02 TeV	91
76	10.4 Decomposition of hemisphere momentum balance in dijet events at 2.76 TeV	95
77	10.5 Theory implications of these results	107
78	11 Conclusion	108
79	References	109
80	Appendices	114
81	A Jet kinematics	114
82	B Background fitting details	128
83	C Pair acceptance and event decomposition systematic uncertainties	132
84	D Correlation widths and related uncertainty	134
85	Vita	138

LIST OF TABLES

87	I	Summary of data samples and number of selected events	42
88	II	Summary of Monte Carlo samples and generated events at 2.76 TeV	46
89	III	Summary of Monte Carlo samples and generated events at 5.02 TeV	47
90	IV	Summary of data selections and analysis bins	50
91	V	Systematic uncertainties for particle density correlation studies at 2.76 TeV	69
92	VI	Systematic uncertainties for particle density correlation studies at 5.02 TeV	69
93	VII	Systematic uncertainties for balanced and unbalanced dijets in transverse momentum distribution studies at 2.76 TeV	70
94			

LIST OF FIGURES

96	1	QCD coupling constant α_s	3
97	2	QCD phase diagram	6
98	3	Glauber model illustration	8
99	4	Dihadron correlation in $\Delta\eta - \Delta\phi$	11
100	5	Fits to dihadron $\Delta\phi$ distributions to extract flow coefficients	12
101	6	Flow coefficients v_2 and v_3 by centrality and p_T	12
102	7	Illustration of QCD cross section factorization	14
103	8	Charged particle R_{AA} at 200 GeV and 2.76 TeV	16
104	9	Charged particle R_{AA} at 2.76 and 5.02 TeV	16
105	10	Jet R_{AA} at 2.76 TeV	17
106	11	Jet fragmentation function in 2.76 TeV PbPb and pp data	18
107	12	Jet shape measurement in 2.76 TeV PbPb and pp data	19
108	13	Illustration of dijet asymmetry	20
109	14	Dijet asymmetry and in 2.76 TeV PbPb and pp data	21
110	15	Hemisphere p_T momentum balance in dijet events as a function of A_J	22
111	17	Model comparisons to charged particle R_{AA} at 5.02 TeV	25
112	18	CMS detector perspective drawing	28
113	19	Diagram of CMS trackers	29
114	20	Diagram of the HCAL	30
115	21	Tracking efficiency correction example	36
116	22	Closure with and without JFF-JEC for quark and gluon jets.	41
117	23	Centrality distribution for PYTHIA+HYDJET reweighted to match centrality distribution of PbPb data.	45
119	24	Vertex z distribution for PYTHIA+HYDJET reweighted to match centrality distribution of PbPb data.	45
120	25	Vertex z distribution for PYTHIA reweighted to match centrality distribution of pp data.	46
123	26	Illustration of the pair-acceptance correction procedure	53
124	27	Illustration of the event decomposition procedure without $\Delta\phi$ fitting	54
125	28	Illustration of the event decomposition procedure with $\Delta\phi$ fitting	55
126	29	Jet fragmentation function bias corrections for particles with $1 < p_T^{\text{trk}} < 2$ GeV	57
127	30	Jet fragmentation function bias corrections for particles with $2 < p_T^{\text{trk}} < 3$ GeV	57
128	31	Jet fragmentation function bias corrections for particles with $3 < p_T^{\text{trk}} < 4$ GeV	58
129	32	Jet fragmentation function bias corrections for particles with $4 < p_T^{\text{trk}} < 8$ GeV	58
130	33	Integrated yield attributed to jet fragmentation function bias as a function of p_T^{trk}	59
131	34	Integrated yield attributed to jet fragmentation function bias as a function of centrality	59
132	35	Background fluctuation bias corrections for particles with $1 < p_T^{\text{trk}} < 2$ GeV	61
133	36	Background fluctuation bias corrections for particles with $2 < p_T^{\text{trk}} < 3$ GeV	61
134	37	Background fluctuation bias corrections for particles with $3 < p_T^{\text{trk}} < 4$ GeV	62
135	38	Background fluctuation bias corrections for particles with $4 < p_T^{\text{trk}} < 8$ GeV	62
136	39	Integrated yield attributed to background fluctuation bias as a function of p_T^{trk}	63
137	40	Data-driven check of integrated yields attributed to background fluctuation bias	64
138	41	Data-driven check of correlated $\Delta\eta$ yields attributed to background fluctuation bias	65
139	42	Comparison of background selection bias effect for quark verus gluon jets	66
140	43	Inclusive jet $\Delta\eta$ correlations for tracks with $1 < p_T^{\text{trk}} < 2$ GeV at 2.76 TeV	72
141	44	Inclusive jet $\Delta\phi$ correlations for tracks with $1 < p_T^{\text{trk}} < 2$ GeV at 2.76 TeV	73

142	45	Inclusive jet $\Delta\eta$ correlations for tracks with $2 < p_T^{\text{trk}} < 3$ GeV at 2.76 TeV	74
143	46	Inclusive jet $\Delta\phi$ correlations for tracks with $2 < p_T^{\text{trk}} < 3$ GeV at 2.76 TeV	75
144	47	Inclusive jet $\Delta\eta$ correlations for tracks with $3 < p_T^{\text{trk}} < 4$ GeV at 2.76 TeV	76
145	48	Inclusive jet $\Delta\phi$ correlations for tracks with $3 < p_T^{\text{trk}} < 4$ GeV at 2.76 TeV	77
146	49	Inclusive jet $\Delta\eta$ correlations for tracks with $4 < p_T^{\text{trk}} < 8$ GeV at 2.76 TeV	78
147	50	Inclusive jet $\Delta\phi$ correlations for tracks with $4 < p_T^{\text{trk}} < 8$ GeV at 2.76 TeV	79
148	51	Inclusive jet $\Delta\eta$ correlations at 5.02 TeV	79
149	52	Inclusive jet $\Delta\phi$ correlations at 5.02 TeV	80
150	53	Inclusive jet distribution of charged particles as a function of Δr at 5.02 TeV	80
151	54	Integrated inclusive jet charged particle yields at 2.76 and 5.02 TeV	81
152	55	Dijet $\Delta\eta$ correlations for tracks with $1 < p_T^{\text{trk}} < 2$ GeV at 2.76 TeV	83
153	56	Dijet $\Delta\phi$ correlations for tracks with $1 < p_T^{\text{trk}} < 2$ GeV at 2.76 TeV	84
154	57	Integrated charged particle yields for inclusive, leading, and subleading jets	85
155	58	Leading jet $\Delta\eta$ correlation widths as a function of p_T^{trk} at 2.76 TeV	87
156	59	Leading jet $\Delta\phi$ correlation widths as a function of p_T^{trk} at 2.76 TeV	88
157	60	Subleading jet $\Delta\eta$ correlation widths as a function of p_T^{trk} at 2.76 TeV	89
158	61	Subleading jet $\Delta\phi$ correlation widths as a function of p_T^{trk} at 2.76 TeV	90
159	62	Inclusive jet shape at 5.02 TeV, shown differentially in p_T^{trk}	92
160	63	Leading jet shape at 2.76 TeV, shown differentially in p_T^{trk}	93
161	64	Subleading jet shape at 2.76 TeV, shown differentially in p_T^{trk}	94
162	65	Dijet subleading-to-leading hemisphere momentum balance for balanced dijets	97
163	66	Dijet subleading-to-leading hemisphere momentum balance for unbalanced dijets	98
164	67	Jet peak subleading-to-leading momentum balance for balanced dijets	99
165	68	Jet peak subleading-to-leading momentum balance for unbalanced dijets	100
166	69	long-range subleading-to-leading momentum balance for balanced dijets	102
167	70	long-range subleading-to-leading momentum balance for unbalanced dijets	103
168	71	Integrated transverse momentum in the long-range $\Delta\phi$ -correlated distribution as a function of track- p_T	104
169	72	Relative contributions from jet peaks and long-range asymmetry to the double difference PbPb–pp, subleading–leading in total hemisphere transverse momentum for central collisions	105
170	73	Relative contributions from jet peaks and long-range asymmetry to the double difference PbPb–pp, subleading–leading in total hemisphere transverse momentum for peripheral collisions	106
171	74	Distribution of transverse momentum, pseudorapidity, and azimuthal distribution of all jet selections for Pythia data compared to PYTHIA simulation.	114
172	75	Transverse momentum distribution of all jet selections for PbPb data at 2.76 TeV compared to PYTHIA+HYDJET simulation.	115
173	76	Pseudorapidity distribution of all jet selections for PbPb data at 2.76 TeV compared to PYTHIA+HYDJET simulation.	116
174	77	Azimuthal angle distribution of all jet selections for PbPb data at 2.76 TeV compared to PYTHIA+HYDJET simulation for each collision centrality bin.	117
175	78	Distribution of pseudorapidity distribution of all jet selections for PbPb data compared to PYTHIA+HYDJET simulation for each collision centrality bin.	118
176	79	Transverse momentum distribution for PbPb data compared to PYTHIA+HYDJET simulation for each collision centrality bin.	118
177	80	Jet η distribution for PbPb data compared to PYTHIA+HYDJET simulation for each collision centrality bin.	118

190	81	Jet ϕ distribution for PbPb data compared to PYTHIA+HYDJET simulation for each collision centrality bin.	119
191	82	Jet p_T , η , and ϕ for all pp dijets and for pp dijets with $A_J: 0 < A_J < 0.11$	120
192	83	Jet p_T , η , and ϕ for all pp dijets and for pp dijets with $A_J: 0.11 < A_J < 0.22$	121
193	84	Jet p_T , η , and ϕ for all pp dijets and for pp dijets with $A_J: 0.22 < A_J < 0.33$	122
194	85	Jet p_T , η , and ϕ for all pp dijets and for pp dijets with $A_J: A_J > 0.33$	123
195	86	Jet p_T , η , and ϕ for all PbPb dijets and for PbPb dijets with $0 < A_J < 0.11$	124
196	87	Jet p_T , η , and ϕ for all PbPb dijets and for PbPb dijets with $0.11 < A_J < 0.22$	125
197	88	Jet p_T , η , and ϕ for all PbPb dijets and for PbPb dijets with $0.22 < A_J < 0.33$	126
198	89	Jet p_T , η , and ϕ for all PbPb dijets and for PbPb dijets with $A_J > 0.33$	127
199	90	Dijet background fits (preliminary step)	128
200	91	Leading jet background fits	129
201	92	Subleading jet background fits	130
202	93	Inclusive jet background fits	131
203	94	Pair acceptance uncertainty determination	132
204	95	Background subtraction uncertainty determination	133
205	96	Width determination for PbPb leading jets	134
206	97	Width determination for pp leading jets	135
207	98	Width determination for PbPb subleading jets	136
208	99	Width determination for pp subleading jets	137

LIST OF ABBREVIATIONS

ADS/CFT	Anti-deSitter/Conformal Field Theory
AMPT	A Multiphase Transport Model
BNL	Brookhaven National Laboratory
CERN	Conseil Européen pour la Recherche Nucléaire
CMS	Compact Muon Solenoid
ECAL	Electromagnetic Calorimeter
E_T	Transverse Energy
HCAL	Hadronic Calorimeter
HF	Hadronic Forward
HLT	High Level Trigger
JEC	Jet Energy Correction
JES	Jet Energy Scale
JFF	Jet Fragmentation Function
LHC	Large Hadron Collider
MC	Monte Carlo
PbPb	Lead-lead (collision data)
PDF	Parton Distribution Function
pPb	Proton-lead (collision data)
pp	Proton-proton (collision data)
pQCD	Perturbative Quantum Chromodynamics
p_T	Transverse Momentum
QCD	Quantum Chromodynamics
QGP	Quark Gluon Plasma
RHIC	Relativistic Heavy Ion Collider
UE	Underlying Event
UrQMD	Ultrarelativistic Quantum Molecular Dynamics

SUMMARY

1 INTRODUCTION

2 THE QUARK GLUON PLASMA

214 2.1 Predictions and early evidence for the quark gluon plasma

215 Quantum chromodynamics (QCD) describes the interactions of the quarks and gluons (together
 216 known as partons) via the strong nuclear force. The strength of the QCD interactions, described
 217 by the QCD coupling constant $\alpha_s(Q)$ decreases as distances between strongly interacting partons
 218 decreases and their exchanged momentum Q :

$$\alpha_s(Q) \propto \frac{1}{\ln(\frac{Q^2}{\Lambda_{QCD}})}, \quad (1)$$

219 where $\Lambda_{QCD} \approx 0.2$ GeV gives the QCD scale. Figure 1 shows the dependence of α_s on momentum
 220 scale Q . In the regime where separations between partons are relatively large (small Q), α_s is large,
 221 leading to the observed confinement of quarks and gluons in composite particles called hadrons, most
 222 commonly baryons (comprised of 3 quarks, including protons and neutrons) and mesons (comprised
 223 of 2 quarks). In the large Q regime, however—accessed via large baryon chemical potential μ_B or
 224 large temperature T —the strength of the coupling constant α_s decreases, in a phenomenon known as
 225 asymptotic freedom. Asymptotic freedom both permits the accurate approximation of high-energy
 226 hadron interactions using perturbation theory (pQCD), and implies the deconfinement of quarks
 227 and gluons. This phase of deconfined quarks and gluons, known as the quark gluon plasma (QGP),
 228 was originally conceived as a gas of color-charged quarks and gluons, analogous to the plasma of
 229 photons and electrons previously studied in quantum electrodynamics. In collider studies, this
 230 suggests the possibility of a phase transition anticipated between the hadron gas phase present
 231 under ordinary matter conditions, and the QGP phase present at sufficiently great μ_B or T [1, 2].

232 In the early 1980s, relativistic nuclear collisions were suggested as a means of producing
 233 sufficient temperatures and densities to induce a quark-gluon plasma and probe the transition
 234 between the QGP and ordinary matter. Efforts were also made to anticipate key experimental
 235 signatures of the short-lived possible QGP, relying in many cases on the anticipation that the QGP
 236 would behave according to a hydrodynamic description of a system in at least partial thermal
 237 equilibrium. Proposed signatures included enhancements of strange (heavy) quarks, unusual event
 238 structures, greater rates of direct dilepton and photon production [4]. The first heavy ion collisions

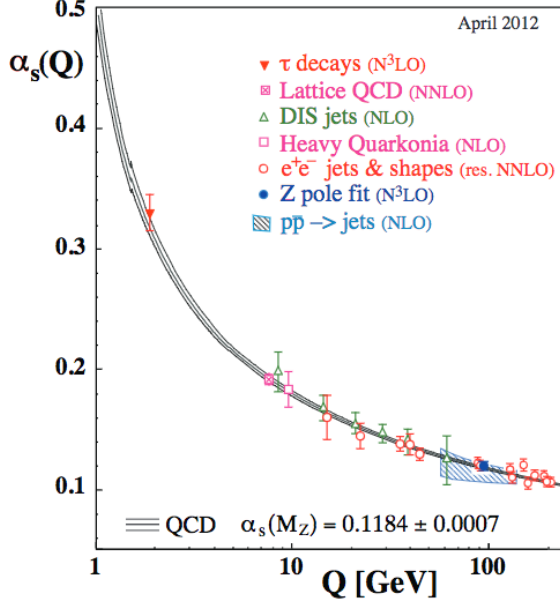


Figure 1. Momentum scale dependence of QCD coupling constant α_s , from Ref. [3].

began with fixed-target experiments at the Super Proton Synchrotron (SPS) at CERN in the mid-1980s, colliding nuclei including gold and lead at energies from 40 GeV to 160 GeV through the 1990s. Analysis of the hadron yields in these collisions showed an apparent chemical equilibrium of quarks and gluons at about 170 MeV and enhancement (as anticipated) both of strangeness (via kaon/pion ratios, and J/ψ production rates). In the early 2000, a CERN press release cited these results in declaring that “a common assessment of the collected data leads us to believe that a new state of matter has indeed been created...[that] features many of the characteristics of the theoretically predicted quark-gluon plasma” [5].

Shortly after the SPS announcement, the first gold-gold collisions began at the Relativistic Heavy Ion Collider (RHIC) at Brookhaven National Laboratory, beginning an era of high-energy heavy ion collisions that would later be complimented by a parallel program at the Large Hadron Collider at CERN. Through data collection and analysis by experiments at each of these colliders over the ensuing nearly two decades, the field has gradually shifted from searches for signatures of QGP formation in heavy ion collisions, to detailed characterizations of its properties and evolution. In 2005, the four experimental collaborations at RHIC (BRAHAMS, PHENIX, PHOBOS, and STAR) published coordinated white papers [6, 7, 8, 9] summarizing the assembled evidence that

255 results from gold-gold collisions could not be explained by models of ordinary hadronic matter–
 256 most notably in signatures of collective behavior (see Sec. 2.6) and in suppression of particles with
 257 relatively high transverse momentum (see Sec. 3). Beginning in 2010, heavy ion studies at the LHC
 258 by the ALICE, ATLAS, and CMS Collaborations (and more recently by the LHCb Collaboration)
 259 have complimented the RHIC access to a wide range of center-of-mass-energies in the 7.7 GeV to
 260 200 GeV range with measurements at 2.76 TeV and 5.02 TeV.

261 2.2 Thermodynamics of the quark gluon plasma

262 The existence of a plasma phase of hadronic matter and a number of the properties of this phase can
 263 also be inferred directly from thermodynamic considerations of hadronic matter. In free space, the
 264 density of states of hadrons as a function of resonance mass m increases exponentially, following
 265 the Hagedorn spectrum

$$\rho(m) = m^{\frac{5}{2}} e^{\frac{m}{T_0}}, \quad (2)$$

266 where $T_0 \approx m_\pi \approx 140$ MeV. [10, 11]. When taking into account the finite size of hadrons (with
 267 radii on the order of 1 fm), this suggests an upper limit or critical temperature $T_c \approx 150 - 200$
 268 MeV above which quark and gluon deconfinement occurs. The pressure and energy density of
 269 this plasma phase are both, to first order in the ideal gas, proportional to T^4 , with higher order
 270 corrections introduced by the non-zero effective (“thermal”) quark and gluon masses. Defining
 271 a color-dependent constant c and a “bag pressure” B (named after the MIT model of hadrons
 272 as “bags” of quarks and gluons) that takes into account the difference between quark and gluon
 273 ground states and the vacuum, pressure may be expressed to first order as:

$$P = cT^4 - B, \quad (3)$$

274 and energy density ϵ may be expressed to first order as:

$$\epsilon = 3cT^4 + B. \quad (4)$$

275 Interaction effects due differences between the ground state and the vacuum may be captured by
276 “interaction measure” $\Delta = (\epsilon - 3P)/T^4$. Lattice QCD studies show a sharp rise in energy density
277 from the low-density hadronic state at the critical temperature T_c , saturating to constant values
278 at larger T . These values are about 10% less than those expected for an ideal massless gas due
279 to the higher order thermal mass corrections. The interaction measure remains non-zero above
280 T_c , indicative of differences between the vacuum and the QCD ground state or possibly of color
281 resonance states in the QGP. [11, 12]

282 Figure 2 gives a schematic illustration of the QCD phase diagram as a function of baryon
283 chemical potential and temperature based on thermodynamic considerations and lattice QCD stud-
284 ies. While chiral symmetry is spontaneously broken for non-zero quark masses, asymptotic freedom
285 implies chiral symmetry at sufficiently large temperatures and a phase transition between the two
286 (hadronic and quark gluon plasma) phases, which is first-order at sufficiently large μ_B with sin-
287 gularities in thermodynamic functions. Below a certain critical point value of μ_B (and at critical
288 temperature T_c), however, the transition is a cross-over without singular behavior, and lattice
289 QCD simulations have demonstrated such cross-over behavior for the limit $\mu_B = 0$. This suggests
290 the existence of a tricritical point on the phase boundary between confined and deconfined QCD
291 phases. [11, 12, 13] The beam energy scan program at RHIC probes center-of-mass energies ranging
292 from 7.2 to 200 GeV to probe temperatures around the predicted values for T_c ; at LHC energies
293 2.76 TeV and 5.5 TeV initial QGP temperatures are estimated in the 300 - 700 MeV range, well
294 above the critical temperature. [14]

295 2.3 Time-evolution of heavy ion collisions

296 Connecting predictions and simulations of QGP behavior to experimental results requires the de-
297 scription and analysis of several different sequential phases of heavy ion collisions [11, 15]:

298 1. **Initial state** – Nuclei A and B (lorentz-contracted into two flat discs) approach each other
299 with impact parameter b and nucleon distributions $\rho_A(r)$ and $\rho_B(r)$, establishing a set of
300 initial conditions with implications for the later evolution of the medium.

301 2. **Pre-equilibrium** – Initially after nuclei collide (before thermalization time τ_0), nucleons
302 interact dynamically as the QGP begins to form. Various models – including IP-Glasma,

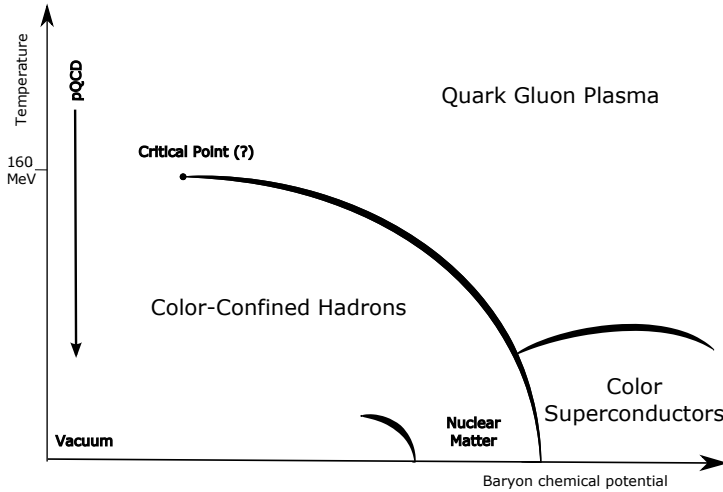


Figure 2. Schematic phase diagram of strongly interacting matter as a function of baryon chemical potential μ_B and temperature T .

303 A Multiphase Transport Model (AMPT), Ultrarelativistic Quantum Molecular Dynamics
 304 (UrQMD), and models based on the Anti-deSitter/Conformal Field Theory (ADS/CFT) cor-
 305 respondence – attempt to capture these dynamics.

306 3. **Hydrodynamic expansion** – After thermalization time τ_0 local thermodynamic equilib-
 307 rium is achieved, producing an expanding medium whose properties can be described with
 308 ideal fluid dynamics with sheer viscosity to energy-density ratio $\eta/s \approx 1.6$ at RHIC and the
 309 LHC [16].

310 4. **Hadronization (“freeze-out”)** – Quarks and gluons recombine into hadrons in the phase
 311 transition back from deconfined to confined QCD matter. As the medium expands, it reaches
 312 sufficiently low densities and temperatures that thermal equilibrium is lost, and quark and
 313 gluon recombination stops. Chemical freeze-out occurs when particle number changing pro-
 314 cesses end; kinetic freeze-out occurs later, when the ratio of the expansion rate to the collision
 315 rate among particles drops to the point that collisions no longer occur.

316 5. **Free-streaming** – recombined hadrons move through the beam pipe vacuum and are mea-
 317 sured by the detector. Experimental results can only directly access these final distributions
 318 of particles, from which inferences are made about the other collision stages.

319 Each stage of this QGP time evolution may be accessed via various experimental observables.
320 Vacuum-like hadronization is well-modeled by parton shower simulations in Monte Carlo genera-
321 tors such as PYTHIA and HERWIG that capture proton-proton collision dynamics. Heavy ion colli-
322 sions, however, present the challenge of defining a freeze-out hypersurface at which hydrodynamic
323 evolution terminates, and hadronization begins. This hypersurface occurs at the phase transition
324 boundary, and may be experimentally accessed via the yields of hadron species in the final state
325 (as particle numbers do not change during the free-streaming stage) [11]. Initial collision geometry
326 may be described via Glauber Models and nuclear parton distribution functions (PDFs) of the
327 incoming partons, as discussed in Sec. 2.4. Signatures of initial collision anisotropy and collective
328 hydrodynamic evolution may be observed as “collective flow” via particle correlations (Sec. 2.6).
329 Pre-equilibrium dynamics are particularly difficult to access, but probes including the medium mod-
330 ifications to high- p_T jets presented in this analysis provide possibilities for distinguishing between
331 the different theoretical models.

332 2.4 Characterizing collision geometry and event centrality

333 In heavy ion events there is a wide range of possible collision geometries: at one extreme the nuclei
334 may collide head-on (referred to as a “central” collision, with impact parameter $b = 0$), while at
335 the other they may barely graze each other (referred to as a “peripheral” collision). The initial
336 geometry, size, and evolution of the QGP formed in these events may vary considerably based on
337 these initial collisions. At the most basic level, events may vary in both the number of participating
338 nucleons (N_{part}), and in the number of binary nucleon-nucleon collisions (N_{coll}) occurring in the
339 event. While it is not possible to directly measure b , N_{part} , or N_{coll} in a heavy ion experiment, it is
340 possible to measure the total energy deposited in calorimeters at very forward rapidities along the
341 beam line direction. The total energy deposited in these forward calorimeters is directly related to
342 the number of “spectator” nucleons that do not collide in the event, and therefore inversely related
343 to N_{part} . By dividing the total experimental event sample into “centrality classes” (ranging from
344 0% “most central” to 100% “most peripheral”) by total energy deposited at forward rapidity and
345 mapping this classification to a simulated sample, it is possible to map events to Monte Carlo
346 simulation and extract mean values for N_{part} and N_{coll} [17].

347 Glauber Models allow for the characterization of event parameters based on modeling of
 348 collision geometry. In the simplest “optical limit” of such models, it is assumed that individual
 349 nucleons accelerated to very high momenta move relatively independently and linearly, and deflec-
 350 tion and shadowing effects are neglected. These assumptions reduce the problem to one of only
 351 collision geometry, take the inelastic nucleon-nucleon cross-section $\sigma_{NN}^{\text{inel}}$ and the density of nucleons
 352 in each colliding nucleus $\rho_A(r)$ and $\rho_B(r)$ to calculate a “nuclear overlap function” T_{AB} , defined as:

$$T_{AB} = \int d^2\vec{s} \int dz_A \rho_A(\vec{s}, z_A) \int dz_B \rho_B(\vec{s} - \vec{b}, z_B), \quad (5)$$

353 where the integrals $\int dz_A \rho_A(\vec{s}, z_A)$ and $\int dz_B \rho_B(\vec{s} - \vec{b}, z_B)$ define the probability of finding a nucleon
 354 at locations (\vec{s}, z_A) and $(\vec{s} - \vec{b}, z_B)$, respectively with the geometry shown in Fig. 3.

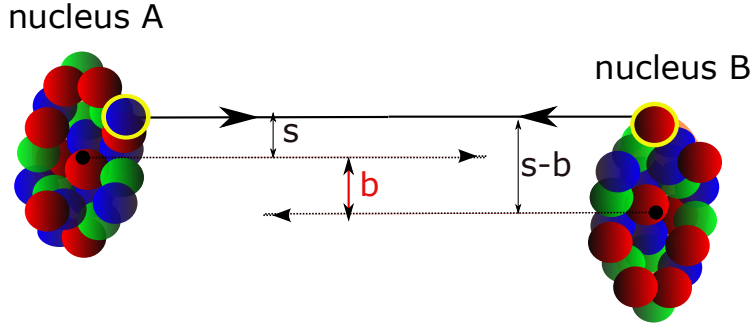


Figure 3. Schematic illustration of Glauber Model geometry for a nucleus-nucleus collision, showing impact parameter \vec{b} between the two nuclei and locations of two representative colliding nuclei.

355 The resulting total number of collisions is then given by:

$$N_{\text{coll}}(b) = \sigma_{NN}^{\text{inel}} T_{AB}(b). \quad (6)$$

356 For example for minimum bias collisions at LHC energy 2.76 TeV $\sigma_{NN} = 65$ mb, $\sigma_{PbPb} = 7660$
 357 mb, $\langle T_{PbPb} \rangle = \int d^2b T_{PbPb} / \int d^2b = 5.65 \text{ mb}^{-1}$, and $\langle N_{\text{coll}}(b) \rangle = 367$ [17, 18]. The optical limit
 358 calculations described above are able to reasonably capture collision parameters, but are limited
 359 by their neglect of effects including nuclear shadowing and diffraction. Glauber Monte Carlo sim-
 360 ulations are able to re-introduce some of these effects, thereby better capturing the nuclear cross
 361 section [17, 19].

362 **2.5 Kinematic variables and coordinates**

363 In high-energy colliders the z axis is defined parallel to the colliding beams, with x and y axes
364 spanning a transverse plane perpendicular to the beam axis. Because the colliding nuclei are
365 accelerated to nearly the speed of light, it is necessary to use relativistic coordinates starting from
366 the energy-momentum relationship:

$$E^2 = p_x^2 c^2 + p_y^2 c^2 + p_z^2 c^2 + M^2 c^4 \quad (7)$$

367 for a particle with rest mass M . The azimuthal coordinate in the transverse plane is then simply
368 given by:

$$\phi = \tan^{-1} \left(\frac{p_y}{p_x} \right) \quad (8)$$

369 With incoming particles colliding with very large p_z , the outgoing direction of collision products is
370 characterized by their rapidity y , a generalization of velocity defined by:

$$y = \ln \sqrt{\frac{E + p_z c}{E - p_z}}, \quad (9)$$

371 The rapidity is defined such that particles which emerge perpendicular to the beam axis (with
372 $p_z = 0$) have $y = 0$, while $y \rightarrow \infty$ toward the beam line. In practice, however, the outgoing
373 particle's rest mass M and energy E are generally unknown, while the total momentum \vec{p} can be
374 measured in detectors. In ultrarelativistic collisions, where $\vec{p}^2 \gg M^2 c^2$, we instead measure the
375 pseudorapidity η defined by:

$$\eta = \ln \left(\frac{|\vec{p}| + p_z}{|\vec{p}| - p_z} \right) \quad (10)$$

376 Pseudorapidity may also be calculated from the polar angle θ with respect to the beam pipe,

$$\eta = -\ln \left(\tan \left(\frac{\theta}{2} \right) \right) \quad (11)$$

377 As is clear from this representation, particles perpendicular to the beampipe with $\theta = \pi/2$ corre-
378 spond to rapidity $\eta = 0$, while particles with $\theta = \pi/4$ correspond to $\eta \approx 0.88$.

379 In general throughout this document, energies and measurements are presented in natural
 380 units with $\hbar = c = 1$ (momenta, for example, are given in MeV or GeV rather than MeV/c or
 381 GeV/c). Azimuthal angle ϕ is measured in radians.

382 **2.6 Collective behavior in the QGP**

383 In any nucleus-nucleus collision, the initial collision region will exhibit some azimuthal anisotropy—
 384 both due to the elliptical overlap region for collisions with impact parameter $b > 0$, and due to local
 385 variations in the nuclear densities ρ_A and ρ_B . As the medium thermalizes and hydrodynamically
 386 expands, this spatial anisotropy translates into anisotropy in momentum space or “collective flow”
 387 of the expanding medium. This correlation is retained through the hadronization and free-streaming
 388 phases, and is ultimately detectable via modulation in the distribution of particles with respect to
 389 the reaction plane (ψ_{RP} , the plane spanned by the impact parameter \vec{b} and the beam direction).
 390 This may be expanded in a Fourier series,

$$\frac{dN}{d\phi} = \frac{N}{2\pi} \left(1 + 2 \sum_n v_n \cos(n(\phi - \psi_{RP})) \right), \quad (12)$$

391 using Fourier coefficients v_1 , v_2 , v_3 , etc. (sometimes referred to as “harmonic flow coefficients”)
 392 to model the $\Delta\phi$ correlation between particles and the reaction plane. These coefficients may be
 393 interpreted as corresponding to different geometric anisotropies in the initial state: v_1 refers to
 394 “directed flow” which arises as colliding nucleons are repelled perpendicular to the beam direction
 395 in the reaction plane. Elliptic flow coefficient v_2 refers to the elliptical anisotropy arising from the
 396 overlap of two roughly circular nuclei, while v_3 (“triangular flow”) and higher coefficients refer to
 397 more complex initial geometries arising from fluctuations in the nucleon densities [20].

398 The azimuthal direction of the reaction plane ψ_{RP} cannot be directly experimentally mea-
 399 sured, but may be estimated based on event-by-event particle distributions in the detector. Al-
 400 ternatively, flow may be measured by considering two-particle correlations measuring $\Delta\phi_{\text{trig,assoc}}$
 401 between trigger and associated particles. In this case, the Fourier decomposition of the $\Delta\phi_{\text{trig,assoc}}$
 402 distribution becomes

$$\frac{1}{N_{\text{trig}}} \frac{dN^{\text{pair}}}{d\Delta\phi_{\text{trig,assoc}}} = \frac{N_{\text{assoc}}}{2\pi} \left(1 + 2 \sum_n V_n \cos(n(\Delta\phi_{\text{trig,assoc}})) \right), \quad (13)$$

403 Here the combined flow coefficients V_n are found to be factorizable into coefficients for the trigger
 404 and associated hadrons, i.e. $V_n = v_{n,\text{trig}} \times v_{n,\text{assoc}}$ [21, 22]. To measure collective flow through this
 405 two-particle method, two dimensional correlations in $\Delta\eta - \Delta\phi$ are constructed between trigger and
 406 associated hadrons, as shown in Fig. 4 from CMS study [22]. These distributions are projected over
 407 the large $\Delta\eta$ region (in this case $|\Delta\eta| < 2$ to capture long range correlations, and are fit in $\Delta\phi$ with
 408 the Fourier function shown above to extract flow coefficients V_1 , V_2 , and V_3 , from which v_1 , v_2 , and
 409 v_3 may be calculated. These studies find centrality- and p_T -dependent flow coefficients through v_3 ,
 410 with v_3 present substantially smaller than v_2 . As expected from simple geometrical considerations,
 411 values of v_2 and v_3 are greatest for mid-central collisions in which collision anisotropy is greatest,
 412 and peak as a function of p_T in the 2-3 GeV range, as shown in Fig. 6.

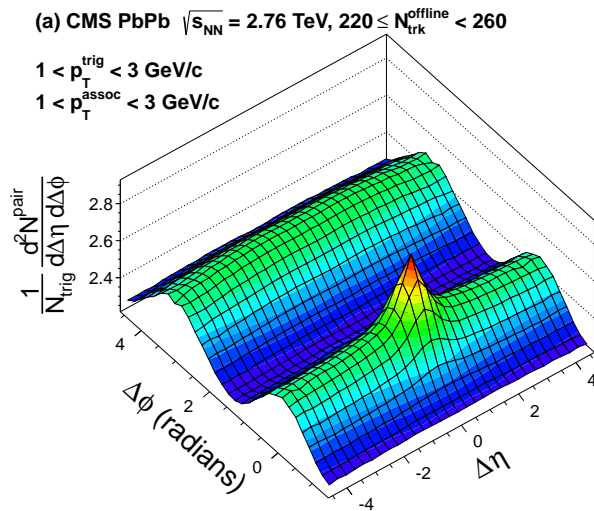


Figure 4. Illustration of dihadron correlation in $\Delta\eta - \Delta\phi$ for $1 < p_T^{\text{trig}} < 3$ GeV and $1 < p_T^{\text{assoc}} < 3$ GeV in central PbPb collisions at 2.76 TeV from Ref. [22]

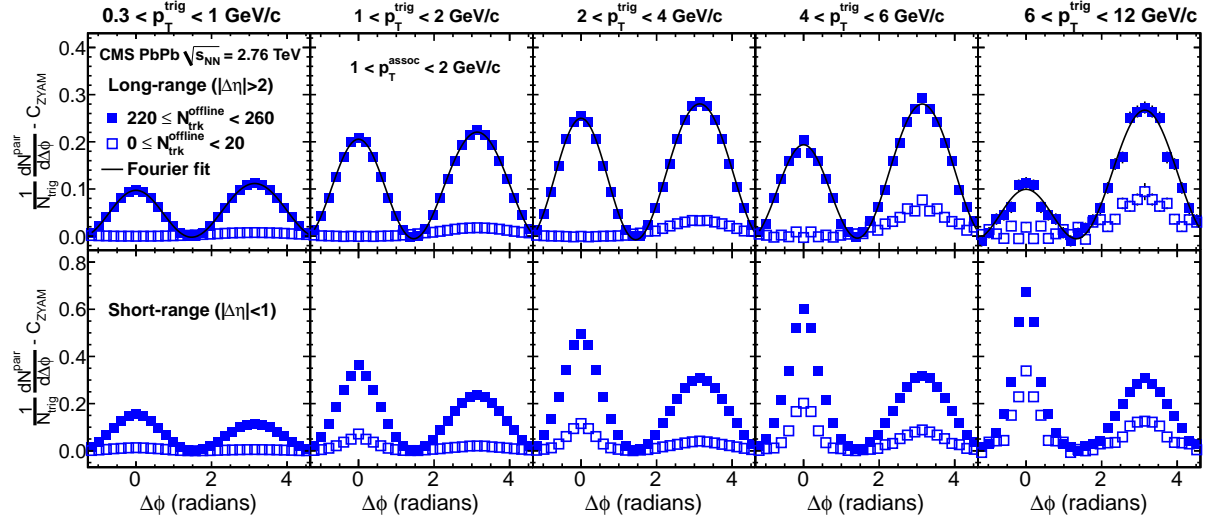


Figure 5. Fourier fits to dihadron $\Delta\phi$ distributions for $1 < p_T^{\text{assoc}} < 2$ GeV as a function of p_T^{trig} in central PbPb collisions at 2.76 TeV from Ref. [22]

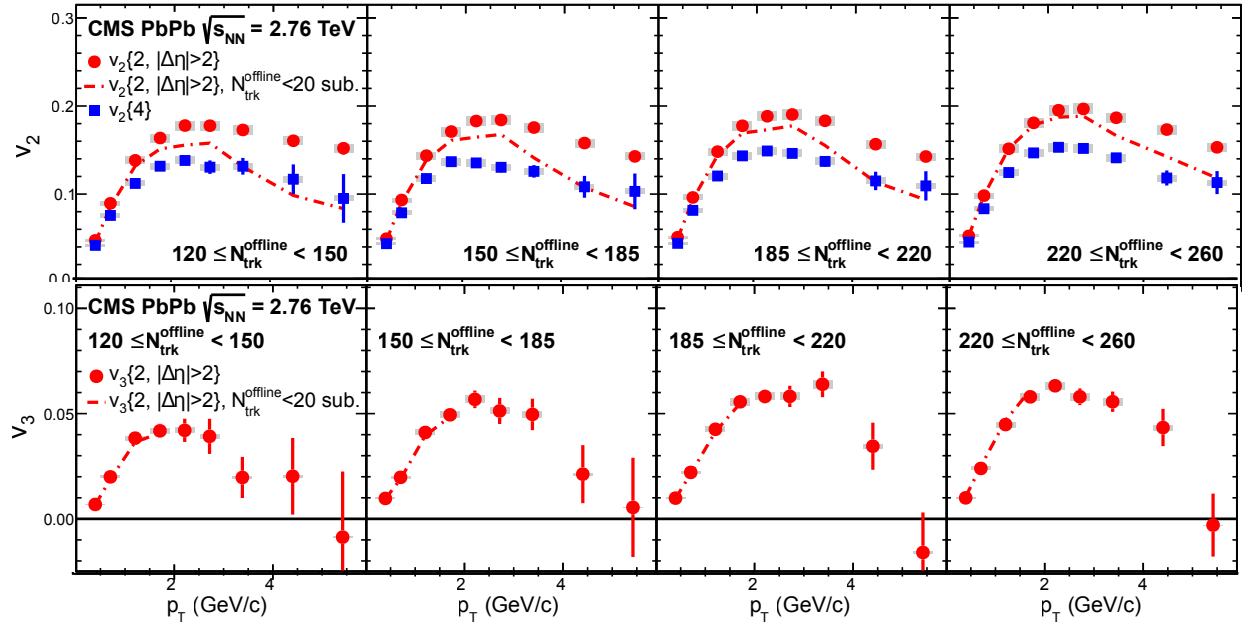


Figure 6. Flow coefficients v_2 and v_3 by centrality and p_T at 2.76 TeV from Ref. [22]

3 JETS AS PROBES OF THE QUARK GLUON PLASMA

414 Hard scatterings in heavy ion collisions can provide powerful probes of the quark gluon plasma.
 415 Because of asymptotic freedom, high-energy parton-parton processes can be accurately character-
 416 ized via pQCD, and have been thoroughly studied experimentally in hadron-hadron collisions. In
 417 heavy ion collisions, the initial parton-parton interaction should by causality behave the same as a
 418 parton-parton interaction in hadron-hadron collisions. After the collision, however, outgoing par-
 419 tons traverse the quark gluon plasma, providing the opportunity to study medium properties by
 420 comparing heavy ion results to expectations inferred from hadron-hadron “vacuum” reference data.
 421 These studies are facilitated by the “factorization theorem” in pQCD, which states that the cross
 422 section $\sigma_{AB \rightarrow h}^{\text{hard}}$ of hadron h produced in the hard process $A + B \rightarrow h$) can be decomposed into
 423 contributions from:

- 424 • The perturbative cross section of the parton hard scattering $\sigma_{ab \rightarrow c}^{\text{hard}}$
- 425 • The initial parton distribution functions (PDFs) of partons in the colliding nuclei A and B
 426 ($f_{a/A}$ and $f_{b/B}$ for partons of flavor a and b)
- 427 • The fragmentation function $\mathcal{D}_{c \rightarrow h}$ describing the probability that parton c fragments into
 428 hadron h with momentum fraction $z = p_h/p_c$

429 The total cross section may be represented, schematically, as:

$$d\sigma_{AB \rightarrow h}^{\text{hard}} = f_{a/A}(x_a, Q^2) f_{b/B}(x_b, Q^2) \times d\sigma_{ab \rightarrow c}^{\text{hard}}(x_a, x_b, Q^2) \times \mathcal{D}_{c \rightarrow h}(z, Q^2), \quad (14)$$

430 Each contribution to $d\sigma_{AB \rightarrow h}$ can be experimentally determined, and in hadron-hadron collisions
 431 $\sigma_{ab \rightarrow c}^{\text{hard}}$, fragmentation functions, and PDFs should each be universal. Figure 7 illustrates this
 432 factorization for hard-scattering interaction $A + B \rightarrow h$.

433 The partonic cross section $\sigma_{ab \rightarrow c}^{\text{hard}}$ furthermore should not, by causality, depend on the pres-
 434 ence or absence of the QGP. Medium modifications may enter at two phases in this process: first,
 435 via energy loss by parton c passing through the medium, and second via possible medium-induced
 436 changes to fragmentation functions $\mathcal{D}_{c \rightarrow h}$. Parton energy loss is attributed to two primary mech-
 437 anisms: collisional energy loss from scatterings with partons in the medium, and medium induced

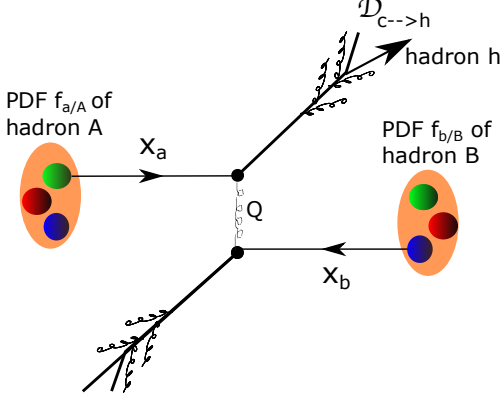


Figure 7. Illustration of the QCD hard-scattering $A + B \rightarrow h$.

438 radiation roughly analogous to electromagnetic ionization in a medium [23, 24]. This medium-
439 induced parton energy loss implies an observable reduction of medium properties can also be fur-
440 ther probed by comparing measurements of jet substructure in heavy ion collisions compared to pp
441 reference data (Sec. 3.2), and by studying modifications to p_T balance in back-to-back dijet events
442 (Sec. 3.3).

443 3.1 Measuring suppression of high- p_T particles and jets

444 One observable to probe parton energy loss in the medium is to compare yields of both particles
445 with relatively high transverse momentum (p_T), and of reconstructed jets (collections of particles
446 clustered in an effort to reconstruct the original parton energy – see Sec. 7). This reduction in jet
447 yields compared to expectations from “vacuum” reference or scaled binary collisions can be studied
448 as both a signature of the presence of the QGP, and an observable to distinguish between models
449 of interactions within the QGP (see Sec. 3.1).

450 Since by pQCD factorization the partonic cross-section $\sigma_{ab \rightarrow c}$ should be independent, in the
451 absence of the quark gluon plasma, the nuclear inclusive cross section would be expected to scale
452 with the number of participating nucleons, i.e.

$$d\sigma_{AB \rightarrow h}^{\text{hard}}(b) = \langle T_{AB}(b) \rangle \sigma_{pp}^{\text{hard}} \quad (15)$$

453 where $T_{AB}(b)$ parameterizes the probability of nucleon-nucleon interactions for a given impact
454 parameter for nuclei A and B colliding with impact parameter b as discussed in Sec. 2.4. A com-

455 parison of actual hadron (or jet) yields compared to this expectation can therefore give information
 456 about parton interactions with the medium, as characterized by the nuclear modification factor
 457 R_{AA} defined as the ratio of the observed yield in heavy ion data to the expecation from binary
 458 scaled pp data:

$$R_{AA}(p_T, \eta) = \frac{d^2\sigma_{AA}/dp_T d\eta}{\langle T_{AB}(b) \rangle d^2\sigma_{pp}/dp_T d\eta} \quad (16)$$

459 Consistent with quenching expectations, RHIC measurements of R_{AA} in gold-gold collisions
 460 showed substantial suppression of a factor of 70-80% for $p_T > 4$ GeV [6, 7, 8, 9]. Comparisons of
 461 RHIC measurements to early LHC results showed similar qualitative features, but greater suppres-
 462 sion at low- p_T at the LHC, despite the more slowly falling pp spectrum at the LHC, as shown in
 463 Fig. 8. Measurements at the LHC have also found that R_{AA} rises with p_T for charged particles with
 464 $p_T > 7$ GeV, and have shown no significant center-of-mass energy differences when comparing R_{AA}
 465 at 2.76 TeV and 5.02 TeV, as shown in Fig. 9. The p_T dependence of R_{AA} is generally driven by
 466 three factors: the kinematic constraints on jet energy loss (model-specific details will be discussed
 467 in Sec. 4), the fact that R_{AA} takes the ratio of two steeply falling spectra the scattered partons, one
 468 shifted by energy loss and one un-shifted, and the effects of nuclear shadowing and anti-shadowing
 469 in the nuclear PDFs [24, 25].

470 Studies of high- p_T tracks make use of the fact that such tracks are likely to originate from
 471 outgoing partons in hard-scattering interactions, providing an indirect look at energy loss by the
 472 parton used as a probe of the QGP. To more directly reconstruct parton energy, we may instead
 473 consider reconstructed jets, defined as the collection of (spatially grouped) particles resulting from
 474 the fragmentation of a high- p_T quark or gluon. Jet reconstruction, described in detail in Sec. 7,
 475 groups detector deposits to reconstruct a jet energy, and uses Monte Carlo simulation to reconstruct
 476 a “true” jet energy of the original parton. Quenching studies with reconstructed jets therefore can
 477 offer a more direct look at energy loss in the medium by comparing measured energy in jets in
 478 heavy ion collisions to those in proton-proton collisions. Measurements of jet R_{AA} at the LHC
 479 reported in Refs. [28, 29] show suppression by a factor of approximately 40-60% in most central
 480 PbPb collisions, with weak depenence on jet p_T as shown in Fig. 10.

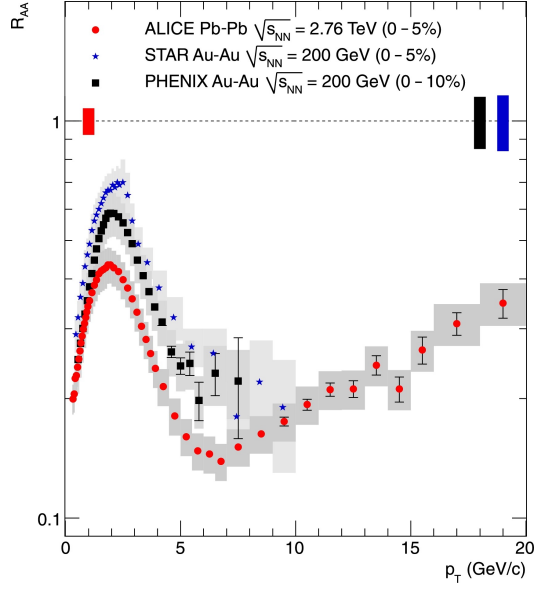


Figure 8. Measurements of charged particle R_{AA} from the STAR and PHENIX Collaborations at 200 GeV at RHIC, compared to ALICE results from the LHC at 2.76 TeV from Ref. [26].

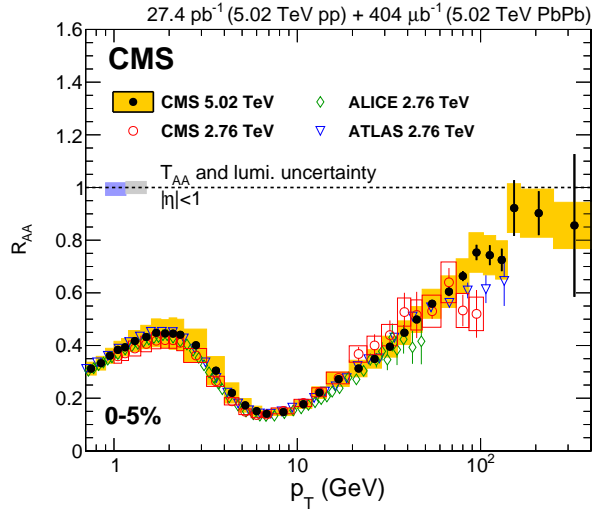


Figure 9. Measurements of charged particle R_{AA} at LHC energies 2.76 TeV and 5.02 TeV from Ref. [27].

481 Jet R_{AA} measurements capture parton energy loss by measuring the reduction in yields in
 482 the presence of the QGP. To connect jet R_{AA} to charged particle R_{AA} measurements, it is necessary
 483 to also consider trends in jet fragmentation patterns with jet- p_T . High- p_T jets are more likely to
 484 originate from quarks than from gluons, and therefore exhibit “harder” fragmentation patterns—

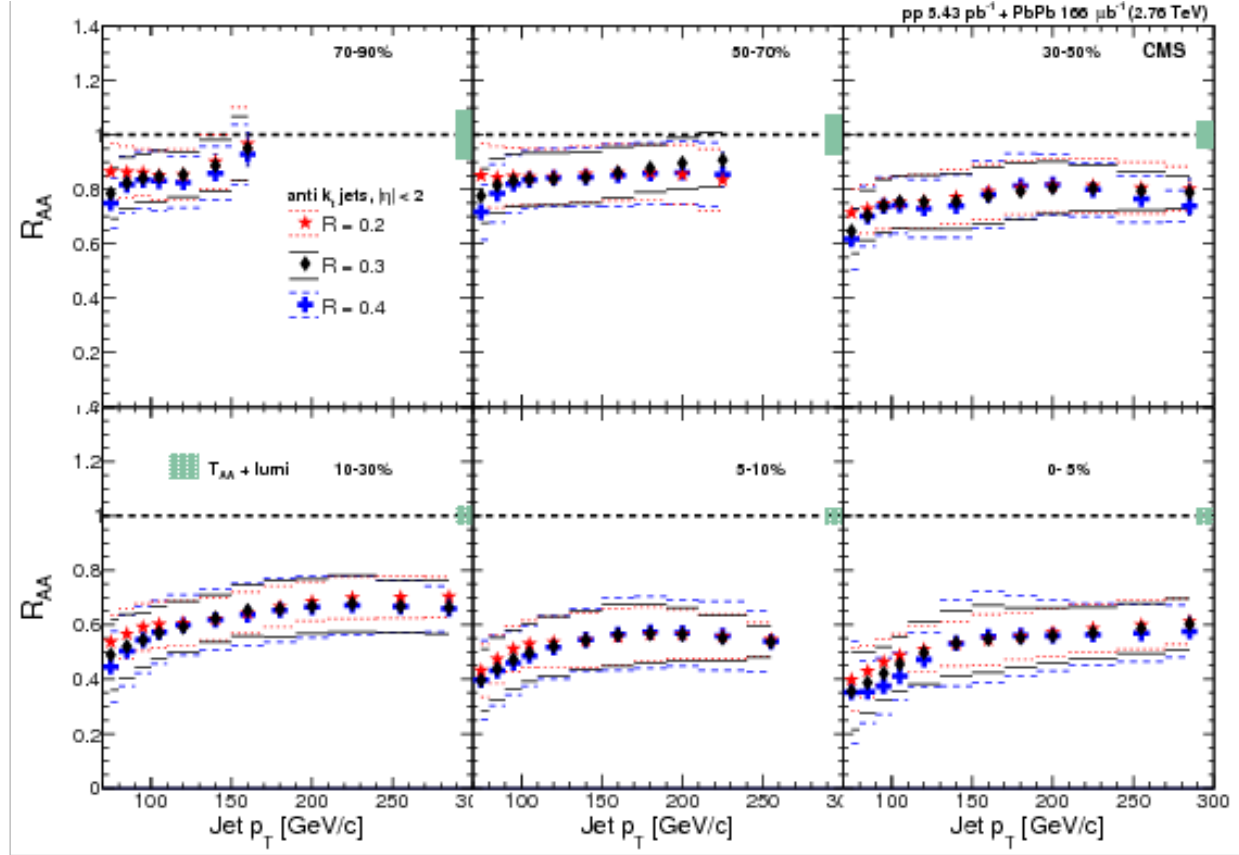


Figure 10. Jet R_{AA} at 2.76 TeV from Ref. [29].

i.e. higher- p_T jets fragment into relatively fewer particles each with more p_T compared to jets at lower- p_T . Jets with softer fragmentation are also expected to exhibit greater modification in the QGP, as low- p_T fragmentation products rescatter in the medium. The highest- p_T tracks, for which R_{AA} is the smallest, are associated with those jets that have not only the highest- p_T , but also the hardest fragmentation. The high- p_T sector of jet R_{AA} measurements at LHC energies, however, still includes significant contributions from jets reconstructed from softer particles that exhibit significant suppression.

492 **3.2 Jet fragmentation function and jet shape measurements**

493 Measurements of jet R_{AA} quantify the overall reduction in numbers of high- p_T jets passing a certain
 494 momentum threshold, providing an indication of the magnitude of jet energy loss in different p_T
 495 regions. As discussed above, this measurement can constrain the possible mechanisms of jet energy
 496 loss. To further constrain models of jet energy loss, additional observables aim to capture the details
 497 of jet fragmentation and its modification in the quark gluon plasma. One such measurement is the
 498 jet fragmentation function, which captures the p_T distribution of tracks carrying jet momentum,
 499 parameterized via the variables z and ζ :

$$z = \frac{p_{||}^{\text{track}}}{p_{||}^{\text{jet}}}, \zeta = \frac{1}{\ln(z)}, \quad (17)$$

500 where $p_{||}^{\text{track}}$ refers to the component of the track p_T along the jet axis. Jet fragmentation function
 501 measurements from CMS shown in Fig. 11 show a centrality-dependent modification to fragmen-
 502 tation function in PbPb relative to pp data, with a depletion in the mid- ζ range, balanced by an
 503 enhancement at large ζ , in the region corresponding to low- p_T tracks. This shows a redistribu-
 504 tion of energy within the jet cone toward softer particle production in the presence of the medium, con-
 505 sistent with predictions of parton energy loss corresponding to a suppression of high- p_T particles
 506 (model details will be discussed in Sec. 4).

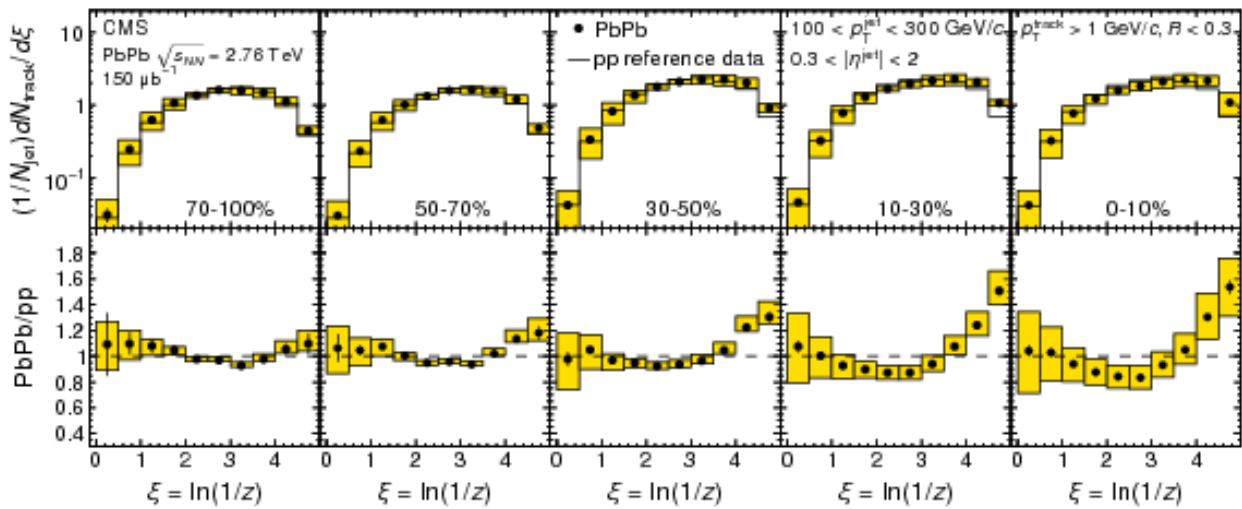


Figure 11. Jet fragmentation function for jets with $100 < p_T < 300$ GeV in 2.76 TeV PbPb and pp data from Ref. [30].

507 In addition to characterizing the p_T spectrum of jet constituents, the distribution of p_T
 508 with respect to the jet axis can also help to constrain fragmentation scenarios. This distribution,
 509 known as the jet shape, is defined within the jet cone as:

$$\rho(\Delta r) = \frac{1}{\delta r} \frac{1}{N_{\text{jet}}} \sum_{\text{jets}} \frac{\sum_{\text{tracks} \in [r_a, r_b]} p_T^{\text{track}}}{p_T^{\text{jet}}}, \quad (18)$$

510 where r_a and r_b correspond to the inner and outer radii, respectively, of an annulus of width $\delta r = 0.5$
 511 around the jet axis. The first jet shape measurement from CMS, shown in Fig. 12 (measured with
 512 particles with $p_T > 1$ GeV), shows a spatial redistribution of energy from small radii ($\Delta r \approx 0.1$)
 513 to larger radii ($\Delta r > 0.2$) from the jet axis. This is qualitatively consistent with predictions of
 514 energy redistribution into particles that are both relatively soft ($p_T < 3$ GeV, as observed in jet
 515 fragmentation function measurements), and recovered at relatively large angles from the jet axis.
 516 In this way, the study of jet shape modifications *within* the jet cone motivate extension of these
 517 measurements to larger angles from the jet axis to quantify the distribution and p_T composition of
 518 particles at angles larger than $\Delta r = 0.3$.

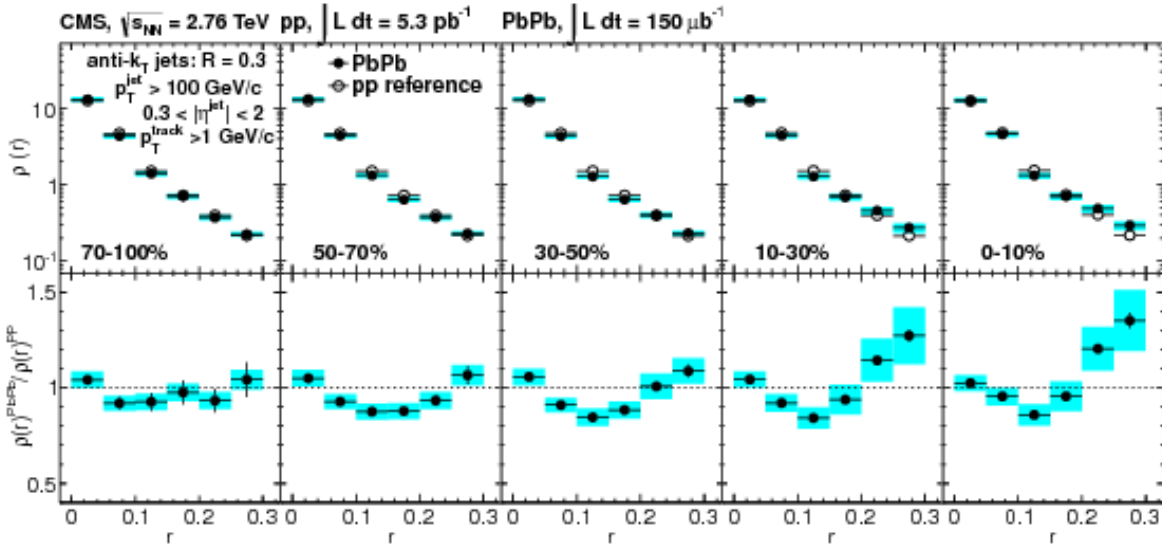


Figure 12. Jet shape measurement in 2.76 TeV PbPb and pp data from Ref. [31].

519 **3.3 Dijet asymmetry and momentum balance studies**

520 Additional possibilities for exploration of medium properties follow from the consideration of “di-
521 jets,” jets that are back-to-back in azimuthal angle ($\Delta\phi_{\text{jets}} \approx \pi$). As the incoming collision partici-
522 pants each begin with $p_T \approx 0$ GeV, the total p_T of outgoing partons immediately after the collision
523 must also be 0. If both partons experience either no energy loss (as in the vacuum) or approximately
524 equal energy loss (i.e. by experiencing roughly equal path-lengths through the medium), the mea-
525 sured p_T of each jet in the dijet pair would be approximately equal. If, however, the hard-scattering
526 occurs toward the surface of the QGP, the jet with a longer path-length through the medium might
527 be expected to experience substantially more energy loss, leading to a p_T asymmetry in the dijet
528 pair as illustrated in Fig. 13. This expectation was probed via studies of di-hadron correlations
529 with high- p_T particle triggers ($4 < p_T < 6$ GeV by STAR at RHIC, $8 < p_T < 15$ GeV by ALICE
530 at the LHC) showed results consistent with the expectation. These studies showed the substantial
531 suppression (even disappearance, in the STAR studies) of yields of particles with $p_T > 2$ GeV in
532 the region opposite the trigger hadron in azimuth [32, 33], consistent with path-length dependent
533 jet quenching and a surface bias in trigger particles.

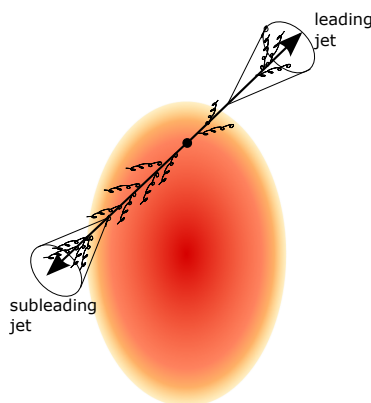


Figure 13. A “back-to-back” pair of dijets separated by $\Delta\phi = \pi$, with a highest- p_T leading jet experiencing less quenching in the medium, and a more-quenched subleading jet with a longer path length through the medium.

534 The large kinematic reach of hard probes at the LHC allows for dijet studies at much higher
535 p_T . The first of these studies measured the “dijet imbalance” between the highest- p_T (“leading

536 jet,” with $p_{T,1}$) and second-highest- p_T jets (“subleading jet,” with $p_{T,2}$ in the event, parameterized
 537 as:

$$A_J = \frac{p_{T,1} - p_{T,2}}{p_{T,1} + p_{T,2}} \quad (19)$$

538 These studies, by the ATLAS and CMS Collaborations [34, 35] showed a centrality-dependent shift
 539 in the A_J in PbPb collisions, with greater dijet asymmetry in central PbPb data than in pp or in
 540 peripheral PbPb collisions. In pp and peripheral PbPb collisions, asymmetric dijet events are those
 541 in which some p_T is carried by a third jet, and the A_J distribution is steeply falling. In central PbPb
 542 collisions, however, there are expected to be two contributions to the sameple of asymmetric dijet
 543 events: not only three-jet events, but also dijet events in which the subleading jet is substantially
 544 quenched. As shown Fig. 14, this effect is evident in the shift toward larger values of A_J in central
 545 PbPb collisions.

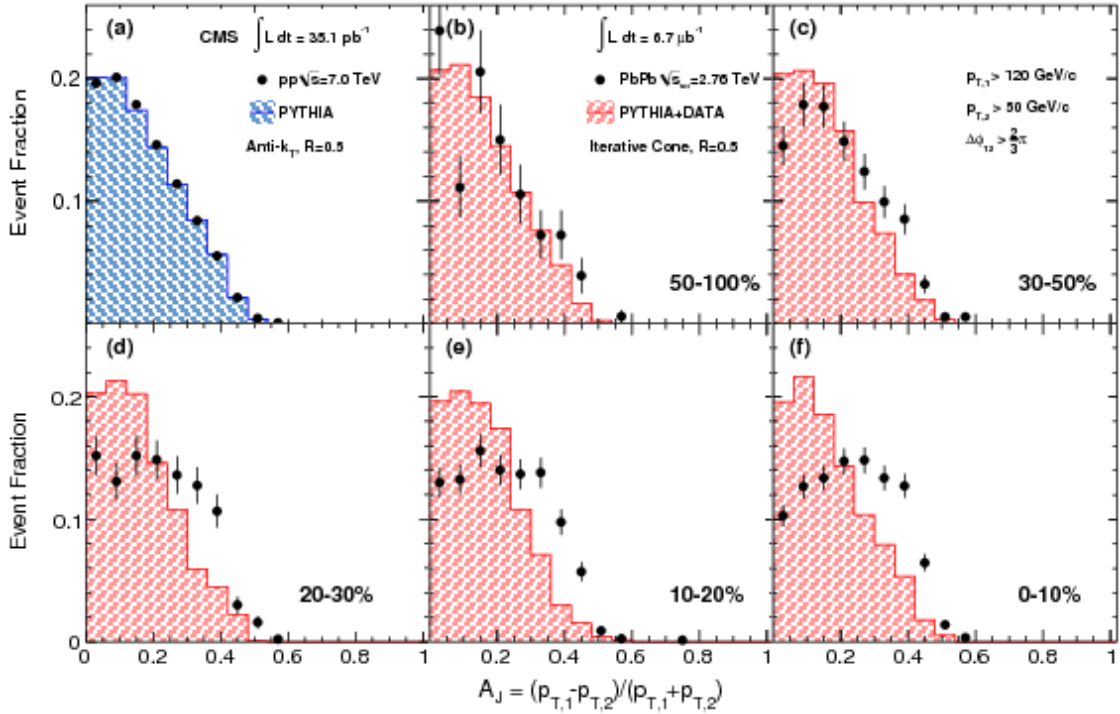


Figure 14. Dijet asymmetry in 2.76 TeV PbPb and pp data for jet selection $p_{T,1} > 120$ GeV, $p_{T,2} > 50$ GeV, and $\Delta\phi_{1,2} > 2\pi/3$ from Ref. [35].

546 The transverse momentum difference between the leading and subleading jets may be con-
 547 ceptualized as “missing- p_T ” from the subleading jet, which must by momentum conservation be

recovered somewhere in the hemisphere of the event surrounding the subleading jet axis. One way
 to capture this momentum balance is by comparing the total p_T carried by tracks in different p_T
 classes in the subleading relative to the leading hemisphere. This balance is shown in the top row
 Fig. 15, for $\langle p_T^{\parallel} \rangle$ defined as the projection of each track's p_T projected in ϕ onto the dijet axis (i.e.
 the average of the leading and subleading jet axes) [54]. In pp and peripheral PbPb data, this
 balance shows the depletion of tracks with $p_T > 8$ GeV in the subleading relative to the leading
 hemisphere balanced primarily by tracks with $2 < p_T < 8$ GeV, consistent with the localization
 of these tracks in additional jets for unbalanced dijets in this scenario. The magnitude of the
 “missing- p_T ” balancing distribution increases with growing A_J by construction. Comparing PbPb
 to pp distributions (differences shown in the bottom row of Fig. 15), the balancing distribution in
 unbalanced (large A_J) events in central PbPb data shows larger contributions from soft particles
 with $p_T < 2$ GeV and smaller contributions from particles with $p_T > 4$ GeV, indicating that the
 more of the balancing p_T distribution in the subleading side is carried by soft quenching products
 rather than additional jets.

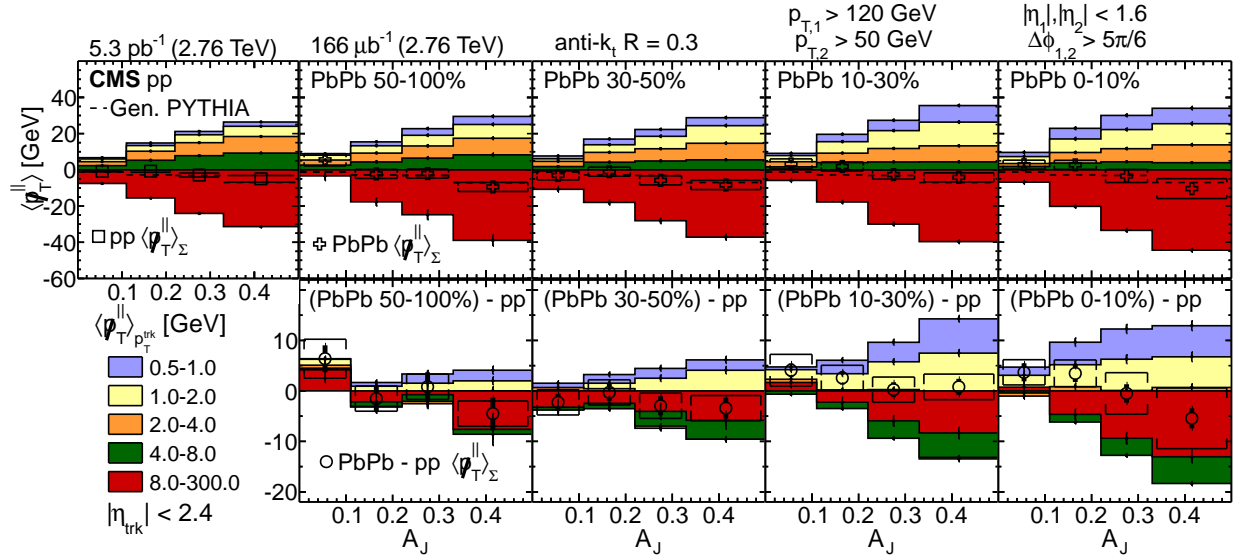


Figure 15. Top row: hemisphere p_T momentum balance in dijet events as a function of A_J , taking the total difference $\langle p_T^{\parallel} \rangle$ in the subleading hemisphere minus that in the leading hemisphere from Ref. [54] in pp and PbPb data. Bottom row: Differences PbPb - pp.

Dijet momentum balance studies therefore show evidence of redistribution of jet energy
 from harder to softer particles via jet quenching, and greater quenching of the subleading than

leading jets. As discussed above, the angular distribution of quenching products relative to the jet axis is also highly relevant for constraining models of interactions between the jet and the medium. This measurement is shown in Fig. 16 for unbalanced dijets with $A_J > 0.22$. Comparing the radial distribution with respect to the dijet axis shows that in this unbalanced dijet sample in central PbPb events, more p_T is recovered in lower- p_T particles extending to large angles from the jet axis. It is important to note that this measurement shows overall hemisphere differences in the radial p_T distribution, combining the effects of quenching to the subleading jet, quenching to the leading jet, and also any azimuthal asymmetry in the underlying event (as would arise if the direction of the dijet axis coupled to odd underlying event flow terms such as v_3). Isolating and further studying each of these contributions will be a major goal of this analysis, as discussed in Sec. 4.3.4.

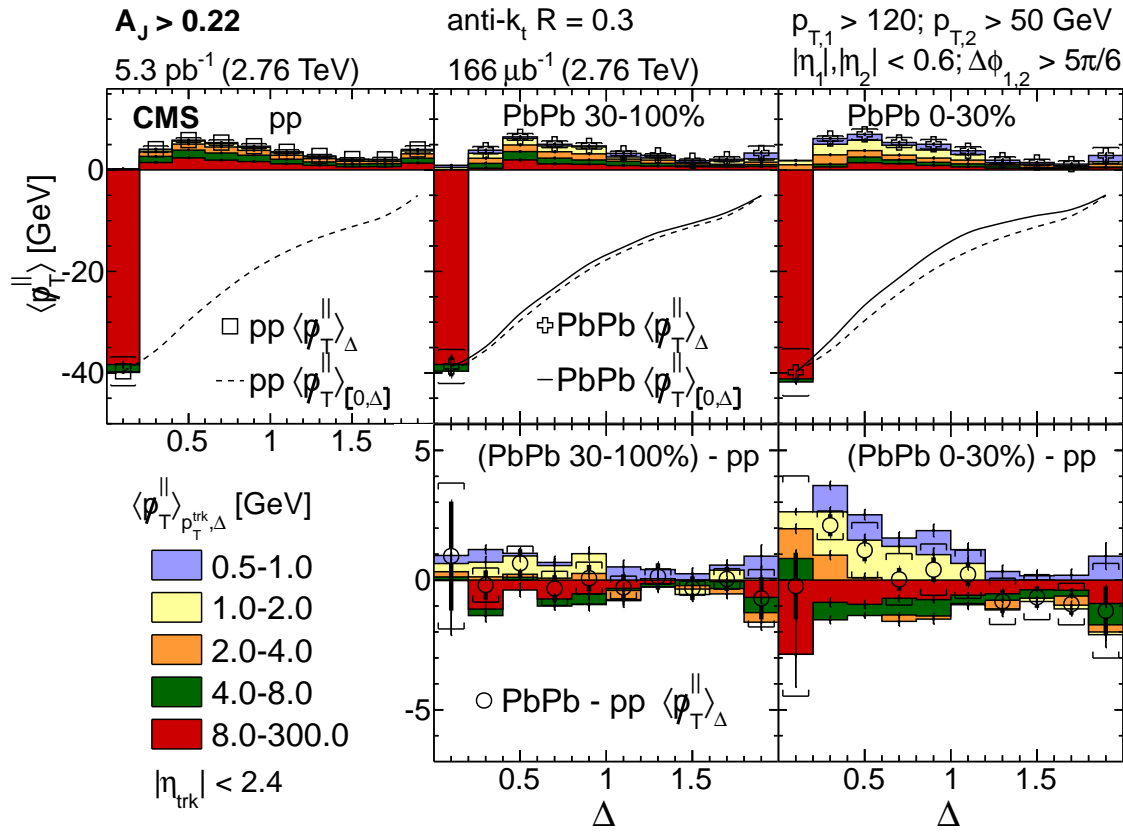


Figure 16

574 **4 MODELS OF JET ENERGY LOSS IN THE QUARK GLUON PLASMA**

575 A range of theoretical models of jet quenching have been developed to specifically account for the
576 energy loss of a propagating probe through the quark gluon plasma. In general, models characterize
577 collisional energy loss mechanisms (i.e. jet energy loss via elastic interactions with the medium),
578 radiative energy loss by the propagating parton, and in some cases a medium response in the form
579 of a “plasma wave” or back reaction. Some prominent examples of specific quenching models are
580 surveyed briefly in Sec. 4.1. Some relevant comparisons to data are shown in Sec. 4.2, and then
581 Sec. 4.3 summarizes goals of the present analysis in the context of the current state of jet quenching
582 models.

583 **4.1 Survey of theoretical models of jet quenching mechanisms**

- 584 • DGLV (and CUJET implementation)
 - 585 • BDMPS-Z/ASW (and JEWEL implementation)
 - 586 • Higher-Twist
 - 587 • AMY (McGill and MARTINI implementations)
 - 588 • Soft collinear effective theory with glauber gluons arxiv:1509.07257 <https://arxiv.org/pdf/1601.04695.pdf>
 - 589 • Linear Boltzman Transport model <https://arxiv.org/pdf/1703.00822.pdf>
 - 590 • Strong/weak hybrid model from AdS/CFT arXiv:1101.0618v2 arXiv:1609.05842
 - 591 • Coupled jet-fluid model arXiv:1701.07951
- 592 Nice summary of these <https://arxiv.org/pdf/1312.5003.pdf>
- 593 New Mehar-Tani paper (substructure and Raa) <https://arxiv.org/pdf/1707.07361.pdf>

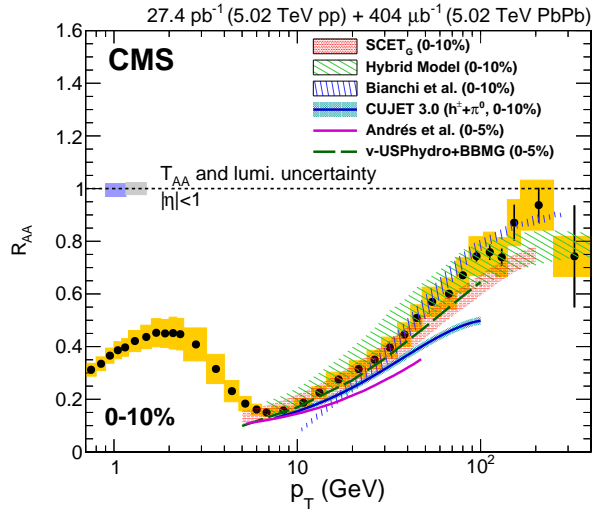


Figure 17. Model comparisons to charged particle R_{AA} in 0-10% central PbPb data at 5.02 TeV from Ref. [27].

594 4.2 Quenching model comparisons to high- p_T particle and jet observables

595 4.2.1 Quenching model comparisons: R_{AA}

596 4.2.2 Quenching model comparisons: jet fragmentation functions

597 4.2.3 Quenching model comparisons: jet shapes

598 4.2.4 Quenching model comparisons: dijet asymmetry

599 4.3 Theoretical motivations for detailed jet-track correlation studies

600 4.3.1 Extension of jet shape measurements to large angles

601 4.3.2 Detailed characterization of jet peak in separate dimensions $\Delta\eta$ and $\Delta\phi$

602 4.3.3 Detailed characterization of leading and subleading jet peaks in dijet events

603 4.3.4 Decomposition of contributions to momentum balance studies in dijet events

604 **5 THE LARGE HADRON COLLIDER AND THE CMS DETECTOR**

605 **5.1 The Large Hadron Collider**

606 The Large Hadron Collider (LHC), located at CERN near Geneva, is the largest and highest-
607 energy particle accelerator in the world. It consists of two counter-rotating particle beam line in
608 a tunnel 26.7 km in circumference, located between 45 m and 170 m underground [36]. During
609 standard operation, the LHC collides beams of protons accelerated and focused using a series
610 of superconducting magnets, cooled to below 2 K using supercritical helium. Particle beams are
611 brought together for collisions at in experimental detectors at four points in the accelerator ring: the
612 ATLAS, CMS, ALICE, and LHCb detectors. In addition to the proton-proton (pp) data collected
613 at center-of-mass energies $\sqrt{S_{NN}} = 7 \text{ TeV}$, 8 TeV , and 13 TeV , the LHC has also been operated
614 for heavy ion physics by colliding with fully-stripped lead nuclei ($^{182}\text{Pb}^{82+}$) in lead-lead (PbPb)
615 and proton-lead (pPb) collisions. Heavy ion runs at the LHC have included PbPb data and pp
616 “reference” runs at $\sqrt{S_{NN}} = 2.76 \text{ TeV}$ (2011 and 2013, respectively) and 5.02 TeV (2015) and pPb
617 data at $\sqrt{S_{NN}} = 5.02 \text{ TeV}$ (2013 and 2016) and 8.16 TeV (2016). This analysis relies on PbPb
618 data at 2.76 TeV and 5.02 TeV , and corresponding pp reference data at the same center-of-mass
619 energies.

620 In peak proton-proton operation, the LHC collides 2,808 bunches each containing approx-
621 imately 10^{11} protons with a minimum bunch spacing of 25 ns, for a maximum luminosity of
622 $10^{34} \text{ cm}^{-2} \text{ s}^{-1}$ delivered to the high-luminosity detectors (ATLAS and CMS). The lead-lead per-
623 formance target of $10^{27} \text{ cm}^{-2} \text{ s}^{-1}$ delivered via 592 bunches of 10^7 lead ions was slightly exceeded
624 during the 2015 PbPb run. At this high-intensity frontier, it is common during nominal pp data
625 collection and possible in PbPb data collection that multiple distinct proton-proton collisions may
626 occur within a recorded event in a phenomenon known as “pile-up.” However, pile-up is relatively
627 rare in PbPb collisions due to the lower luminosities, and in the present analysis only one primary
628 vertex will be considered (with products of any other possible interactions removed via background
629 subtraction procedures).

630 **5.2 The CMS detector**

631 The CMS detector is named for the Compact Muon Solenoid at its heart: a superconducting magnet
632 with magnetic field of 3.8 T, length of 13 m, diameter of 6 m, and weight 14,000 tons. Inside
633 of this solenoid, the detector includes silicon pixel and strip detectors for particle tracking (see
634 Sec. 5.3 for a detailed explanation), and electromagnetic and hadronic calorimeters (see Sec. 5.4).
635 Calorimeters within the solenoid volume are complemented by additional calorimetry outside of the
636 solenoid that provides coverage in the very forward direction close to the beam line, including the
637 hadronic forward (HF) calorimeter in the region $3.0 < |\eta| < 5.2$ used in this analysis for centrality
638 determination, and the Zero Degree and CASTOR calorimeters in the even more forward region.
639 The CMS detector also includes an extensive muon system outside of the solenoid volume, consisting
640 of aluminum drift tubes in the barrel region, cathode strip chambers in the forward region, and a
641 complementary system of resistive plate chambers (not discussed in detail here as muons are not of
642 primary relevance to this analysis). Full details about the CMS detector may be found in Ref. [37],
643 and a perspective drawing of the CMS detector from this report is shown in Fig. 18.

644 In the CMS detector, the $+z$ axis is defined to be horizontal, pointing to the West along
645 the beam line direction. The x axis is horizontal, pointing to the South toward the center of the
646 LHC. The $+y$ axis is vertical, pointing upward. The azimuthal angle $\phi = \tan^{-1}(\frac{y}{x})$ is defined in
647 the x - y plane such that $\phi = 0$ is the $+x$ axis. Pseudorapidity $\eta = -\ln(\tan(\frac{\theta}{2}))$ is defined to have the
648 same sign as the $+z$ axis. Pseudorapidity coverage in the CMS detector ranges from $\eta = 0$ at the
649 y -axis, to $|\eta| > 8.3$ in Zero Degree Calorimeter approaching the $+/z$ axis.

650 **5.3 Trackers in the CMS detector**

651 The CMS tracking system consists of a small silicon pixel detector for precise measurement near
652 the interaction point (with three layers with radii 4.4 cm to 10.2 cm), surrounded by a large silicon
653 strip detector with layers to a radius of 110 cm. In both detectors, a cylindrical tracker “barrel” is
654 complemented by “endcap” disks that together provide full azimuthal coverage and pseudorapidity
655 coverage in the range $|\eta| < 2.5$. The pixel detector consists of 66 million pixels in 1440 modules.
656 It provides three-dimensional measurements of “hits,” or interactions of particles with tracker
657 materials, with a transverse resolution $10\mu\text{m}$ and longitudinal resolution $20 - 40\mu\text{m}$ (and a third

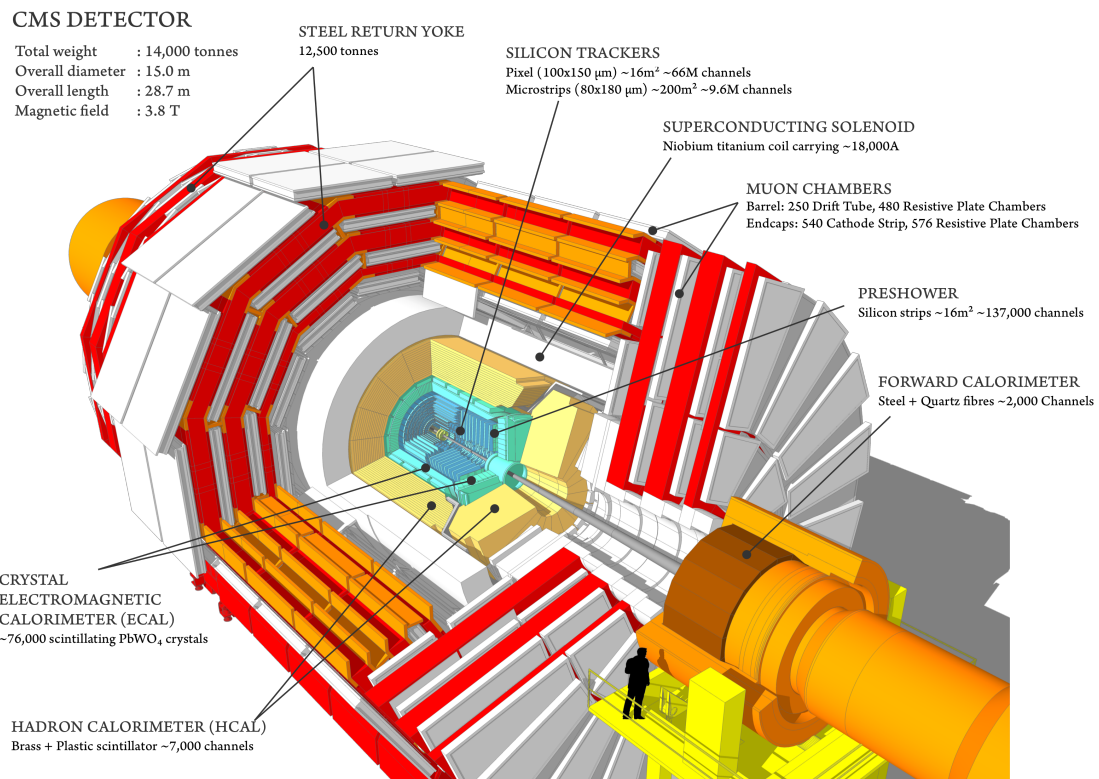


Figure 18. Perspective rendering of the CMS detector, showing component sub-detectors with a human included for scale perspective [38].

coordinate provided by the pixel plane). The silicon strip detector consists of 9.3 million strips in 15,148 modules, organized in four components: Tracker Inner Barrel (TIB) and Disks (TID), Tracker Outer Barrel (TOB, covering the region $r > 55$ cm), and Tracker End Caps (TEC, covering the region $124 < |z| < 282$ cm). Figure 19 shows a diagram of the pixel and strip detectors, which have total length 5.8 m and diameter 2.5 m [39]. Track reconstruction and tracking efficiency will be discussed in detail in Sec. 6.

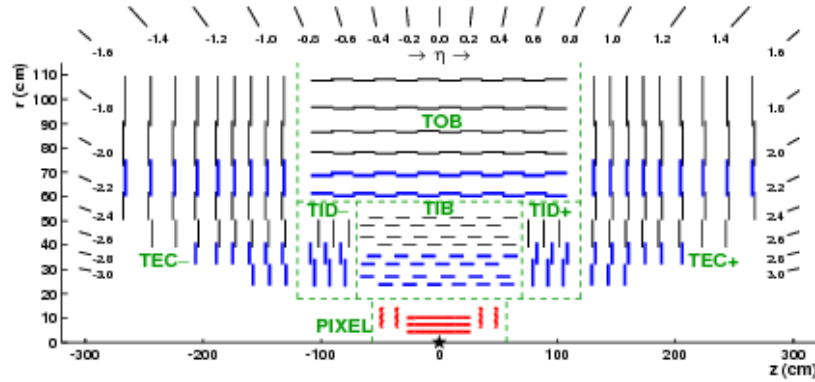


Figure 19. Diagram of CMS pixel and silicon strip detectors in the $r - z$ plane [39].

5.4 Calorimeters in the CMS detector

This analysis relies on electromagnetic and hadronic calorimeters for the energy measurements used as inputs for the reconstruction of high- p_T jets. The ECAL, which measures the energy of charged particles, consists of 75 848 lead tungstate (PbWO_4) crystal scintillators, organized in 5 arrays, covering $|\eta| < 1.48$ in a barrel region and $1.48 < |\eta| < 3.0$ in the endcap region. Light from the scintillators is captured with avalanche photodiodes in the barrel region, and vacuum phototriodes in the endcap region. A preshower detector system in front of the ECAL is used to assist in the identification of neutral pions and electrons [37]. ECAL energy resolution ranges from about 1-2.5% (depending $|\eta|$ and photon conversion) in the barrel region, and from 2.5-4% in the endcap region. [40].

Hadrons pass through the ECAL and are stopped by the HCAL, a hermetic detector which records their energy using a system of scintillator tiles embedded with wavelength-shifting fibers.

676 The HCAL has three regions, as shown in Fig. 20: barrel (HB), endcap (HE), and an outer region
 677 (HO) outside of the solenoid, necessitated by the fact that the HB is volume-limited by the solenoid
 678 diameter. In the barrel region $|\eta| < 1.74$, the HCAL cells have widths of 0.087 in pseudorapidity
 679 and 0.087 in ϕ , while for $|\eta| > 1.74$ the coverage of the towers increases progressively to a maximum
 680 of 0.174 in $\Delta\eta$ and $\Delta\phi$. HCAL towers are mapped onto ECAL towers within the barrel region, and
 681 their summed energies are used to determine the location, energy, and axis of jets, as described
 682 below in Sec. 7. The HCAL is complimented in the forward region by the HF calorimeters, which
 683 each consist quartz fibers in the $\pm z$ directions organized in 432 readout towers in the region $3.0 <$
 684 $|\eta| < 5.2$ [37]. In this analysis, only jets from the barrel region of the calorimeters will be included,
 685 while the HF detector is used for the determination of PbPb event centrality as described in Sec. 8.2.



Figure 20. Diagram of the HCAL [37].

686 5.5 The CMS trigger system

687 The collision rate at the LHC is so high that it is impossible to store and process every event
 688 that occurs in the CMS detector. A two-level online trigger system is therefore used to select events
 689 of interest. Furthermore, data selected with loose trigger requirements (for example “zero bias”
 690 data with no selection criteria and “minimum bias” criteria consisting of minimal requirements to
 691 demonstrate the presence of a collision event) may also need to be further “prescaled” to limit
 692 the rate of recorded events by a specified factor. The trigger system consists of a first (L1) trigger
 693 consisting of programmable electronics that use information from the calorimeter and muon systems

694 of the detector to select events to record. The L1 trigger operates with an interval of approximately
695 4μ s, with a maximum rate of 100 kHz. The next trigger level, the High Level Trigger (HLT), consists
696 of a processor farm that allows for more sophisticated event selection based on the reconstruction of
697 physics objects. Reconstruction is performed in a series of steps, or a “HLT path,” chosen to apply
698 selection in order of increasing reconstruction complexity, so as to minimize processing time [41].
699 This analysis will rely primarily on two kinds of triggers: minimum bias data, and jet-triggered
700 data samples selected by requiring the presence of an online reconstructed jet with $p_T > 80$ GeV
701 ($p_T > 100$ GeV for 5.02 TeV PbPb data). No prescale is applied for the jet-triggered data samples
702 used in this analysis.

6 TRACK RECONSTRUCTION AND CORRECTION

704 6.1 Track reconstruction in pp collisions

705 Standard track reconstruction in CMS occurs in the following steps, summarized here and described
 706 in detail in Ref. [39]:

- 707 • **Hit reconstruction** – In the pixel tracker, zero-suppression is performed by setting an ad-
 708 justable threshold, equivalent charge to 3200 for each pixel. Pixel hits are reconstructed as
 709 clusters of adjacent pixels, requiring a minimum charge equivalent of 4000 electrons (compared
 710 to at least 21,000 electrons deposited by a typical ionizing particle). In the strip detector,
 711 zero-suppression is performed by subtracting the baseline pedestal and noise from the signal,
 712 and clusters are seeded with channels which contain charge at least three times that of the
 713 pedestal. Adjacent strips are added to the cluster if their charge is more than twice that of
 714 the pedestal, and the cluster is kept if its total charge is at least five times larger than the
 715 combined strip noise. Cluster position in the strip detector is determined from the charge-
 716 weighted average of strip positions, corrected for Lorentz drift. The average efficiency for hit
 717 reconstruction in both the pixel and strip detectors (excluding 2.4% of pixel modules and
 718 2.3% of strip modules known to be defective) is > 99 %.
- 719 • **Track seed generation** – Track reconstruction begins by first running a fast track and
 720 vertex reconstruction using the pixel tracker only to reconstruct the beamspot position and
 721 the location of primary vertices in the event. After this, track reconstruction is carried out in
 722 six iterations, each of which begins with “seeds” that define the trajectories and uncertainties
 723 of potential tracks. The first set of seeds are pixel triplets, produced from corresponding sets
 724 of three pixel hits (on a helical track trajectory) with weak constraints on compatibility with
 725 the beam spot to require that the tracks correspond to promptly produced particles. In later
 726 iterations, additional information from vertex reconstruction and the silicon strip detector is
 727 incorporated in seed generation.
- 728 • **Track finding** – The seeds generated in the step above are used as starting points for
 729 track-finding based on the Kalman filter method, implemented in four steps for each tracker
 730 layer. First, track parameters at the starting level are extrapolated, assuming a perfectly

731 helical track trajectory (neglecting multiple scatterings, energy loss, and non-uniformity in
732 the magnetic field), to determine the locations of interception in other pixel layers. The second
733 step is a search for tracker modules consistent with the interception locations determined in
734 the previous step. In the third step, hits from mutually exclusive module groups (i.e. groups
735 of modules for which it is not possible that one track could pass through more than one of
736 the grouped modules) are used to update and refine hit locations (including the possibility of
737 adding “ghost” hits where a particle failed to produce a hit due to module inefficiency) and to
738 calculate the Lorentz drift in the silicon bulk. Finally, in the fourth and last step, new track
739 candidates are formed by adding one compatible hit from each of the module groupings, and
740 trajectories are updated combining this added hit with the original track path extrapolation.
741 All track candidates at a given level are then extrapolated to the next compatible layer and
742 the procedure repeated through five iterations.

- 743 • **Track fitting** – Finally, the track trajectory is refitted to reduce possible biases (due, for
744 example, to the beam spot constraint introduced in initial seed finding), and to remove
745 outlying hits falsely associated to a track.

746 After tracks are reconstructed according to this procedure, the track sample both includes a contri-
747 bution from “fake” tracks (that do not correspond to the trajectory of an ionizing particle), which
748 is reduced by requiring certain selection criteria as discussed in Sec. 6.3. The collection also suffers
749 from detector and reconstruction inefficiencies, which are corrected in this analysis according to
750 the procedure described in Sec. 6.4.

751 6.2 Track reconstruction in PbPb collisions

752 In PbPb collision data, dedicated track reconstruction is necessary due to the dramatically greater
753 multiplicity in PbPb compared to pp collisions. This heavy ion tracking occurs in the following
754 steps, and is detailed in Refs. [42] and [43]:

- 755 • **Hit reconstruction** – Tracker hits are reconstructed following the same basic procedure
756 applied in pp collisions.
- 757 • **Track seed generation** – First, primary vertex positions are reconstructed using only a
758 collection of pixel hits, extrapolated to the region near the beam spot. In PbPb data pileup

759 is negligible, so there is generally only one primary vertex reconstructed in each event. Initial
760 track seeds are then constructed from pixel triplets only. To reduce combinatorial back-
761 grounds, seeds are restricted to those pointing to a region within 2 mm of the primary vertex,
762 and further selections are applied on track p_T , goodness-of-fit (χ^2), and compatibility between
763 the seed trajectory and the primary vertex.

764 • **Track finding** – Track trajectories are propagated through the tracker following a procedure
765 similar to that outlined above for pp data. The track seeding and finding procedure is repeated
766 through three iterations. In the second and third iterations, hits belonging unambiguously to
767 a previously identified tracks are first removed, and then reconstruction is repeated using pixel
768 triplet and pixel pair seeds (in the 2nd and 3rd iterations, respectively). Tracks identified in
769 these later iterations are merged into first-iteration tracks, with duplicates removed based on
770 hit matching.

771 6.3 High purity tracks

772 The track reconstruction procedures described above for pp and PbPb collision data give track
773 collections with significant “fake rates,” or fraction of reconstructed tracks that cannot be associated
774 with a particle. This fake rate is reduced with a series of quality selections, defined in three levels:
775 “loose” criteria define the minimum to keep tracks in track collections, “tight” criteria are somewhat
776 more stringent (sacrificing some lost efficiency for a lower fake rate), and finally “high purity”
777 criteria are most strict and are those applied for most CMS analyses, including those reported
778 here. Track quality in each case is set with flags for each track, and criteria in each case are
779 applied separately at each iterative tracking step. The precise criteria for high purity tracks at
780 each iterative pass are defined in Refs. [39, 42, 43], and include the following types of selections,
781 imposed as a function of p_T and η :

- 782 • Requirements on the number of hits on the track trajectory (N_{hit})
- 783 • Requirements on the minimum layers in which the track has an associated hit (N_{layers} , and
784 on the maximum intercepted layers in which the track has no assigned hits)
- 785 • A minimum imposed on the goodness-of-fit of the track ($\chi^2/\text{Ndof}/N_{\text{layers}}$ or χ^2/N_{hit})

- 786 • A maximum on relative track- p_T uncertainty
- 787 • Maxima on longitudinal and transverse impact parameters (d_z and d_{xy}) with respect to the
788 primary vertex position and beam spot
- 789 In pp data, criteria are optimized by the quality metric $Q(\rho) = s/\sqrt{s + \rho b}$, where s = selected
790 ("real") tracks, b = selected fake tracks, and parameter $\rho \approx 10$ weights the metric toward min-
791 imizing the fake rate. In PbPb data from Run 2, optimization is performed via the output of a
792 multivariate analysis tool (MVA), as detailed in Ref. [43].
- 793 **6.4 Tracking efficiency and fake rate evaluation and correction**
- 794 Tracking efficiency for charged particles in pp collisions ranges from approximately 80% at $p_T \approx 0.5$ GeV
795 to 90% or better at $p_T \approx 10$ GeV and higher. Track reconstruction is more difficult in the heavy-ion
796 environment due to the high track multiplicity, and tracking efficiency for PbPb collisions ranges
797 from approximately 30% at 0.5 GeV to about 70% at 10 GeV. Tracking efficiencies are evaluated
798 using PYTHIA and PYTHIA+HYDJET Monte Carlo simulation, by comparing track distributions as
799 generated to those after MC samples are passed through GEANT detector simulation and recon-
800 structed with the algorithms used to reconstruct data. Corrections are derived as a function of
801 centrality, p_T , η , ϕ , and local charged particle density. Tracking efficiency closure and systematic
802 uncertainty is evaluated in pythia and pythia+hydjet, comparing generated track p_T , η , and ϕ dis-
803 tributions to reconstructed distributions before and after correction. For illustration, examples of
804 these closure checks for 5.02 TeV PYTHIA simulation are shown in Fig. 21. Additional 5% residual
805 systematic uncertainty is conservatively assigned for possible differences between MC and data that
806 might affect tracking performance.

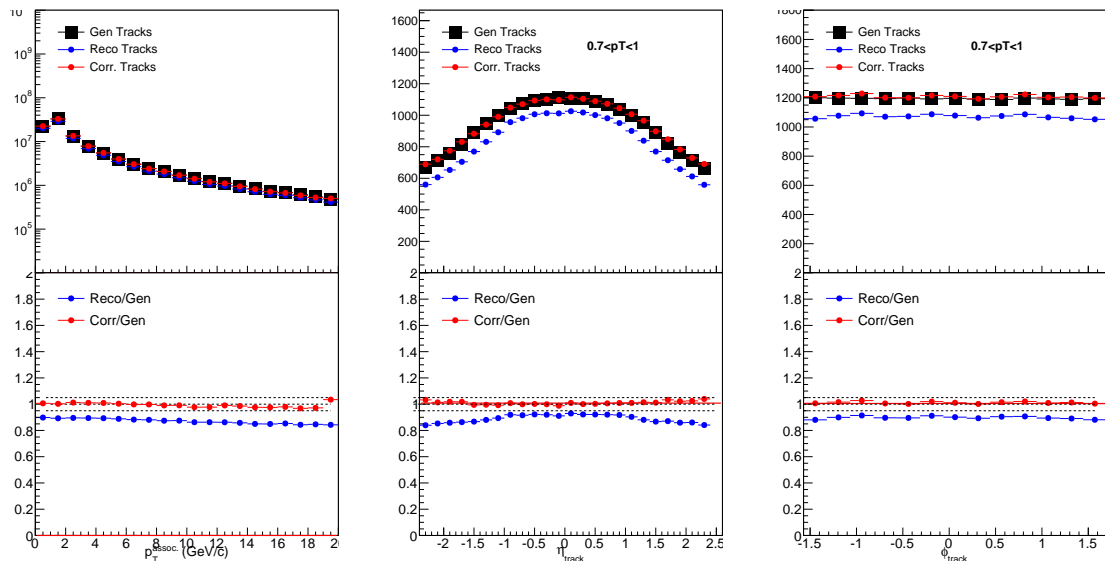


Figure 21. Tracking efficiency correction closure for PYTHIA simulation at 5.02 TeV, comparing tracking generated tracks to uncorrected and corrected reconstructed tracks, as a function of track p_T and of pseudorapidity, and azimuth for the lowest p_T^{trk} bin.

7 JET RECONSTRUCTION AND CORRECTION

808 7.1 Jet reconstruction with the anti- k_t algorithm

809 The goal in jet reconstruction is to identify clusters of hadrons originating from a fragmenting high-
 810 energy parton. In high- p_T jet studies in pp collisions, the general locations of jets in an event may
 811 be qualitatively obvious via large energy deposits in calorimeters; however, there is no clear single
 812 standard of how jet boundaries should be drawn. In practice, jets are defined by the algorithms
 813 used to find and determine their direction. These algorithms fall in two primary categories: “cone
 814 algorithms,” which define jets within specific conical regions (based on the fact that hadronization
 815 has little effect total momentum flow), and “sequential recombination algorithms,” which iteratively
 816 identify and cluster pairs of closest particles to form jets that are not necessarily conical. [44, 45, 46].
 817 Several properties are desireable, from theoretical and experimental perspectives, in jet finding:

- 818 • Straightforward implementation for both theoretical calculations and jet-finding and recon-
 819 struction in experimental measurements
- 820 • Cross-sections that are finite in perturbation theory
- 821 • Infrared and collinear (IRC) safety – the property that a soft collinear emission in a parton
 822 splitting should not modify the overall collection of hard (high- p_T) jets in the event, in
 823 particular avoiding the possibility of non-cancelling divergences in perturbation calculations
- 824 • Soft resilience – clustering jets that are reasonably regular and not overly sensitive to soft
 825 particles, a property motivated by the finite resolution of experimental detectors.

826 Heavy ion jet studies in CMS use the anti- k_t algorithm, a soft-resilient, IRC safe, and straightforward
 827 sequential recombination algorithm [45], implemented in the FastJet framework [46]. The anti- k_t
 828 algorithm clusters entities (calorimeter towers, particles, or partially clustered pseudo-jets) i and
 829 j based on the distance measures d_{ij} between the two particles and d_{iB} between the particle and
 830 beam, with the measures defined as:

$$d_{ij} = \min(k_{ti}^{-2}, k_{tj}^{-2}) \frac{(\Delta R_{ij})^2}{R^2}, \quad (20)$$

$$d_{iB} = k_{ti}^{-2}, \quad (21)$$

where k_{ti} refers to the transverse momentum of particle i , ΔR_{ij} refers to the spatial distance (in rapidity and azimuth) between the two particles, and radius parameter R is a reconstruction parameter. The name anti- k_t derives from the negative exponent for k_t (in contrast to other sequential recombination algorithms), which enables IRC safety and soft resilience by making jet shape sensitivity to a particle inversely correlated to the particle's transverse momentum. With this low sensitivity to soft particles, the anti- k_t algorithm results in a collection of mostly circular jets (except in the case of jets separated by less than $2R$, in which each jet has a radius of πR^2). The choice of parameter R is a trade-off between capturing more fragmentation products (as can extend as far as $\Delta R_{ij} = 0.8$ in pp collisions), and limiting the influence of background particles in jet reconstruction. In heavy ion experimental studies, where background levels are very high, typical choices of R range from 0.2 to 0.5.

With the CMS detector, jets may be clustered from ECAL and HCAL information only (“calorimeter jets”) or from information from the full detector, using the particle flow (PF) algorithm. The PF algorithm improves jet energy resolution (JER) substantially at low- p_T (at 10 GeV JER is 15% for PF jets versus 40% for calorimeter jets) with improvements decreasing for higher- p_T jets (at 100 GeV PF jet JER is 8% versus 12% for calorimeter jets, falling to a difference of 4% versus 5% at 1 TeV). For jet-track correlation studies, however, the resolution improvements that the particle flow algorithm offers come at the cost of enhancing sensitivity to tracking biases in the jet-track correlation signal, since low- p_T tracks are included in jet reconstruction. In this analysis, calorimeter jets are used to avoid these auto-correlation effects, and because we will consider jets with $p_T > 120$ GeV for which calorimeter jet energy resolution is adequate. Jets are reconstructed with anti- k_t radius $R = 0.3$ for 2.76 TeV data (“ak3Calo” jets), and with radius $R = 0.4$ for 5.02 TeV data (“ak4Calo” jets). In pp data at 2.76 TeV and 5.02 TeV the contribution to the jet energy from the underlying event (UE) is negligible (less than 1 GeV), so no underlying event subtraction is employed.

856 **7.2 Underlying event subtraction in PbPb data**

857 In PbPb collisions it is necessary to subtract contributions from the large underlying event in order
858 to recover the true jet energy. There are a variety of methods used for underlying event subtraction,
859 of which the following two are relevant for this analysis.

860 **7.2.1 Noise/pedestal subtraction**

861 In most CMS high- p_T jet analyses, including 5.02 TeV PbPb data studies here, underlying event
862 subtraction is performed using a variant of an iterative noise/pedestal subtraction technique [47].
863 This algorithm occurs in the following steps:

- 864 • First, the mean “pedestal” energy in calorimeter cells as a function of energy η ($P(\eta)$) is
865 calculated along with its dispersion.
- 866 • The pedestal function $P(\eta)$ is subtracted from all cells.
- 867 • Cells with non-physical negative energy entries are then set to zero.
- 868 • $\langle E_{\text{cell}} \rangle + \langle \sigma(E_{\text{cell}}) \rangle$ is subtracted from each cell to compensate for the elimination of negative
869 energy cells.
- 870 • Jets are clustered from the pedestal-subtracted cells using the anti- k_t algorithm.
- 871 • The pedestal function $P(\eta)$ is then re-derived using only cells that are not a part of clustered
872 jets, and the algorithm is repeated.

873 After this underlying event subtraction is applied, the anti- k_t algorithm with radius parameter
874 $R = 0.4$ is then employed for jet reconstruction (“akPu4Calo jets”).

875 **7.2.2 HF/Voronoi subtraction**

876 For 2.76 TeV PbPb data a different algorithm, designed to eliminate the threshold and possible
877 resulting bias from the noise/pedestal technique, is employed [42]. This algorithm uses information
878 from the HF detector to model and subtract the underlying event using Voronoi decomposition
879 (“HF/Voronoi” algorithm) in the following steps:

- The distribution of underlying E_T as a function of η and ϕ is modeled using singular value decomposition (SVD) training ($dE_T/d\eta/\phi$ with Voronoi parameters $v_1 \dots v_4$) to extrapolate the UE distribution from the HF calorimeter at large η to the central analysis region ($|\eta| < 1.6$).
 - The modeled UE distribution is subtracted from all calorimeter cells.
 - Each calorimeter cell is associated with its nearest neighbors, and energy is redistributed between neighboring in an “equalization” procedure used to eliminate non-physical negative E_T entries (optimized to minimize energy transfers).
- After Voronoi subtraction and equalization, the anti- k_t algorithm is employed with radius parameter $R = 0.3$ to cluster (“akVs3Calo”) jets.

7.3 Jet energy corrections

Jet reconstruction as described above gives spatial coordinates and p_T for each jet as measured by the detector. Our goal in jet studies, however, is to reconstruct the true total parton or particle energy. This is achieved through jet energy corrections (JEC) that establish a mapping between measured energy (which does not, for example, include neutrinos produced in jet fragmentation) and “true” jet energies. This mapping is complicated by nonlinearity in detector response. Initial corrections are derived as a function of p_T and η using dijet QCD samples of PYTHIA and PYTHIA+HYDJET Monte Carlo, spatially matching reconstructed jets to generated particles, and comparing generated versus reconstructed jet energy for these matched jets. These “MC truth” corrections are applied to measured jet energies to return a collection of jets that, on average, capture the kinematic distribution of the partons before fragmentation.

These corrections do not, however, fully account for the non-linearity of calorimeter response. In particular, in an effect particularly relevant for jet-track correlation studies, the jet energy scale depends on jet fragmentation. Given two jets with identical parton energy, the jet with softer fragmentation (i.e. jets with a higher fraction low- p_T particles) will be on average reconstructed with lower energy than the jet with harder fragmentation. When combined with a jet selection threshold, this non-linearity results in a bias that systematically underestimates the jets with soft fragmentation in the analysis sample. An additional fragmentation-function dependent jet energy correction (JFF-JEC) is therefore applied after initial jet energy corrections in order to

908 reduce this bias (detailed in Ref. [42]). These JFF-JEC are derived using the number of particle flow
 909 candidates (N_{PF}) in the jet with $p_T > 2$ GeV, with this threshold chosen to reduce the influence
 910 of soft fluctuations in the underlying event. Correction tables are derived as a function of N_{PF} , jet
 911 p_T , and PbPb event centrality in PYTHIA and PYTHIA+HYDJET simulation, and are applied to jets
 912 after the JECs described above. Finally, iterative residual corrections are applied as a function of
 913 jet p_T . The application of JFF-JECs reduces the overall quark/gluon non-closure, as illustrated for
 914 PbPb data in Fig. 22, and slightly improves jet energy resolution overall.

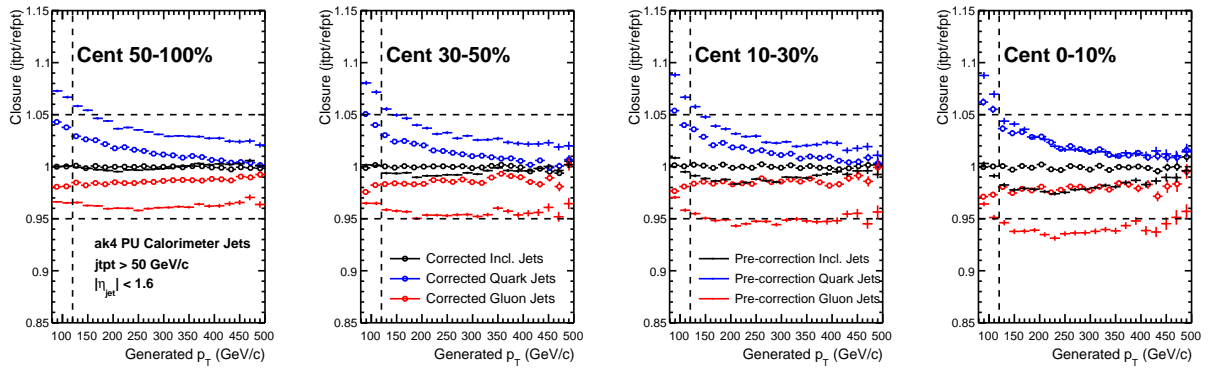


Figure 22. Closure with and without JFF-JEC for quark and gluon jets.

8 DATA AND MONTE CARLO SAMPLES

916 8.1 Data samples and event selection

917 This analysis is based on PbPb and pp data collected with the CMS detector at 2.76 TeV and 5.02
 918 TeV during Run 1 and Run 2 of the CERN LHC. Studies at 2.76 TeV use $166 \mu\text{b}^{-1}$ of PbPb data
 919 collected in 2011, and 5.3 pb^{-1} of pp data collected in 2013. Studies at 5.02 TeV use $404 \mu\text{b}^{-1}$ of
 920 PbPb data and 25 pb^{-1} of pp data, both collected in 2015. Online collision selection was performed
 921 using the CMS HLT described in Sec. 5.5 to obtain a minimum bias sample of PbPb collision events,
 922 and to obtain samples of PbPb and pp data with the requirement that events contain at least one
 923 high- p_{T} jet (with $p_{\text{T}} > 80 \text{ GeV}$ for pp data and 2.76 TeV PbPb data, $p_{\text{T}} > 100 \text{ GeV}$ for 5.02 TeV
 924 PbPb data). These jet triggers are fully efficient for offline-reconstructed jets with $p_{\text{T}} > 120 \text{ GeV}$.
 925 Total numbers of selected events are summarized in Table I.

TABLE I. Summary of data samples and number of selected events

Dataset	Number of selected events
2.76 TeV PbPb MinimumBias	1.01 M
2.76 TeV PbPb Jet-triggered ($p_{\text{T}} > 80 \text{ GeV}$)	1.25 M
2.76 TeV pp Jet-triggered ($p_{\text{T}} > 80 \text{ GeV}$)	1.27 M
5.02 TeV PbPb MinimumBias	764 k
5.02 TeV PbPb Jet-triggered ($p_{\text{T}} > 100 \text{ GeV}$)	3.35 M
5.02 TeV pp Jet-triggered ($p_{\text{T}} > 80 \text{ GeV}$)	2.66 M

926 A number of quality cuts are applied, as is standard for CMS analyses to remove detector
 927 noise backgrounds, ultra-peripheral collisions, beam gas events, and events with exceptionally large
 928 pixel occupancy. These selection criteria have shown to have negligible impact on dijet analyses [48,
 929 49], and are as follows in PbPb and pp collisions:

- 930 • Vertex-z position within 15 cm of the center of the detector ($|v_z| < 15$)

- Primary vertex filter – a requirement that events include a reconstructed primary vertex filter with at least two tracks, requiring the presence of inelastic hadronic scattering and removing beam-gas events and ultra-peripheral collisions
 - Beam-scraping filter – a requirement of pixel clusters compatible with the primary vertex. In pp, this requires that if there are more than 10 tracks, at least 25% of tracks must be highPurity (see Sec. 6)
 - HB/HE noise filter – a filter to exclude events exhibiting uncharacteristic calorimeter noise [50]
 - PbPb data only: HF coincidence filter – at least 3 GeV recorded in at least each of at least three hadronic forward calorimeter towers on each side of the interaction point
- These cleaning cuts are applied to both minimum bias and jet-triggered data samples. Additional event selection will later be applied to obtain samples of high- p_T jets and dijet events, as discussed in Sec. 8.4 below.

8.2 Collision centrality determination and classes

The variable centrality is used to parameterize the degree of overlap of the colliding nuclei. In CMS, centrality is determined using total transverse energy (E_T) in the HF calorimeter towers, in the region $4.0 < |\eta| < 5.2$. The distribution of total E_T in all events is used to divide the total minimum bias event sample into centrality bins, each containing 0.5% of the total events. The resulting centrality distribution is flat in minimum bias data by construction. In jet-triggered data, however, requiring the presence of a high- p_T jet results in a larger fraction of more central collisions (in which hard-scatterings are more likely). The collisions defined as “most central” (centrality = 0%) are those with the greatest E_T , corresponding to collisions in which the nuclei collided head-on. In contrast, the collisions defined as “least central” or “most peripheral” (centrality = 100%) are those in which the nuclei barely overlapped at all. To observe how jet modifications evolve with changing centrality, this analysis considers four centrality classes: 0-10% (most central), 10-30%, 30-50%, and 50-100%.

956 **8.3 Monte Carlo simulation**

957 Monte Carlo (MC) simulation is used in this analysis to evaluate and correct for jet reconstruction
958 performance and tracking efficiency for both pp and PbPb data. Simulation of pp data and of
959 the hard processes in PbPb data are performed using the PYTHIA (version 6, tune Z2 [51]) event
960 generator. In order to have reasonable event samples in all jet p_T ranges, different samples are
961 produced with various cut-off values of \hat{p}_T , which are then combined using their respective cross-
962 sections as weights. To simulate CMS detector output for MC events, GEANT4 detector simulation
963 is used [52]. Jet and track reconstruction performance and efficiency for pp data is evaluated by
964 comparing observables in PYTHIA samples as generated to the same observables after they have
965 been passed through the detector simulation and the same reconstruction procedures applied to
966 pp data. For the relevant jet kinematics observables relevant to this analysis, PYTHIA reasonably
967 reproduces pp data.

968 For PbPb data, the underlying event is simulated using HYDJET (Drum5 tune) [53], which
969 combines hydrodynamics with “mini-jets” produced with quenched PYTHIA input. Hard processes
970 are generated using PYTHIA, and are directly embedded in this HYDJET sample (referred to as
971 PYTHIA+HYDJET simulation), with no medium quenching effects applied to the embedded jets.
972 This PYTHIA+HYDJET sample is used to evaluate the reconstruction effects of the presence of the
973 heavy ion collision environment, *other* than the jet-medium interactions that are our objects of
974 study. As for PYTHIA simulation of pp data, comparing PYTHIA+HYDJET samples that have been
975 passed through the detector and reconstructed chain to the generated Monte Carlo allows for the
976 evaluation of jet and track reconstruction performance.

977 **8.3.1 Monte Carlo centrality and vertex-z reweighting**

978 Simulated PYTHIA+HYDJET samples are generated minimum bias, and therefore must be reweighted
979 to match the bias toward more central events induced by requiring the presence of a high- p_T
980 jets discussed in Sec. 8.2. Reweighting factors are calculated for each 0.5%-wide centrality bin,
981 and applied to the PYTHIA+HYDJET sample overall to match the PbPb centrality distribution.
982 Similarly, another reweighting procedure is performed to match the distributions of the position of

983 the primary interaction along the beam direction in MC and data for both pp and PbPb collisions.
984 Figures 23-25 illustrate the necessity and effects of these reweighting procedures.

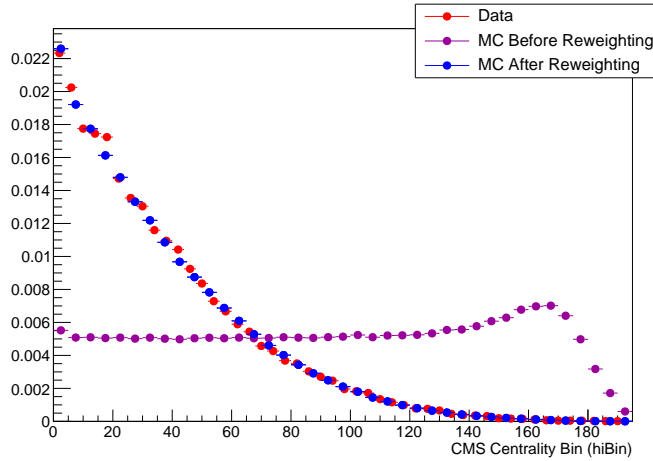


Figure 23. Centrality distribution for PYTHIA+HYDJET reweighted to match centrality distribution of PbPb data.

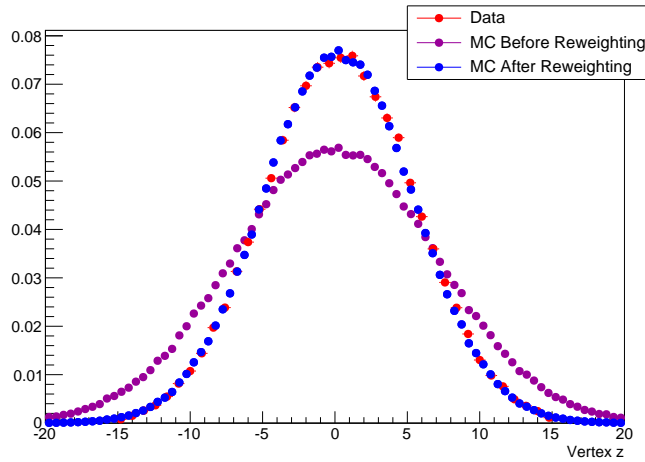


Figure 24. Vertex z distribution for PYTHIA+HYDJET reweighted to match centrality distribution of PbPb data.

985 8.3.2 Monte Carlo samples at 2.76 TeV

986 Tables II and III summarize the PYTHIA and PYTHIA+HYDJET samples used in this analysis by \hat{p}_T ,
987 with respective numbers of generated events and cross-sections used for combining samples.

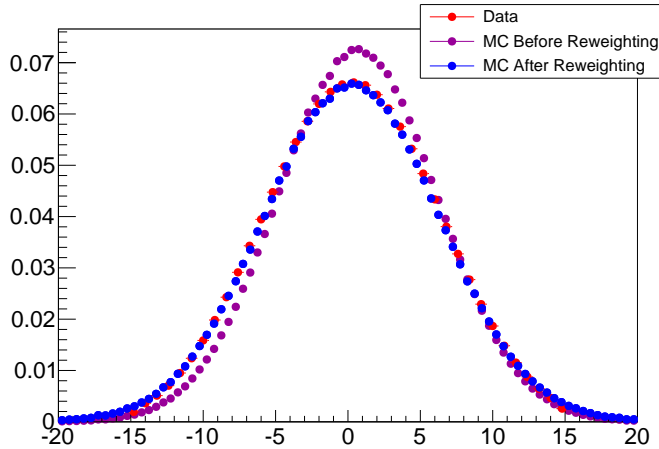


Figure 25. Vertex z distribution for PYTHIA reweighted to match centrality distribution of pp data.

TABLE II. Summary of Monte Carlo samples and generated events at 2.76 TeV

Generator	Process	Cross section (mb)	Number of events
PYTHIA+HYDJET	$\hat{p}_T > 50 \text{ GeV}$	1.025×10^{-3}	395k
PYTHIA+HYDJET	$\hat{p}_T > 80 \text{ GeV}$	9.865×10^{-5}	368k
PYTHIA+HYDJET	$\hat{p}_T > 120 \text{ GeV}$	1.129×10^{-5}	367k
PYTHIA+HYDJET	$\hat{p}_T > 170 \text{ GeV}$	1.465×10^{-6}	392k
PYTHIA+HYDJET	$\hat{p}_T > 220 \text{ GeV}$	2.837×10^{-7}	181k
PYTHIA+HYDJET	$\hat{p}_T > 280 \text{ GeV}$	2.837×10^{-7}	50k
PYTHIA	$\hat{p}_T > 80 \text{ GeV}$	9.865×10^{-5}	104k
PYTHIA	$\hat{p}_T > 120 \text{ GeV}$	1.129×10^{-5}	975k
PYTHIA	$\hat{p}_T > 170 \text{ GeV}$	1.465×10^{-6}	69k

988 **8.3.3 Summary of Monte Carlo samples at 5.02 TeV**

TABLE III. Summary of Monte Carlo samples and generated events at 5.02 TeV

Generator	Process	Cross section (mb)	Number of events
PYTHIA+HYDJET	$\hat{p}_T > 80 \text{ GeV}/c$	4.412×10^{-4}	499k
PYTHIA+HYDJET	$\hat{p}_T > 120 \text{ GeV}/c$	6.147×10^{-5}	496k
PYTHIA+HYDJET	$\hat{p}_T > 170 \text{ GeV}/c$	1.018×10^{-5}	498k
PYTHIA+HYDJET	$\hat{p}_T > 220 \text{ GeV}/c$	2.477×10^{-6}	200k
PYTHIA+HYDJET	$\hat{p}_T > 280 \text{ GeV}/c$	6.160×10^{-7}	200k
<hr/>			
PYTHIA	$\hat{p}_T > 80 \text{ GeV}/c$	4.412×10^{-4}	500k
PYTHIA	$\hat{p}_T > 120 \text{ GeV}/c$	6.147×10^{-5}	500k
PYTHIA	$\hat{p}_T > 170 \text{ GeV}/c$	1.018×10^{-5}	499k
PYTHIA	$\hat{p}_T > 220 \text{ GeV}/c$	2.477×10^{-6}	200k
PYTHIA	$\hat{p}_T > 280 \text{ GeV}/c$	6.160×10^{-7}	200k

989 **8.4 Jet selection and dijet asymmetry classes**

990 Jet selection in this analysis is restricted to the pseudorapidity region $|\eta_{\text{jet}}| < 1.6$ to ensure stable
991 reconstruction performance in the calorimeter barrel region. A requirement is also imposed that
992 the highest- p_T track contains no less than 1% and no more than 98% of the total jet p_T . In the
993 jet selection referred to as “inclusive jets” for analysis at both 2.76 TeV and 5.02 TeV, all jets with
994 $p_{T,\text{jet}} > 120$ GeV are considered. In this selection, it is possible to select more than one jet from
995 the same event, provided that each jet satisfies the inclusive selection criteria.

996 In addition to the inclusive jet selection, a “dijet” selection of events containing two back-
997 to-back high- p_T jets is also analyzed for the 2.76 TeV data sample. Events are included in this
998 sample based on the criteria that they contain highest- p_T “leading” jet with $p_{T,1} > 120$ GeV and a
999 second-highest- p_T “subleading” jet with $p_{T,2} > 50$ GeV with relative azimuthal separation between
1000 the two jets $\Delta\phi_{1,2} > \frac{5\pi}{6}$. This dijet sample is subdivided into a sample of relatively “balanced”
1001 dijets, with similar $p_{T,1}$ and $p_{T,2}$ and a sample of relatively “unbalanced” dijets in which the leading
1002 jet has a much larger p_T than the subleading jet based on asymmetry parameter A_J . The balanced
1003 selection is defined as those events for which $A_J < 0.22$, while the unbalanced selection is defined
1004 as those events for which $A_J > 0.22$. The dividing value $A_J = 0.22$ is chosen for consistency with
1005 previous CMS analyses [35, 54]. In this analysis, 52% of central PbPb events are balanced, while
1006 67% of pp events are balanced. Jet kinematics for all jet samples (broken down by asymmetry for
1007 2.76 TeV dijet data) are shown in Appendix A.1 for 2.76 TeV data and in Appendix A.2 for 5.02
1008 TeV data.

1009 **8.5 Track selection and classes**

1010 Tracks, reconstructed as described in Sec. 6 are required to satisfy the following criteria:

- 1011 • $|\eta_{\text{trk}}| < 2.4$ – restricts to the barrel region of the tracker
- 1012 • $0.5 < p_{\text{T}}^{\text{trk}} < 300$ GeV – excludes very low- p_T tracks where reconstruction performance is not
1013 stable
- 1014 • High Purity criteria – see Sec. 6.3

- 1015 • Distance of closest approach (DCA) in x-y plane and in z less than 3 times the DCA error –
 1016 reduces fraction of tracks not associated with a primary vertex
- 1017 • Relative p_T^{trk} error less than 30% (10% for 5.02 TeV PbPb data) – removes tracks with very
 1018 poor resolution (has a negligible effect on efficiency as CMS resolution is generally good)
- 1019 For 5.02 TeV PbPb data, the following additional criteria are also applied to reduce the contribution
 1020 from misidentified tracks [43]:
- 1021 • Exclude tracks with fewer than 11 tracker hits
- 1022 • Require that for each track the chi-squared over number of degrees of freedom (χ^2/Ndof) of
 1023 the track fit, also divided by the number of tracker layers (nLayer) hit as the track passed
 1024 through the detector, is less than 0.15, i.e. $\chi^2/\text{Ndof}/\text{nLayer} < 0.15$.
- 1025 • For tracks with $p_T > 20$ GeV (the kinematic region in which misreconstruction is difficult to
 1026 access with Monte Carlo), calorimeter matching is applied: since high- p_T tracks eventually
 1027 deposit their energy in a calorimeter after passing through the tracker, tracks are required
 1028 to be associated with calorimeter transverse energy $E_T = (E_{\text{ECAL}} + E_{\text{HCAL}})/\cosh(\eta_{\text{trk}})$, such
 1029 that $E_T > 0.5p_T^{\text{trk}}$
- 1030 After these selection criteria are applied, tracking efficiency corrections are applied as described
 1031 in Sec. 6.4. Tracks in this analysis are considered in the following classes: 0.5–1 GeV, 1–2 GeV,
 1032 2–3 GeV, 3–4 GeV, 4–8 GeV, 8–12 GeV, 12–16 GeV, 16–20 GeV, and above 20 GeV. Not all bins
 1033 are considered in every analysis, and for 5.02 TeV studies the lowest- p_T^{trk} bin is 0.7–1 GeV.

¹⁰³⁴ **8.6 Summary of analysis bins**

¹⁰³⁵ Table IV summarizes the key kinematic selections and bins for the three components to this analysis.

¹⁰³⁶ In all cases, identical selection is applied to PbPb and pp data. Event, jet, and track quality cuts

¹⁰³⁷ are not included in this table.

TABLE IV. Summary of data selections and analysis bins

Variable	2.76 TeV Inclusive	5.02 TeV Inclusive	2.76 TeV Dijets
PbPb Centrality	0-10%, 10-30%, 30-50%, 50-100%	0-10%, 10-30%, 30-50%, 50-100%	0-10%, 10-30%, 30-50%, 50-100%
Jet Selection	$ \eta_{\text{jet}} < 1.6$ $p_T > 120 \text{ GeV}$	$ \eta_{\text{jet}} < 1.6$ $p_T > 120 \text{ GeV}$	$ \eta_{\text{jet}} < 1.6$ $p_{T,1} > 120 \text{ GeV}$ $p_{T,2} > 50 \text{ GeV}$ $\Delta\phi_{1,2} > \frac{5\pi}{6}$
A_J Bins	–	–	$A_J < 0.22$, $A_J > 0.22$
Track η	$ \eta_{\text{trk}} < 2.4$	$ \eta_{\text{trk}} < 2.4$	$ \eta_{\text{trk}} < 2.4$
p_T^{trk} Bins	1-2 GeV, 2-3 GeV, 3-4 GeV, 4-8 GeV	0.7-1 GeV, 1-2 GeV, 2-3 GeV, 3-4 GeV, 4-8 GeV	0.5-1 GeV, 1-2 GeV, 2-3 GeV, 3-4 GeV, 4-8 GeV, 8-300 GeV

9 JET-TRACK CORRELATION MEASUREMENTS

1039 9.1 Analysis procedure

1040 Measurements in this analysis are carried out by considering correlations between high- p_T jets and
 1041 tracks in PbPb and pp collisions. Jets are selected within $\eta < 1.6$ and p_T above a particular
 1042 threshold. For each jet, the relative separation in pseudorapidity ($\Delta\eta = \eta_{\text{track}} - \eta_{\text{jet}}$) and azimuth
 1043 ($\Delta\phi = \phi_{\text{track}} - \phi_{\text{jet}}$) is measured between the jet and all charged-hadron tracks within $\eta < 2.4$. For
 1044 each jet-track pair, these measurements are recorded in a two-dimensional $\Delta\eta - \Delta\phi$ correlation in
 1045 a particular track transverse momentum (p_T^{trk}) and centrality class. Each correlation is normalized
 1046 by dividing by the number of jets in the sample (N_{jets}), resulting in a signal pair distribution,
 1047 $S(\Delta\eta, \Delta\phi)$, that gives the per-jet yield of tracks and their relative distance from the jet:

$$1048 S(\Delta\eta, \Delta\phi) = \frac{1}{N_{\text{jets}}} \frac{d^2 N^{\text{same}}}{d\Delta\eta d\Delta\phi}. \quad (22)$$

1049 This procedure results in a two dimensional measurement of the distribution of charged
 1050 tracks with respect to the jet axis. The same procedure may also be repeated, weighting each track
 1051 by its p_T^{trk} , in order to obtain a distribution of transverse momentum with respect to the jet axis.
 1052 These particle density and p_T^{trk} correlations form the basis for all results discussed in this analysis.
 1053 From this point, several additional corrections and other steps are necessary to isolate jet-related
 effects from long range and uncorrelated backgrounds. These additional steps are as follows:

- 1054 • A correction for jet-track pair acceptance effects;
- 1055 • Separation of correlations into short-range jet peaks and and long range components;
- 1056 • Monte Carlo-based corrections for biases related to jet reconstruction.

1057 After these steps, a range of different observables may be extracted to characterize the multiplicity
 1058 and distribution of tracks and p_T^{trk} at both small and large angles from the jet axis.

1059 **9.2 Jet-track correlation pair-acceptance correction**

1060 This analysis considers $\Delta\eta$ jet-track separations as large as $\Delta\eta = 2.5$. With finite η acceptance for
1061 both jets and tracks ($|\eta_{\text{jet}}| < 1.6$ and $|\eta_{\text{track}}| < 2.4$, tracks that fall within $\Delta\eta = 2.5$ of a jet may be
1062 outside the tracking acceptance. This pair acceptance effect results in trapezoidal correlations that
1063 fall with rising $|\Delta\eta|$ as tracks are “lost” outside of the acceptance. This effect is purely geometric,
1064 and may be corrected by reproducing this pair acceptance geometry. This is done by creating a
1065 “mixed event” correlation in which jets in the sample are correlated to tracks within $|\eta| < 2.4$ from
1066 randomly selected events in a minimum bias PbPb sample, matched in vertex- z position (within 0.5
1067 cm) and centrality (within 2.5%). This reproduces the pair acceptance geometry from the signal
1068 correlations:

$$ME(\Delta\eta, \Delta\phi) = \frac{1}{N_{\text{jets}}} \frac{d^2N^{\text{mix}}}{d\Delta\eta d\Delta\phi}, \quad (23)$$

1069 is constructed to account for pair-acceptance effects, with N^{mix} denoting the number of mixed-event
1070 jet-track pairs. The mixed event correction is normalized to unity at $\Delta\eta=0$, where the jet and track
1071 are colinear in η and therefore have perfect pair acceptance, with the normalization factor $ME(0, 0)$.
1072 Dividing the signal correlation $S(\Delta\eta, \Delta\phi)$, defined in Equation 22, by this normalized mixed event
1073 correlation $ME(\Delta\eta, \Delta\phi)/ME(0, 0)$ yields the corrected per-jet correlated yield distribution, as
1074 illustrated in Figure 26:

$$\frac{1}{N_{\text{jets}}} \frac{d^2N}{d\Delta\eta d\Delta\phi} = \frac{ME(0, 0)}{ME(\Delta\eta, \Delta\phi)} \times S(\Delta\eta, \Delta\phi). \quad (24)$$

1075 **9.3 Separation of correlations into long range and short-range components**

1076 After correlations are corrected for pair-acceptance effects, in each correlation we are left with a
1077 well-defined jet peak sitting at $\Delta\eta = 0$, $\Delta\phi = 0$ on top of a large combinatoric and long range
1078 correlated background. For most measurements, it is necessary to isolate this jet peak in order to
1079 distinguish jet-related effects from eventwise correlations. In order to achieve this, we note that the
1080 long range correlation is independent of $\Delta\eta$ at distances larger than $\Delta\eta = 1.5$ from the jet. This
1081 “sideband” region ($1.5 < |\Delta\eta| < 3.0$) is used to model the underlying event, capturing both the

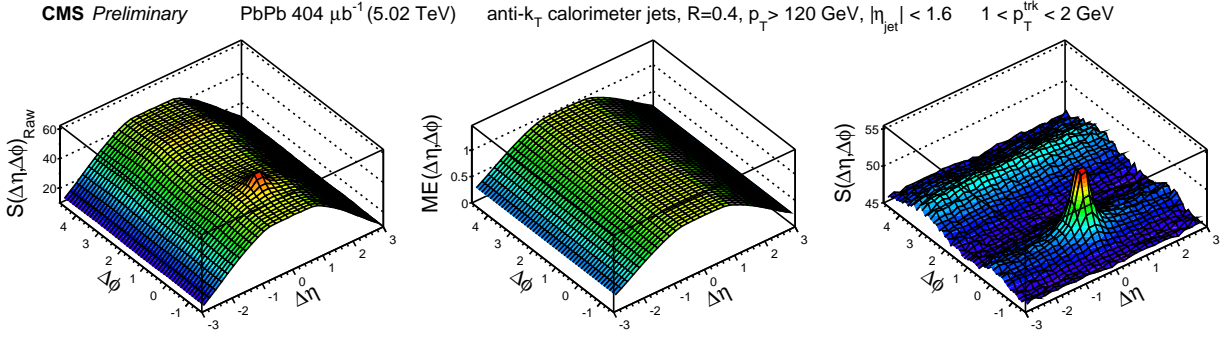


Figure 26. Illustration of the pair-acceptance correction procedure: left panel shows signal correlation $S(\Delta\eta, \Delta\phi)$, and center panel shows mixed event correlation $ME(\Delta\eta, \Delta\phi)$. Dividing the signal correlation by the normalized mixed event correlation yields the corrected per-jet correlated yield distribution shown in the right panel.

level of the combinatoric background in the event, and also the long range “flow” correlations in the event. The assumption of rapidity-independence of the flow harmonics is based on the CMS study [55], which shows no appreciable variation of the elliptic flow for charged particles above 1 GeV in the pseudorapidity interval of $\Delta\eta < 3.0$ relevant for this study. As long range correlations depend only on $\Delta\phi$, the sideband region is projected into $\Delta\phi$ to obtain a one-dimensional model of the underlying event. To subtract this long range correlation in 2D, this distribution may be either directly re-propagated into $\Delta\phi$ (as shown in Figure 27), or may be fit in $\Delta\phi$ before repropagation in a smoothing procedure as shown in Fig. 28. When aiming to simply remove the long range correlated background, we fit long range correlations function modeling harmonic flow plus a term to capture the (Gaussian or sharper) “away-side” peak opposite the jet in relative azimuth:

$$B(\Delta\phi) = B_0(1+2V_1 \cos(\Delta\phi)+2V_2 \cos(2\Delta\phi)+2V_3 \cos(3\Delta\phi))+A_{AS} \exp\left(-\left(\frac{|\Delta\phi-\pi|}{\alpha}\right)^\beta\right), \quad (25)$$

In this case, the fit is performed only as a smoothing procedure to model the background under the near-side jet peak.; as only the jet peak within $|\Delta\phi| < \frac{\pi}{2}$ is studied, the fit to the away-side peak is not relevant to the analysis. Furthermore, no physics conclusions can be extracted from the V_n terms in this fit, which are used only to establish a reasonable functional form for smooth modeling of the background distributions.

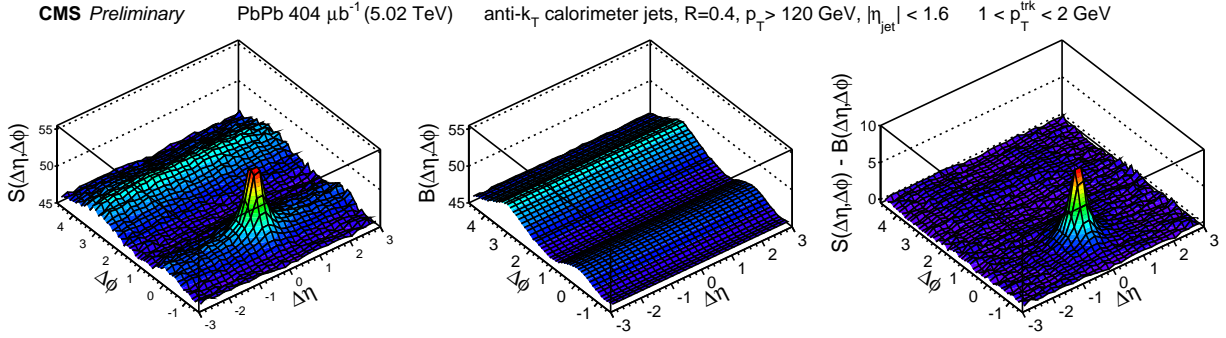


Figure 27. Illustration of the event decomposition procedure without $\Delta\phi$ fitting: left panel shows the acceptance-corrected correlation, middle panel shows the projected and re-propagated long range distribution, and right panel shows the background-subtracted jet peak.

1097 The long range correlations in the underlying event are in themselves interesting objects of
 1098 study, however, as they contain information about the collective behavior of particles in the event as
 1099 a whole, and the extent to which the distribution of high- p_T jets in the event couple to this collective
 1100 flow. To further study the long range correlations, we may apply the well-established harmonic
 1101 flow decomposition method used to study two-particle correlations [56] to correlations between jets
 1102 and tracks. In dijet studies, more accurate information about long range flow correlations can
 1103 furthermore be obtained by making use of the fact that for our dijet selection and a given value
 1104 of $\Delta\eta$ the region $-\frac{\pi}{2} < \Delta\phi < \frac{\pi}{2}$ of the leading correlation is by definition equivalent to the region
 1105 $\frac{\pi}{2} < \Delta\phi < 3\frac{\pi}{2}$ of the subleading correlation. This provides a full 2π distribution of the long range
 1106 correlated underlying event under both the leading and subleading jet peaks. We can then perform
 1107 a single fit to the combined background. Here we fit with harmonic flow terms only:

$$B(\Delta\phi)^{\text{Dijet}} = B_0(1 + 2V_1 \cos(\Delta\phi) + 2V_2 \cos(2\Delta\phi) + 2V_3 \cos(3\Delta\phi)), \quad (26)$$

1108 In this fit, we find that terms through V_3 are necessary to describe the low- p_T , central background,
 1109 while at higher- p_T only V_1 , V_2 . From this combined fit, we extract parameters V_1 , V_2 , and V_3 .
 1110 Then, to better constrain the background under the signal and minimize the effects of random
 1111 background fluctuations, we apply the factorization relation of overall Fourier harmonic $V_2 =$
 1112 $v_2^{\text{jet}} \times v_2^{\text{trk}}$ [57, 21]. The values of v_2^{trk} for charged particles are determined in Ref. [56], while the
 1113 fit parameter v_2 is expected to be independent of p_T^{trk} ranges for a given centrality class. The

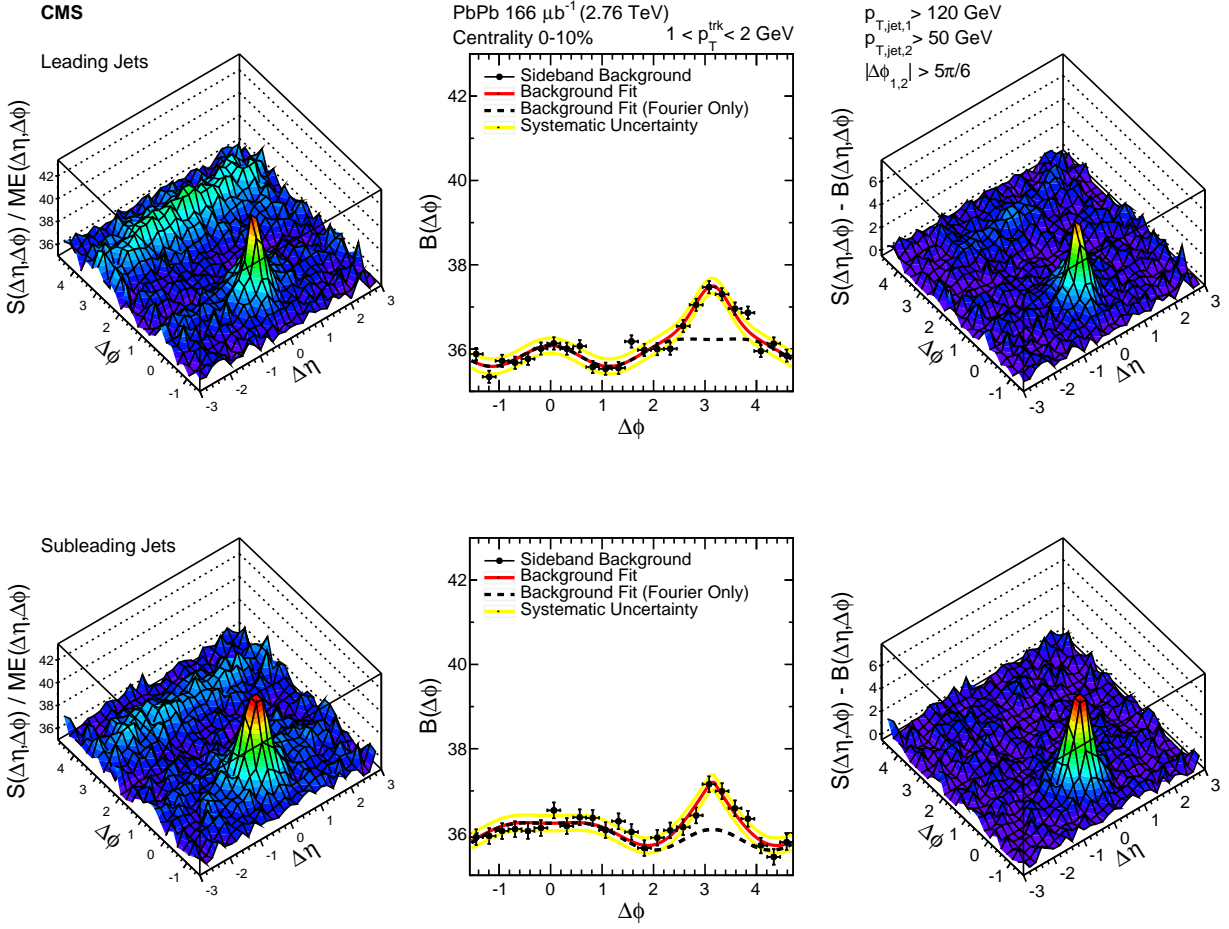


Figure 28. Illustration of the event decomposition procedure with $\Delta\phi$ fitting: left panel shows the acceptance-corrected correlation, middle panel shows the projected and fit long range distribution, and right panel shows the background-subtracted jet peak.

average value of v_2^{jet} from each p_T^{trk} range is calculated, and used to fix the V_2 parameter on the second iteration of the fit. Both the combined dijet fit with $B(\Delta\phi)^{\text{Dijet}}$ and the final $B(\Delta\phi)$ fits are shown in Appendix B. Through this process, we characterize the underlying event and note that the distribution of jets as well as tracks couples to the flow modulation of the underlying event. This has immediate consequences for studies of momentum balance between leading and subleading hemispheres of the event: as there are non-zero contributions from odd harmonics to the long-range correlated backgrounds, we cannot expect flow cancellation when directly subtracting hemishpere p_T^{trk} distributions.

1122 For jet peak studies the underlying event is a background to subtracted to isolate jet peaks.
1123 After this is done, either by direct subtraction or by subtracting the fit and re-propagated back-
1124 ground, we are left with isolated 2D jet peaks. Before extracting observables, we must carefully
1125 consider and correct for reconstruction biases affecting these correlated yields. Before correlations
1126 are constructed, both tracks and jets are corrected for detector efficiencies and other reconstruction
1127 effects, as discussed in detail in Sec. 6 and Sec. 7, respectively. There are two additional effects,
1128 however, in which jet biases are coupled to the multiplicity of low- p_T tracks: a bias against recon-
1129 structing jets with soft fragmentation that arises from nonlinearity in calorimeter response (reduced
1130 but not eliminated by the JFF-JEC described in Sec. 7.3), and a bias toward selecting jets that
1131 sit on upward (soft) fluctuations in the background resulting in excess low- p_T yields around the jet
1132 axis. Both effects are studied and corrections obtained by carrying out the full analysis in Monte
1133 Carlo simulation, and corrections are applied to the data correlations after background subtraction.

1134 9.4 Residual Jet Fragmentation Function correction

1135 Jets with harder fragmentation are more likely to be successfully reconstructed than jets with softer
1136 fragmentation, resulting in a bias toward the selection of jets with fewer associated tracks in both
1137 pp and PbPb data for all track- p_T selections studied. This bias is partially resolved by the jet
1138 fragmentation function-dependent jet energy corrections described in Sec. 7. Following the method
1139 used in [54], corrections are derived for this bias and for the related possible effect of "jet swapping"
1140 between leading, subleading, and additional jets by comparing correlated per-trigger particle yields
1141 for all reconstructed jets versus all generated jets. This correction is derived for each jet selection in
1142 PYTHIA-only simulation, and also in PYTHIA embedded and reconstructed in a HYDJET underlying
1143 event, excluding HYDJET tracks from the correction determination. For illustration, the derivation
1144 and magnitude of these corrections for inclusive jets at 2.76 TeV are shown in Figs. 29–32.

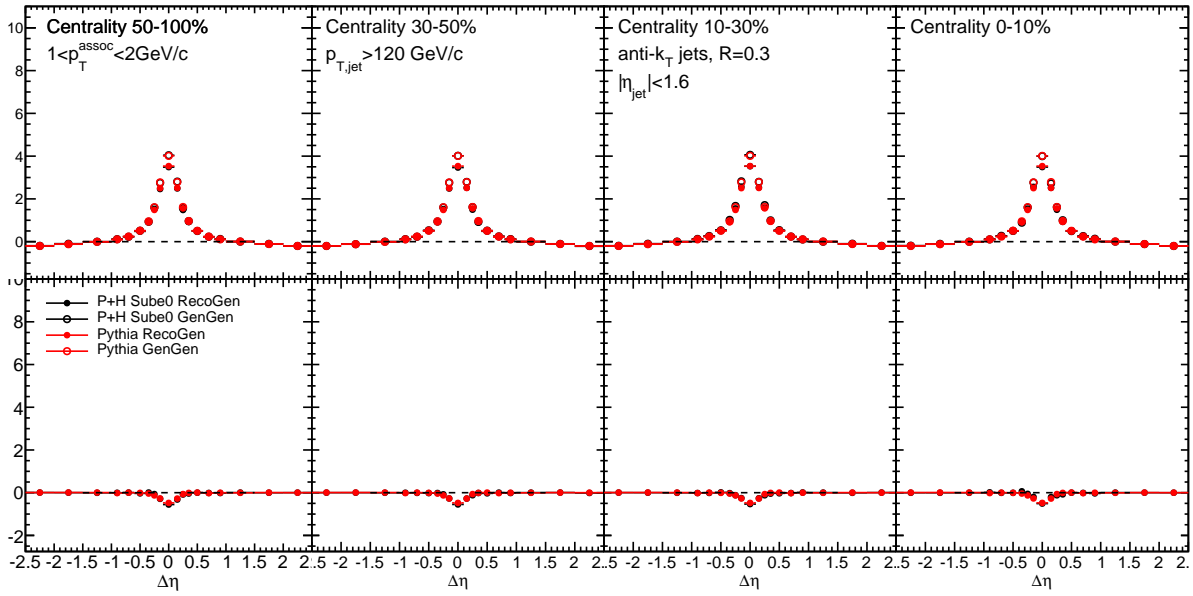


Figure 29. $\Delta\eta$ jet fragmentation function bias corrections derived by comparing correlations between reconstructed vs. generated jets and generated PYTHIA events, with and without embedding into the HYDJET heavy ion environment, for particles $1 < p_T^{\text{trk}} < 2 \text{ GeV}$.

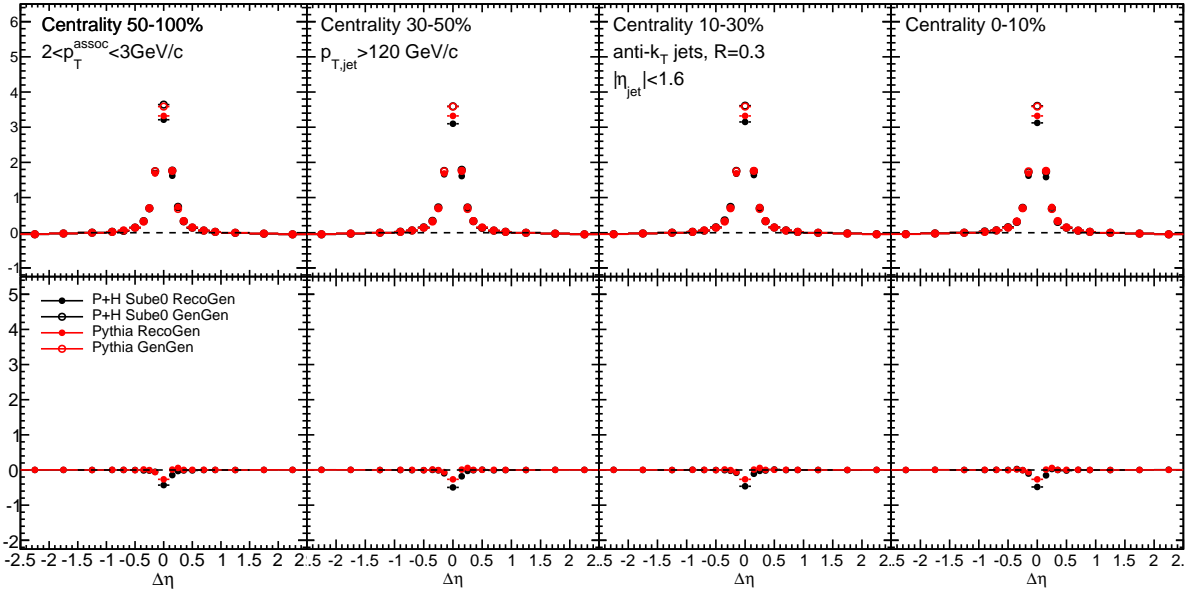


Figure 30. $\Delta\eta$ jet fragmentation function bias corrections derived by comparing correlations between reconstructed vs. generated jets and generated PYTHIA events, with and without embedding into the HYDJET heavy ion environment, for particles $2 < p_T^{\text{trk}} < 3 \text{ GeV}$.

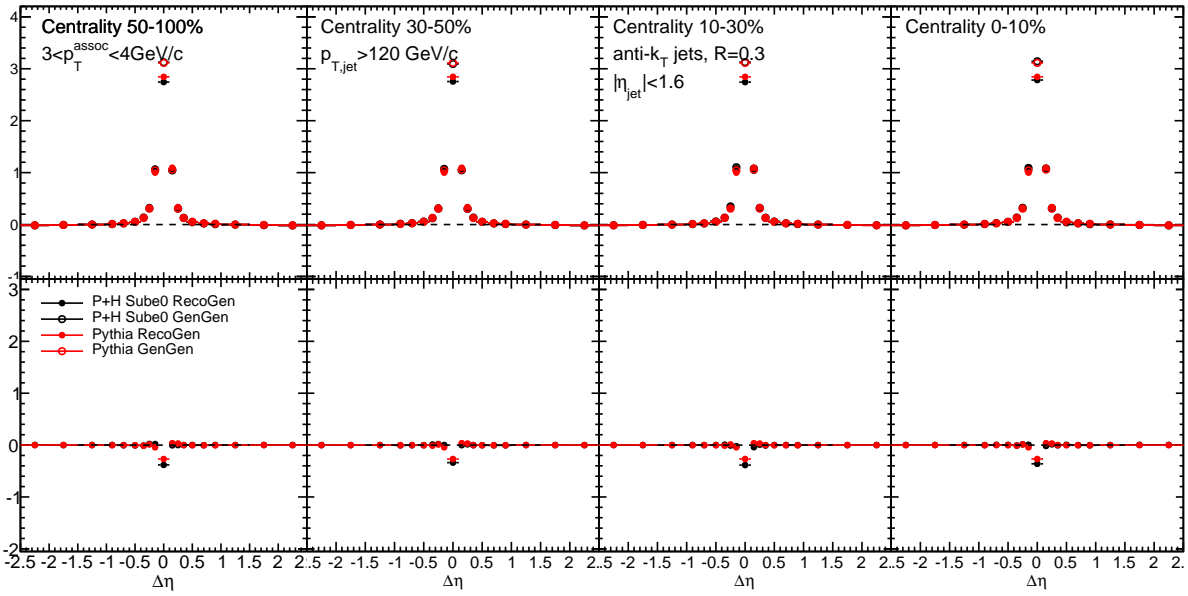


Figure 31. $\Delta\eta$ jet fragmentation function bias corrections derived by comparing correlations between reconstructed vs. generated jets and generated PYTHIA events, with and without embedding into the HYDJET heavy ion environment, for particles $3 < p_T^{\text{trk}} < 4 \text{ GeV}$.

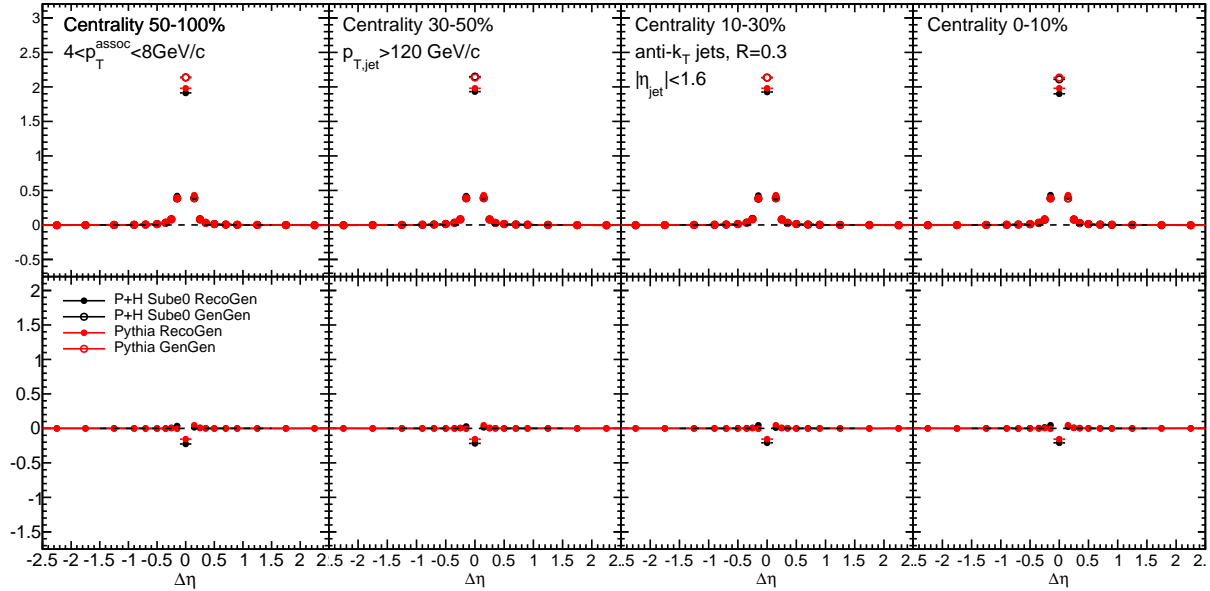


Figure 32. $\Delta\eta$ jet fragmentation function bias corrections derived by comparing correlations between reconstructed vs. generated jets and generated PYTHIA events, with and without embedding into the HYDJET heavy ion environment, for particles $4 < p_T^{\text{trk}} < 8 \text{ GeV}$.

To assess the overall effect of these corrections, the integrated yield of these corrections is shown as a function of transverse momentum and centrality is shown for inclusive, leading, and subleading jets as a function of p_T^{trk} in Fig. 33 and as a function of PbPb centrality in Fig. 34. The correction magnitude shows little centrality dependence, and is very similar for pure PYTHIA simulation and PYTHIA embedded into HYDJET.

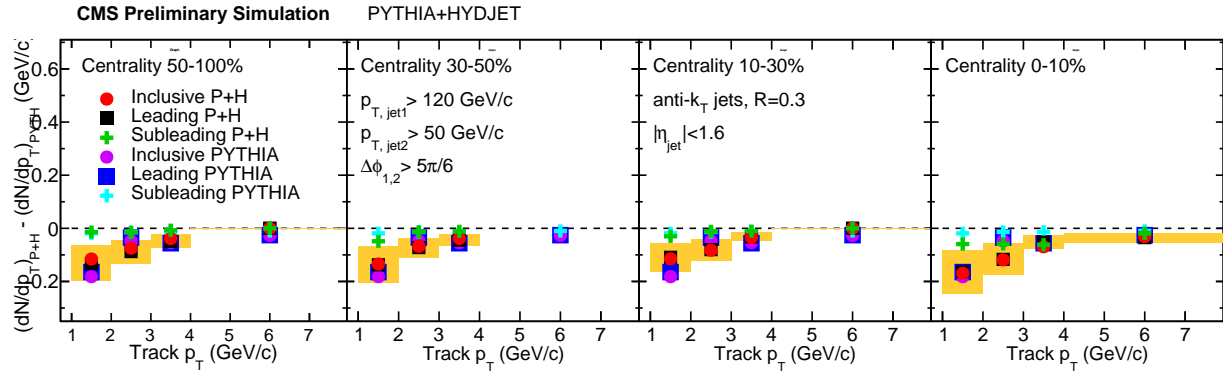


Figure 33. Integrated yield attributed to jet fragmentation function bias in jet reconstruction for PYTHIA alone and embedded into HYDDET, shown as a function of p_T^{trk} for each centrality class.

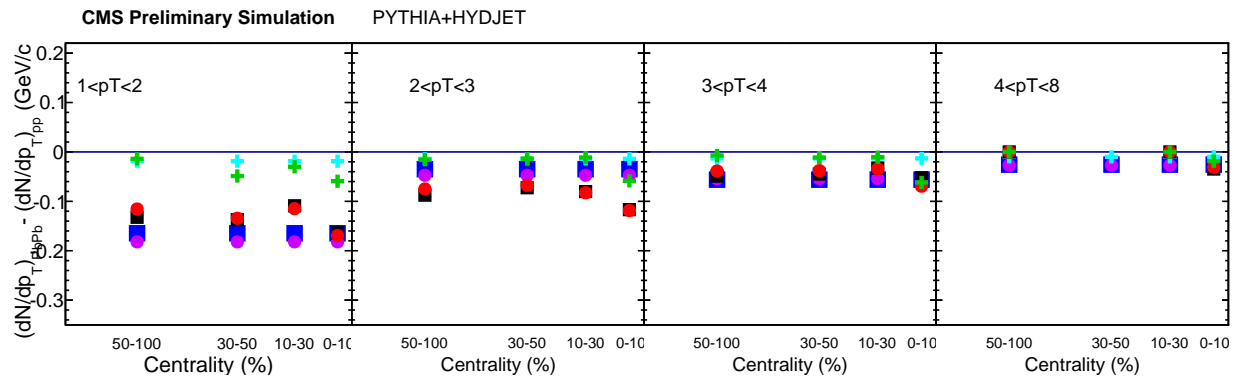


Figure 34. Integrated yield attributed to jet fragmentation function bias in jet reconstruction for PYTHIA alone and embedded into HYDDET, shown as a function of centrality for each associate track p_T range.

1150 **9.5 Background fluctuation bias correction**

1151 In central PbPb collisions background levels are very high, and naturally fluctuate throughout
1152 the event. As discussed in Section 7, the process of jet reconstruction in PbPb collisions includes
1153 background subtraction that accounts for the general distribution of energy in the event. However,
1154 small, local variations in background levels remain (on the order of 5 GeV within a radius of $R =$
1155 0.3). These are reconstructed into the jet, raising or lowering the measured jet energy depending
1156 on whether the jet sits on an upward or a downward fluctuation in the background. As a result,
1157 jets with “true” p_T slightly below the 120 GeV selection threshold that sit on upward background
1158 fluctuations will be included in the sample, while jets sit on downward will be excluded. Because
1159 the jet spectrum is steeply falling, it is much more common for a lower- p_T jet (on an upward
1160 fluctuation) to be included in the sample than for a higher- p_T jet to be excluded. This results in
1161 the systematic inclusion of tracks from background fluctuations in the peak of tracks observed about
1162 the jet axis, resulting in a contribution to the initially measured jet peak that must be accurately
1163 quantified and subtracted.

1164 To estimate and subtract the contribution to the excess yield due to background fluctuation
1165 bias in jet reconstruction to the measured excess yield, we perform simulations in PYTHIA+HYDJET
1166 samples with reconstructed jets (but generated tracks, as the tracking efficiency uncertainty is
1167 analyzed separately), and construct correlations excluding particles generated with the embedded
1168 PYTHIA hard-scattering process. As the PYTHIA+HYDJET simulation does not include interactions
1169 between the PYTHIA hard process and the medium, this procedure by construction isolates the
1170 contribution to the jet peak that is attributable to the background fluctuation bias. The resulting
1171 corrections are illustrated in Fig. 35 - Fig. 38 for inclusive jets at 2.76 TeV. These correlations show
1172 a diminishing effect with increasing particle transverse momentum. We subtract the gaussian fit
1173 to these correlations bin-by-bin from the data results, and also assign the half its magnitude as
1174 systematic uncertainty to the final measurements. To assess the overall effect of these corrections,
1175 the integrated yield of these corrections is shown in Fig. 39 as a function of transverse momentum
1176 and centrality is shown for inclusive, leading, and subleading jets at 2.76 TeV.

1177 Considering that the background fluctuation bias effect in many ways mimics the jet peak
1178 signal, it is particularly important to validate this correction and confirm both that its origin

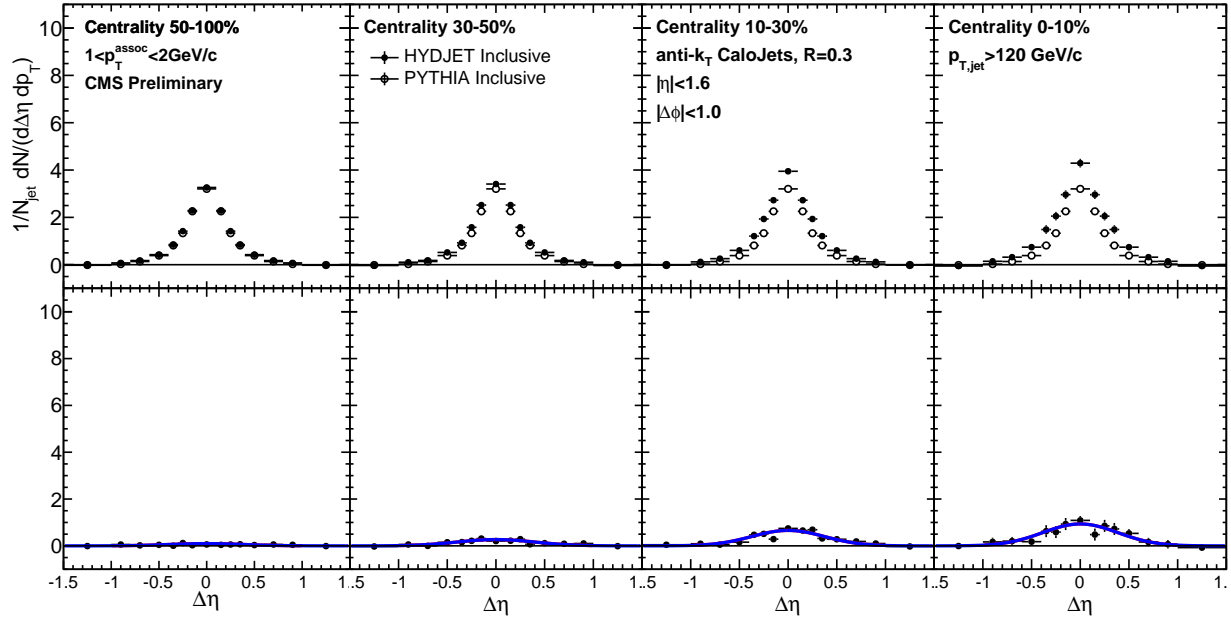


Figure 35. $\Delta\eta$ background fluctuation bias correction for inclusive jets derived by constructing correlations in PYTHIA+HYDJET between reconstructed jets and only those tracks simulated as part of the heavy ion underlying event rather than the embedded PYTHIA hard process, for particles $1 < p_T^{\text{trk}} < 2 \text{ GeV}$

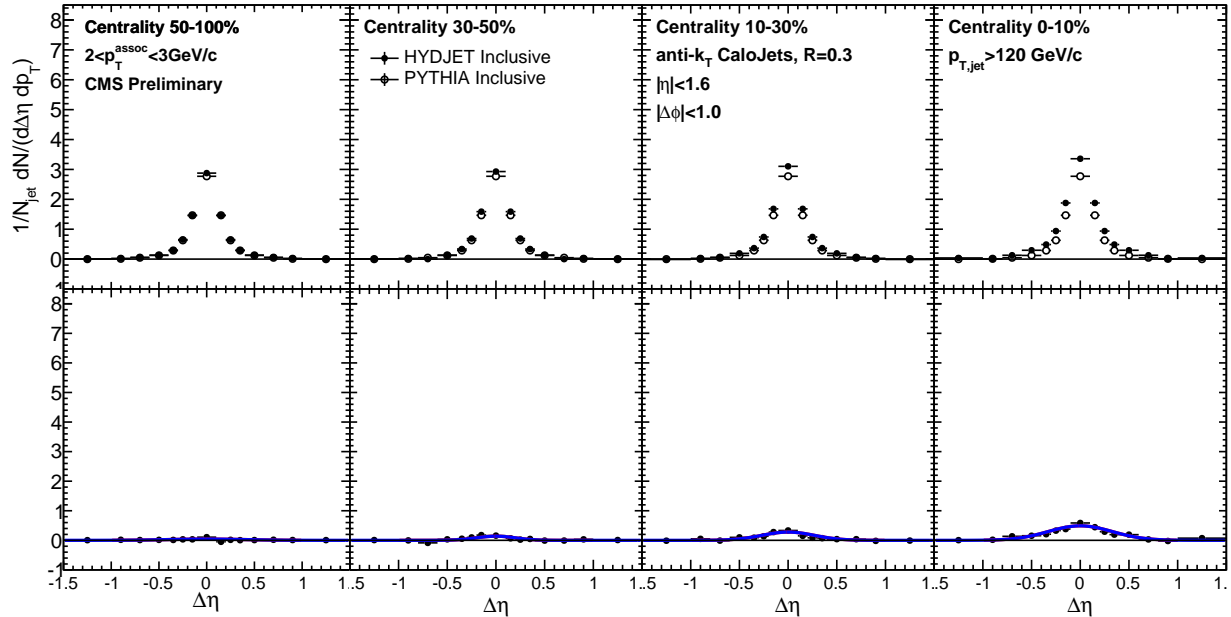


Figure 36. $\Delta\eta$ background fluctuation bias correction for inclusive jets derived by constructing correlations in PYTHIA+HYDJET between reconstructed jets and only those tracks simulated as part of the heavy ion underlying event rather than the embedded PYTHIA hard process, for particles $2 < p_T^{\text{trk}} < 3 \text{ GeV}$

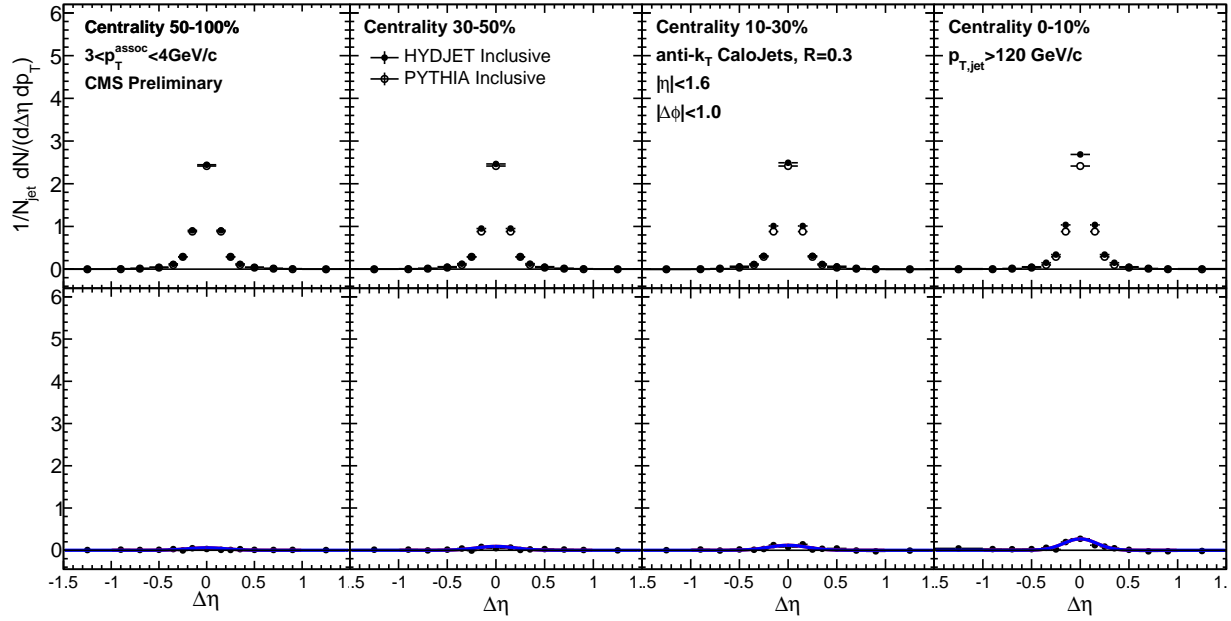


Figure 37. $\Delta\eta$ background fluctuation bias correction for inclusive jets derived by constructing correlations in PYTHIA+HYDJET between reconstructed jets and only those tracks simulated as part of the heavy ion underlying event rather than the embedded PYTHIA hard process, for particles $3 < p_T^{\text{trk}} < 4 \text{ GeV}$

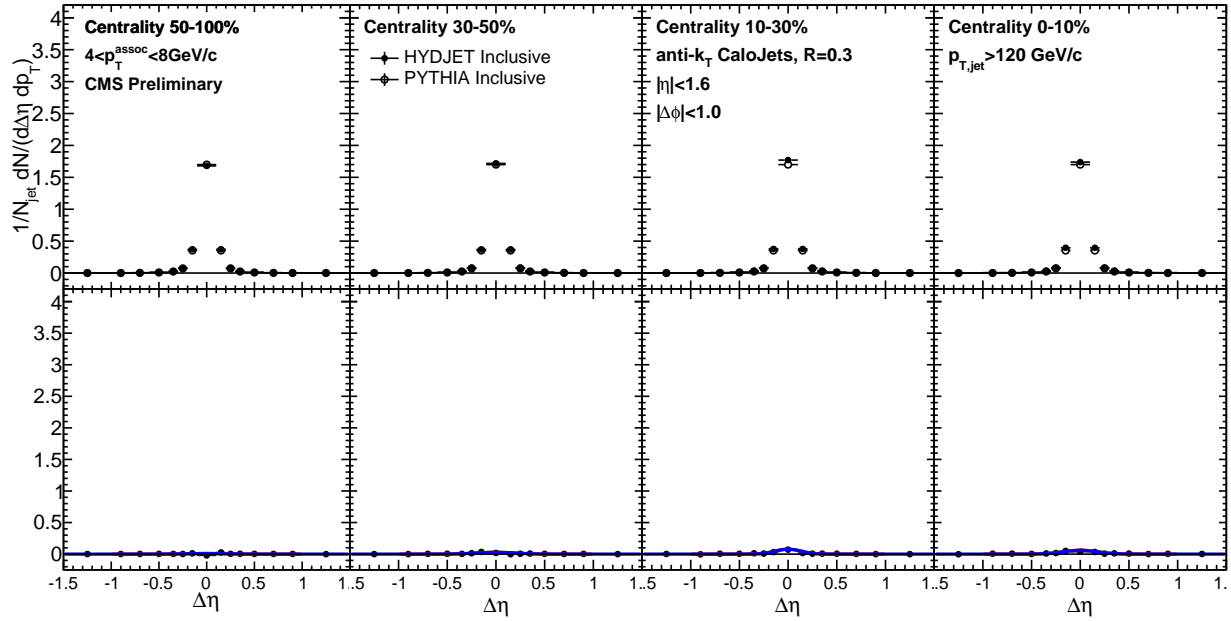


Figure 38. $\Delta\eta$ background fluctuation bias correction for inclusive jets derived by constructing correlations in PYTHIA+HYDJET between reconstructed jets and only those tracks simulated as part of the heavy ion underlying event rather than the embedded PYTHIA hard process, for particles $4 < p_T^{\text{trk}} < 8 \text{ GeV}$

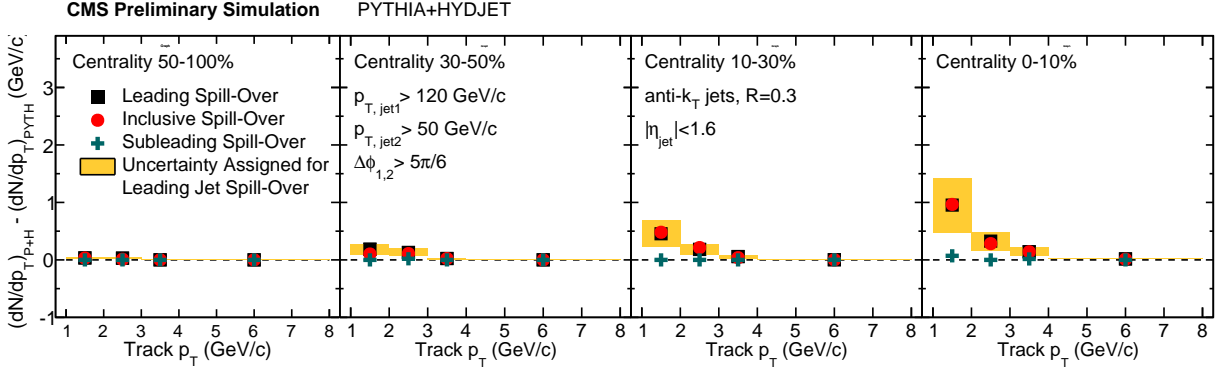


Figure 39. Integrated yield attributed to background fluctuation bias in the selection of inclusive and leading jets, shown as a function of associate track p_T for each centrality class.

is well-understood and that the HYDJET simulation used to derive it reproduces the background fluctuations in data closely enough to accurately obtain corrections. To check this, we extract a direct estimate of the effect from data using a “pseudo-embedding” of pp jets into a minimum bias PbPb data sample. The goal of this study is to verify that we recover a similar magnitude of excess yield as we attribute based on our more detailed PYTHIA+HYDJET simulations. Here we approximate the effect by adding the total transverse momentum in a circle of radius $R = 0.3$ around all jets with $p_T > 90$ GeV, and considering the total deviation up or down of this $(\Sigma p_T)_{\text{cone}}$ from the average total transverse momentum $\langle (\Sigma p_T)_{\text{cone}} \rangle$. First, we may directly compare the average p_T and fluctuations in p_T in these random cones between data and Monte Carlo. We find that our Monte Carlo approximately reproduces the data: in data $\langle (\Sigma p_T)_{\text{cone,data}} \rangle = 10.0$ GeV, with $\sigma((\Sigma p_T)_{\text{cone,data}}) = 4.9$ GeV, while in Monte Carlo $\langle (\Sigma p_T)_{\text{cone,MC}} \rangle = 11.9$ GeV, with $\sigma((\Sigma p_T)_{\text{cone,data}}) = 5.6$ GeV.

We then use these random cones to adjust jet energy and re-select jets: we add the deviation up or down of this $(\Sigma p_T)_{\text{cone}}$ to each embedded pp jets with this adjusted p_T . We then fill $\Delta\eta - \Delta\phi$ correlations to all jets that pass our nominal $p_T > 120$ GeV jet selection cut. We apply this technique to both our PYTHIA+HYDJET sample and a minimum-bias PbPb data sample to measure the charged particle yield associated with the embedded jet axis as a result of the jet fluctuation bias. As Fig. 40–41 show, this data pseudo-embedding recovers the same magnitude of excess yield due to background fluctuation bias as our nominal Monte Carlo studies, but artificially confines this

1198 effect to a $R = 0.3$ cone by construction, due to the artificially simple jet reconstruction procedure.

1199 This gives confidence that the origin and magnitude of the effect are well-understood.

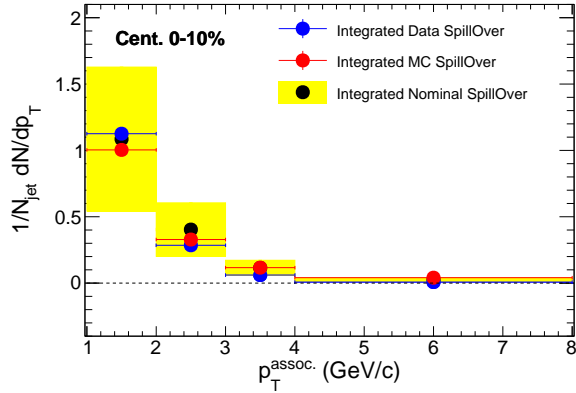


Figure 40. Total integrated magnitude of background fluctuation bias as simulated with pp jets embedded in Minimum Bias events (blue points) compared to the effect as simulated with PYTHIA jets into minimum bias HYDJET and to nominal corrections obtained with full PYTHIA+HYDJET simulation. Nominal systematic errors of +/- 50% as assigned in this analysis are shown as yellow systematic error bars on nominal (full MC simulation) points.

1200 The background fluctuation bias could also be sensitive to the same calorimeter nonlinearity
1201 bias that necessitates fragmentation-jet energy corrections. To study this question and validate the
1202 uncertainty associated with this correction, we separately study the effect for quark jets and gluon
1203 jets, as shown in Figure 42. We find that this bias affects gluon jets slightly more than quark jets,
1204 consistent with deterioration of jet reconstruction performance for broader/softer jets, but that
1205 these deviations are within the 50% systematic uncertainty assigned.

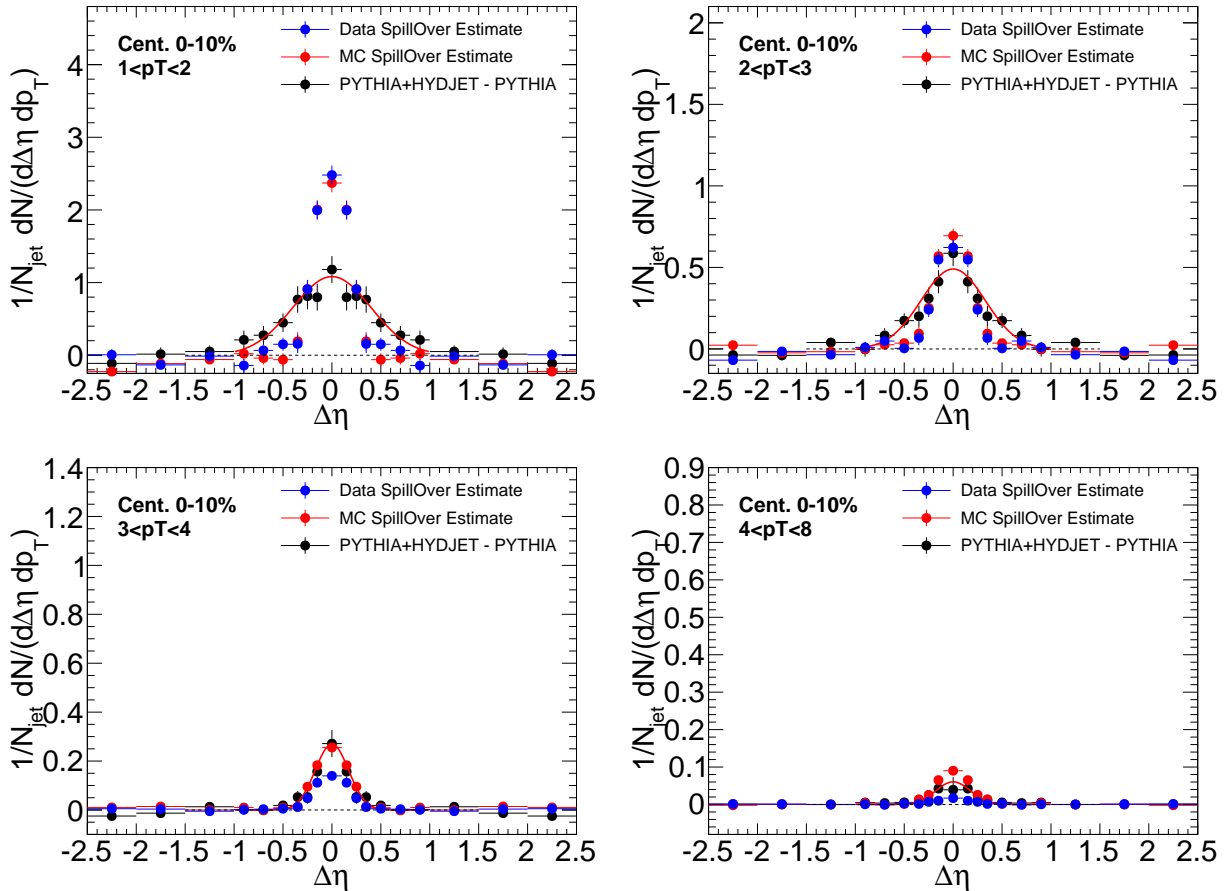


Figure 41. Correlated yield $\Delta\eta$ due to background fluctuation bias as simulated with pp jets embedded in Minimum Bias events (blue points) compared to the effect applying the same technique with PYTHIA jets in HYDJET minimum bias events, as well as in full PYTHIA+HYDJET simulation (black points with red fit line).

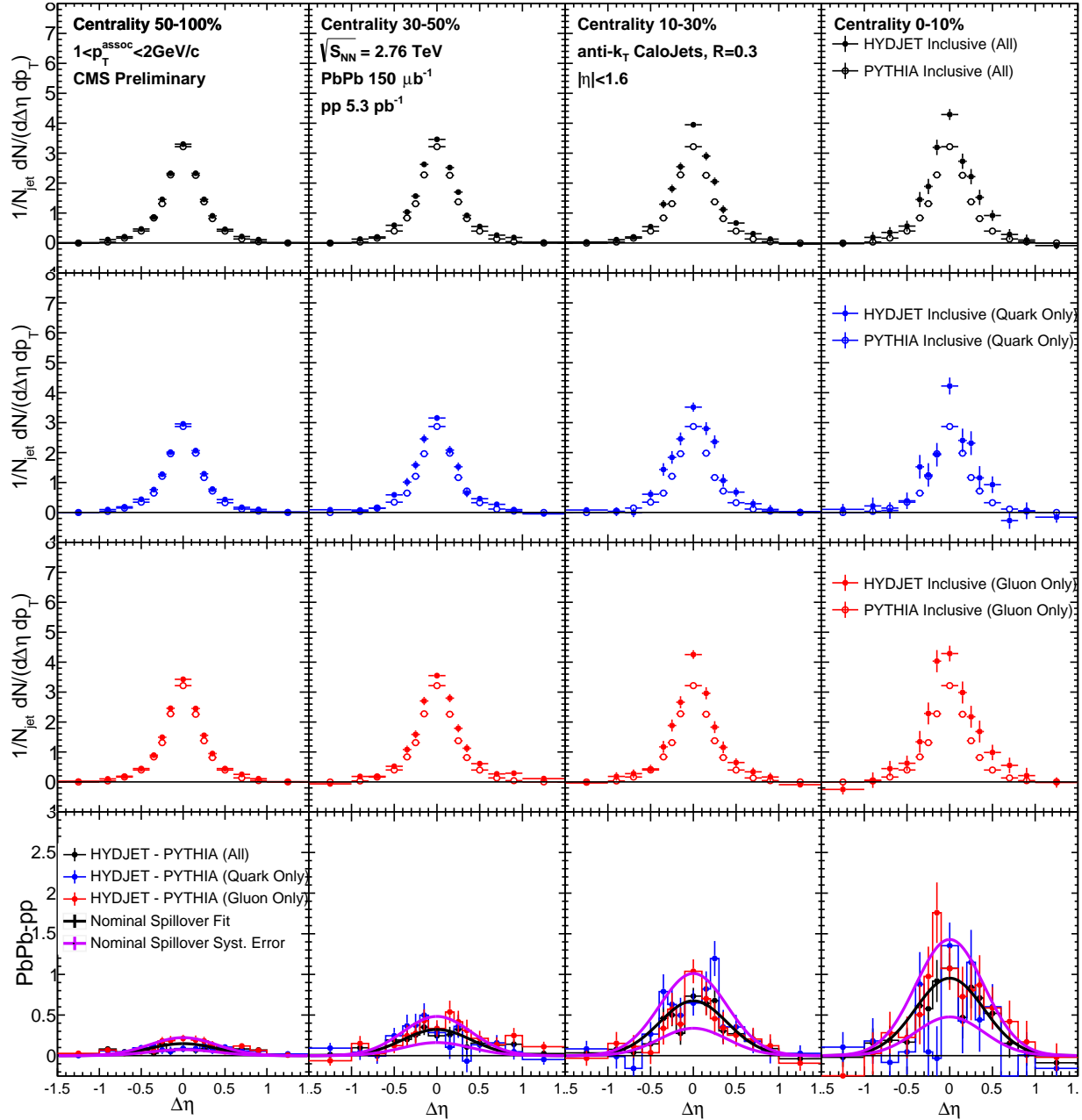


Figure 42. Comparison of magnitude of background selection bias effect for quark and gluon jets versus our nominal sample. Jet selection is inclusive in all cases.

1206 **9.6 Evaluation of systematic uncertainties**

1207 A number of sources of systematic uncertainty have been discussed in presenting jet and track
1208 reconstruction and the jet-track correlation analysis procedure. To estimate the total systematic
1209 uncertainty in these measurements, these contributions are added in quadrature. A brief summary
1210 of all systematic uncertainty contributions, together with the procedure used to estimate their
1211 magnitude follows. The contributions from each source (relative to jet peak signal) are summarized
1212 in Tables [V](#)–[VII](#).

1213 **9.6.1 Systematic uncertainties related to jet reconstruction**

1214 Jet reconstruction-related sources of systematic uncertainty in this analysis include the two recon-
1215 struction biases as discussed above, as well uncertainty associated with the jet energy scale (JES)
1216 evaluation. We consider three sources of uncertainty on the JES: (1) differences in calorimeter
1217 response for quark versus gluon jets, meaning that medium-induced changes in jet flavor could
1218 result in either over-correction or under-correction of jet energy and a resulting bias in jet selection
1219 (evaluated via Monte Carlo non-closure for quark and gluon jets); (2) possible differences between
1220 data and simulation; (3) uncertainty due to quenching effects not included in our HYDJET simula-
1221 tion. To evaluate how each of these sources of JES uncertainty affects final correlations, we vary jet
1222 selection threshold by the combined uncertainty, and then quantify the resulting differences in the
1223 final correlations as a measure of the combined residual JES uncertainty. Since all the measured
1224 correlations are studied per-reconstructed jets, the jet reconstruction efficiency does not contribute
1225 to the systematic uncertainty of this measurement.

1226 **9.6.2 Systematic uncertainties related to tracking and tracking efficiency corrections**

1227 The tracking efficiency correction uncertainty is estimated from the ratio of corrected reconstructed
1228 yields and generated yields by using generator level charged particles as a “truth” reference. To ac-
1229 count for the possible track reconstruction differences in data and simulation, a residual uncertainty
1230 in track reconstruction efficiency and fake rate corrections is also estimated.

1231 **9.6.3 Systematic uncertainty associated with pair acceptance correction and event
1232 decomposition**

1233 Uncertainty arising from pair-acceptance effects is estimated by considering the sideband asymme-
1234 try after dividing by the mixed-event background. Each sideband region of the final $\Delta\eta$ distribution
1235 ($-2.5 < \Delta\eta < -1.5$ and $1.5 < \Delta\eta < 2.5$) is separately fit with a horizontal line after background
1236 subtraction. The greater of these two deviations from zero is assigned as systematic error. Un-
1237 certainties resulting from the background subtraction are determined by considering the average
1238 point-to-point deviation in two parts of the sideband region ($1.5 < |\Delta\eta| < 2.0$ and $2.0 < |\Delta\eta| < 2.5$)
1239 after background subtraction. The derivations of both of these sources of uncertainty are illustrated
1240 in Appendix C. In PbPb data this background subtraction uncertainty is greatest for the most cen-
1241 tral events (0–10%) and the lowest track p_T bin where the background is most significant compared
1242 to the signal level, and decreases for less central collisions and for higher p_T tracks ($p_T^{\text{trk}} > 2$ GeV).

1243 **9.6.4 Summary of systematic uncertainties**

1244 The contributions to total systematic uncertainty from each of the sources described above are given
1245 in Tables V–VII. Table V gives uncertainty evaluations for correlation studies at 2.76 TeV, while
1246 Table VI gives the same for studies at 5.02 TeV. Finally, Table VII gives uncertainty evaluations
1247 for balanced ($A_J < 0.22$) and unbalanced ($A_J > 0.22$) dijet events in momentum balance studies
1248 at 2.76 TeV.

TABLE V. Systematic uncertainties in the measurement of the jet-track correlations in PbPb and pp collisions at 2.76 TeV, as percentage of the total measured correlated yield. The numbers presented in this table summarize the range of values of systematic uncertainty (as a function of p_T^{trk}) for different centrality bins.

Source	0–10%	10–30%	30–50%	50–100%	pp
Background fluctuation bias	3–12%	2–7%	1–5%	0–1%	–
Jet fragmentation function bias	0–2%	0–2%	0–2%	0–2%	0–2%
Residual jet energy scale	3%	3%	3%	3%	3%
Tracking efficiency uncertainty	4%	4%	4%	4%	3 %
Residual track efficiency corr.	5%	5%	5%	5%	5%
Pair acceptance corrections	5–9%	5–9%	4–8%	2–6%	2–3%
Background subtraction	2–5%	2–5%	2–5%	2–5%	1–2%
Total	9–17%	9–14%	8–13%	8–10%	7–8%

TABLE VI. Systematic uncertainties in the measurement of the jet track correlations in PbPb and pp collisions at 5.02 TeV. The numbers presented in this table summarize typical range of systematic uncertainty as a function of collision centrality. The upper limits of the cited values correspond to uncertainties at lowest p_T^{trk} , and uncertainties decrease with rising p_T^{trk} .

Source	0–10%	10–30%	30–50%	50–100%	ppRef
Background fluctuation bias	0–10%	0–5%	0–2%	0–1%	–
Background fluctuation bias residual	0–2%	0–3%	0–1%	0–1%	–
JFF bias	3–5%	3–4%	3–4%	3–4%	3%
Residual JES	4%	4%	4%	4%	4%
Tracking efficiency uncertainty	1%	1%	1%	1%	1%
Residual tracking efficiency	5%	5%	5%	5%	5%
Pair-acceptance corrections	1–5%	1–4%	1–4%	1–4%	1–2%
Event decomposition	1–9%	0–4%	0–4%	0–3%	0–3%
Total	7–16%	7–11%	7–9%	7–9%	7–8%

TABLE VII. This table summarizes the systematic uncertainties in the measurement of the p_T^{trk} correlations in PbPb and pp collisions at 2.76 TeV. Upper and lower limits are shown as a function of collision centrality. Upper values correspond to the uncertainties at lowest p_T^{trk} .

Source	0–30%	30–50%	50–100%	pp
Balanced jet selection ($A_J < 0.22$):				
Background fluctuations	1–8%	1–3%	0–1%	–
JFF bias and jet swapping	0–2%	0–2%	0–2%	0–2%
Residual JES	3%	3%	3%	3%
Tracking efficiency	4%	4%	4%	3 %
Residual track efficiency corr.	5%	5%	5%	5%
Pair acceptance corrections	5–9%	4–8%	2–6%	2–3%
Event decomposition	2–5%	2–5%	2–5%	1–2%
Total	9–15%	8–13%	8–10%	7–8%
Unbalanced jet selection ($A_J > 0.22$):				
Background fluctuations	1–10%	1–5%	0–2%	–
JFF bias and jet swapping	0–2%	0–2%	0–2%	0–2%
Residual JES	3%	3%	3%	3%
Tracking efficiency	4%	4%	4%	3 %
Residual track efficiency corr.	5%	5%	5%	5%
Pair acceptance corrections	5–9%	4–8%	2–6%	2–3%
Event decomposition	2–5%	2–5%	2–5%	1–2%
Total	9–16%	8–13%	8–10%	7–8%

10 DISCUSSION OF RESULTS

1250 Jet-track correlation studies can produce measurements of the density of particles (in each p_T^{trk}
 1251 class) with respect to the jet axis and can also, by creating correlations weighted per-track by
 1252 its p_T^{trk} , produce measurements of the distribution of p_T^{trk} in the event as a whole. Both types of
 1253 measurements are presented here, for inclusive selections of jets with $p_T > 120$ GeV at 2.76 TeV
 1254 and 5.02 TeV, and for high- p_T dijet events at 2.76 TeV. First, particle density correlation results are
 1255 presented in Secs. 10.1- 10.2. Next, p_T^{trk} distributions are used to extract measurements of jet shapes
 1256 (the transverse momentum profiles of jets) in Sec. 10.3. Finally, in Sec. 10.4, p_T^{trk} distributions are
 1257 used to decompose and analyze the hemisphere momentum balance in dijet events.

1258 **10.1 Inclusive jet particle density correlation results**

1259 Particle density correlation studies allow for the detailed characterization of jet fragmentation,
 1260 and of medium-induced modifications to jet fragmentation in PbPb data (as a function of collision
 1261 centrality) compared to pp data. The analysis procedure described in Sec. 9 results in fully-corrected
 1262 2D jet peaks in $\Delta\eta - \Delta\phi$, which may then be projected to obtain the distribution of particles in
 1263 each p_T^{trk} class as a function of $\Delta\eta$ or $\Delta\phi$. The top panels of Figs. 43-50 show these $\Delta\eta$ and
 1264 $\Delta\phi$ distributions (projected over $|\Delta\phi| < 1$ and $|\Delta\eta| < 1$, respectively) for 2.76 TeV pp data and
 1265 PbPb data in each p_T^{trk} range from 1–2 GeV (Fig. 43-44) up to 4–8 GeV (Fig. 49-50). The bottom
 1266 panels of these figures show the differences PbPb–pp for illustration of medium modifications to jet
 1267 fragmentation patterns. In both the $\Delta\eta$ and $\Delta\phi$ dimensions, centrality-dependent excesses of soft
 1268 (low- p_T^{trk}) particles are evident. These exhibit the greatest modifications in the most central PbPb
 1269 collisions, decreasing with centrality until the most peripheral collisions show little modification
 1270 when compared to pp data. These excesses decrease with increasing p_T^{trk} , until in the 4–8 GeV
 1271 range the enhancements evident at lowest- p_T^{trk} reverse to possible slight depletion. In both $\Delta\eta$ and
 1272 $\Delta\phi$ dimensions, the soft excesses exhibit a gaussian-like distribution around the jet axis, while also
 1273 extending to large angles $\Delta\eta = 1$ and $\Delta\phi = 1$ at lowest p_T^{trk} .

1274 Figures 51 and 52 show the corresponding $\Delta\eta$ and $\Delta\phi$ distributions at 5.02 TeV. Here,
 1275 the distribution of particles in each p_T^{trk} class are stacked (with lowest- p_T^{trk} particles on top), and
 1276 pp data shown separately at left. Again the differences PbPb–pp are shown in bottom panels to

illustrate the medium modifications, and exhibit similar qualitative trends to those described above
 for 2.76 TeV results. Results may also be presented as a function of radial distance from the jet axis
 $\Delta r = \sqrt{\Delta\eta^2 + \Delta\phi^2}$. Figure 53 presents charged particle yields, differentially in p_T^{trk} , as a function
 of Δr . For comparison, the bottom row of each plot shows the difference, PbPb minus pp. This
 shows the particles contributing to a jet fragmentation function measurement within a given radius
 from a jet, and illustrates the radial dependence of modifications extending to at least $\Delta r = 1$.

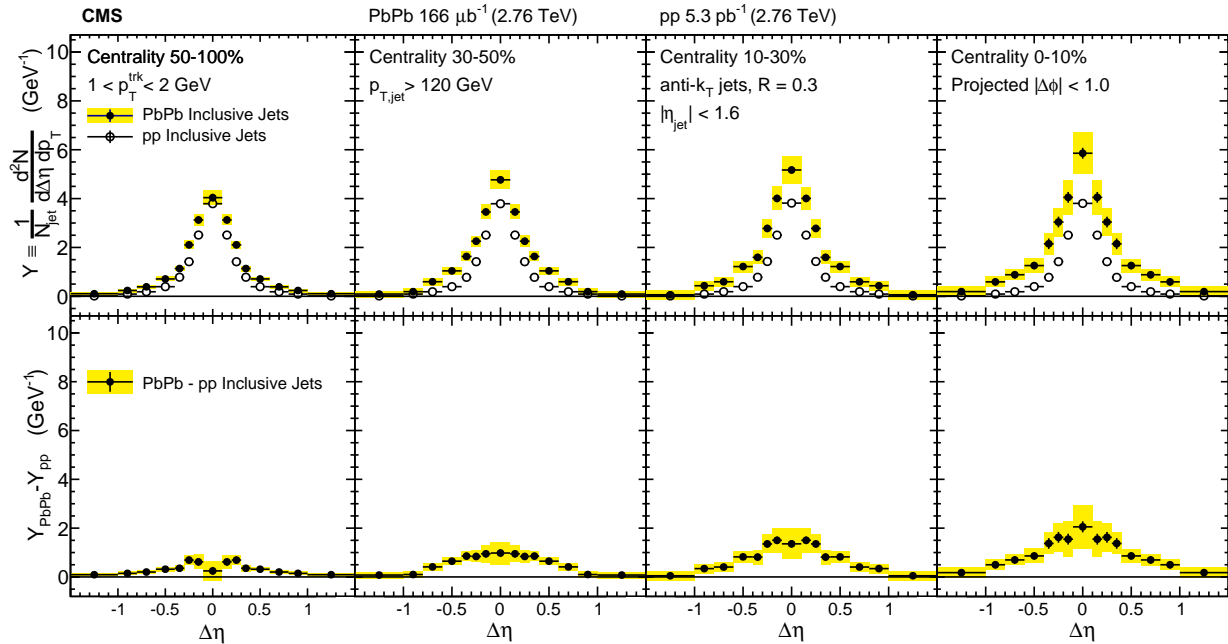


Figure 43. Symmetrized $\Delta\eta$ distributions (projected over $|\Delta\phi| < 1$) of background-subtracted particle yields correlated to PbPb and pp inclusive jets with $p_T > 120$ GeV are shown in the top panels for tracks with $1 < p_T^{\text{trk}} < 2$ GeV. The difference in PbPb and pp per-jet yields is shown in the bottom panels. The total systematic uncertainties are shown as shaded boxes, and statistical uncertainties are shown as vertical bars (often smaller than the symbol size).

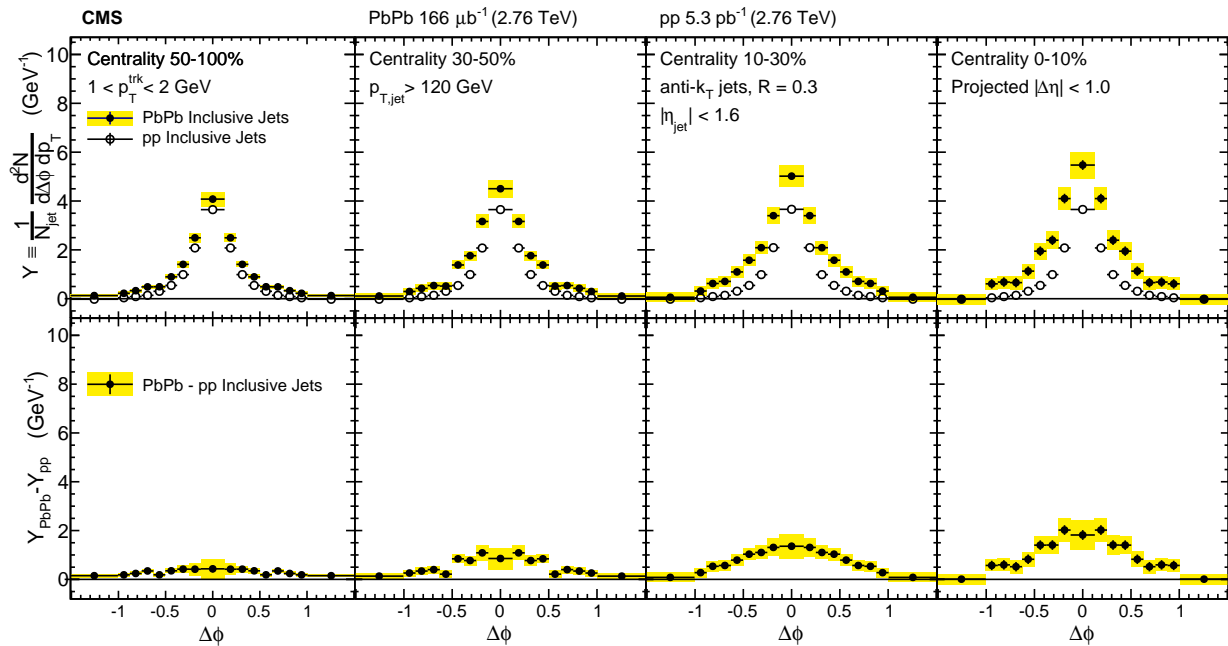


Figure 44. Symmetrized $\Delta\phi$ distributions (projected over $|\Delta\eta| < 1$) of background-subtracted particle yields correlated to PbPb and pp inclusive jets with $p_{\text{T}} > 120 \text{ GeV}$ are shown in the top panels for tracks with $1 < p_{\text{T}}^{\text{trk}} < 2 \text{ GeV}$. The difference in PbPb and pp per-jet yields is shown in the bottom panels. The total systematic uncertainties are shown as shaded boxes, and statistical uncertainties are shown as vertical bars (often smaller than the symbol size).

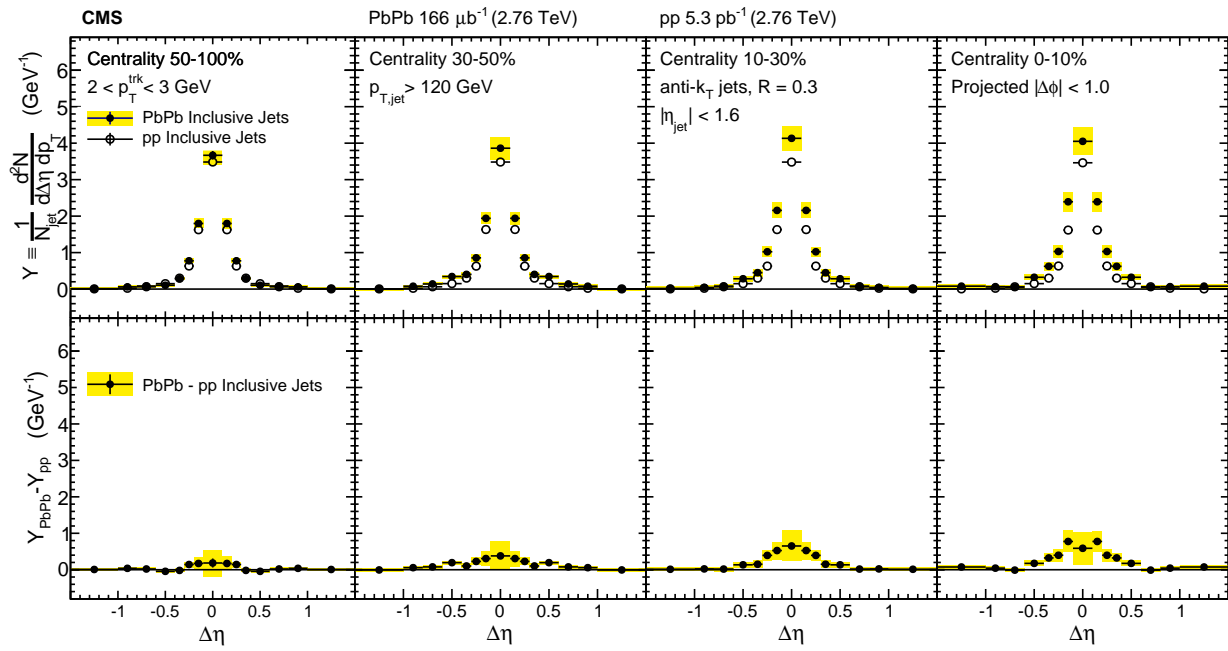


Figure 45. Symmetrized $\Delta\eta$ distributions (projected over $|\Delta\phi| < 1$) of background-subtracted particle yields correlated to PbPb and pp inclusive jets with $p_{\text{T}} > 120 \text{ GeV}$ are shown in the top panels for tracks with $2 < p_{\text{T}}^{\text{trk}} < 3 \text{ GeV}$. The difference in PbPb and pp per-jet yields is shown in the bottom panels. The total systematic uncertainties are shown as shaded boxes, and statistical uncertainties are shown as vertical bars (often smaller than the symbol size).

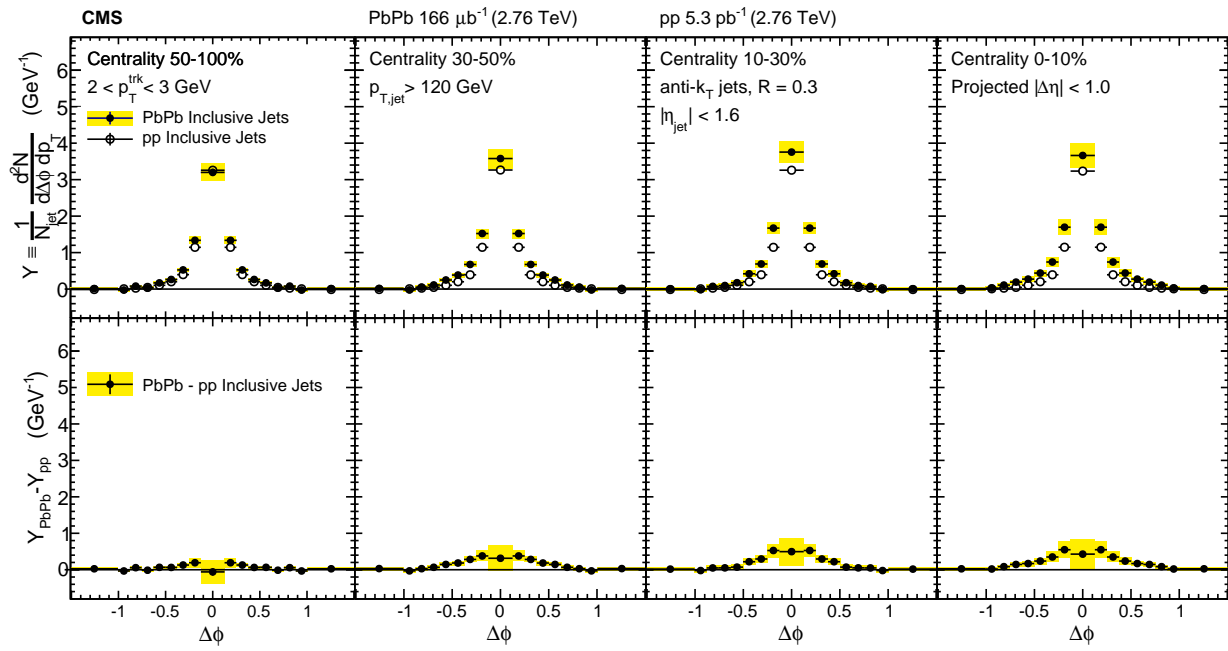


Figure 46. Symmetrized $\Delta\phi$ distributions (projected over $|\Delta\eta| < 1$) of background-subtracted particle yields correlated to PbPb and pp inclusive jets with $p_T > 120 \text{ GeV}$ are shown in the top panels for tracks with $2 < p_T^{\text{trk}} < 3 \text{ GeV}$. The difference in PbPb and pp per-jet yields is shown in the bottom panels. The total systematic uncertainties are shown as shaded boxes, and statistical uncertainties are shown as vertical bars (often smaller than the symbol size).

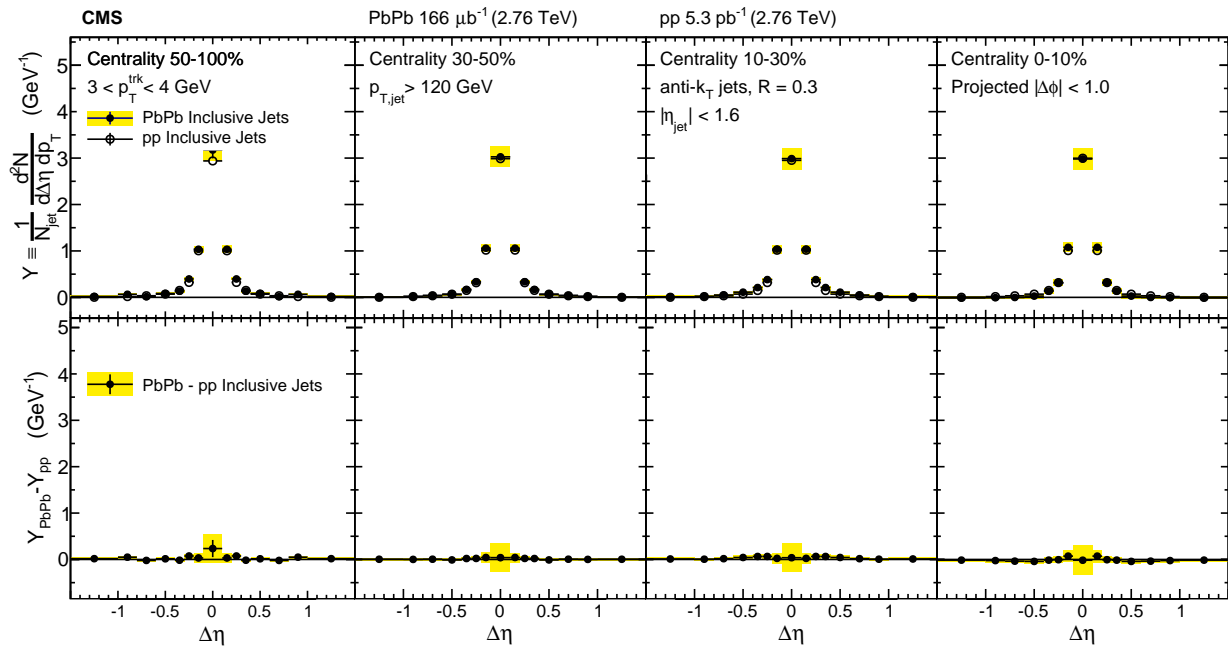


Figure 47. Symmetrized $\Delta\eta$ distributions (projected over $|\Delta\phi| < 1$) of background-subtracted particle yields correlated to PbPb and pp inclusive jets with $p_T > 120 \text{ GeV}$ are shown in the top panels for tracks with $3 < p_T^{\text{trk}} < 4 \text{ GeV}$. The difference in PbPb and pp per-jet yields is shown in the bottom panels. The total systematic uncertainties are shown as shaded boxes, and statistical uncertainties are shown as vertical bars (often smaller than the symbol size).

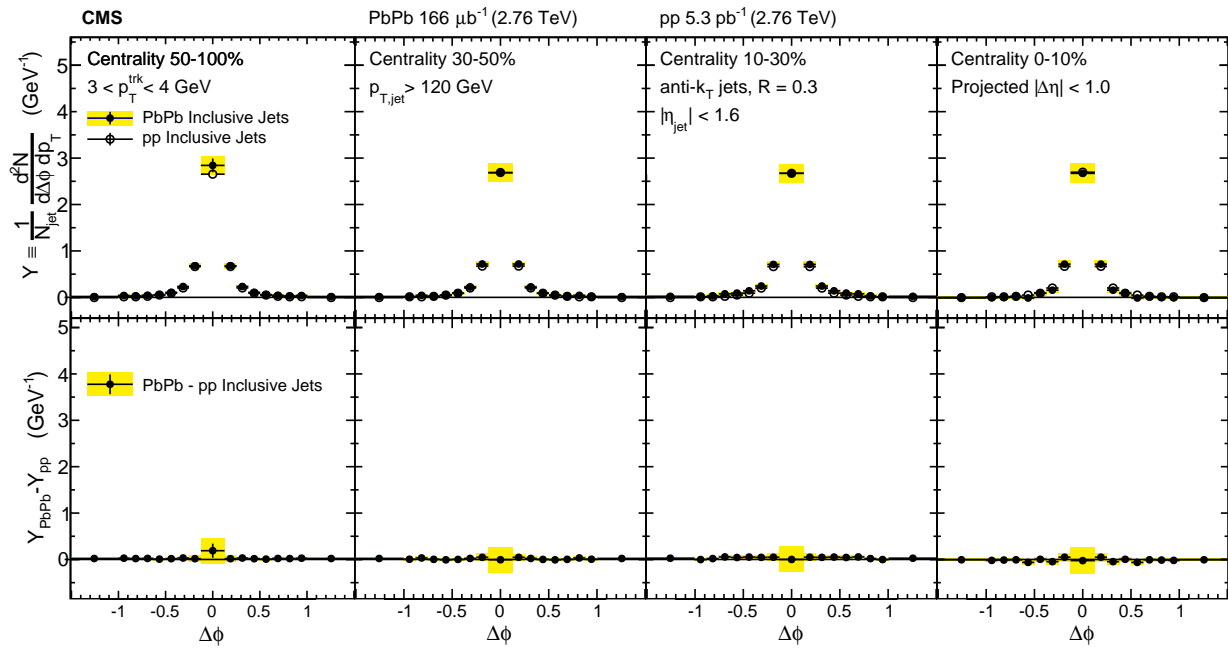


Figure 48. Symmetrized $\Delta\phi$ distributions (projected over $|\Delta\eta| < 1$) of background-subtracted particle yields correlated to PbPb and pp inclusive jets with $p_T > 120$ GeV are shown in the top panels for tracks with $3 < p_T^{\text{trk}} < 4$ GeV. The difference in PbPb and pp per-jet yields is shown in the bottom panels. The total systematic uncertainties are shown as shaded boxes, and statistical uncertainties are shown as vertical bars (often smaller than the symbol size).

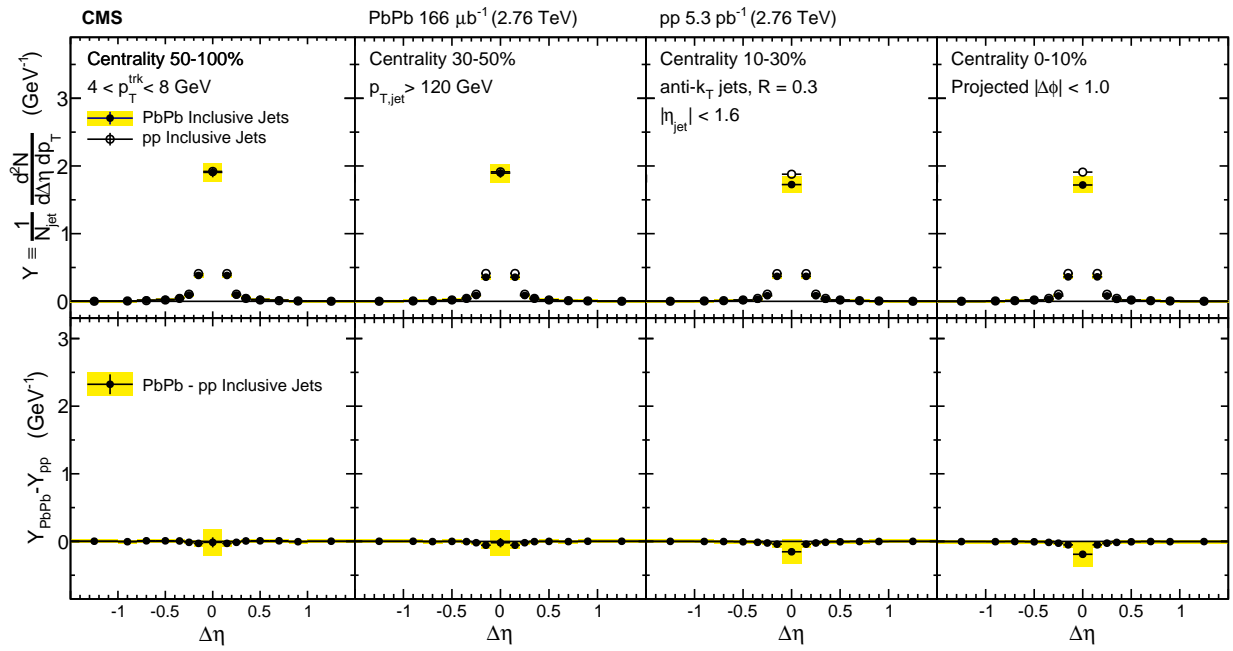


Figure 49. Symmetrized $\Delta\eta$ distributions (projected over $|\Delta\phi| < 1$) of background-subtracted particle yields correlated to PbPb and pp inclusive jets with $p_T > 120 \text{ GeV}$ are shown in the top panels for tracks with $4 < p_T^{\text{trk}} < 8 \text{ GeV}$. The difference in PbPb and pp per-jet yields is shown in the bottom panels. The total systematic uncertainties are shown as shaded boxes, and statistical uncertainties are shown as vertical bars (often smaller than the symbol size).

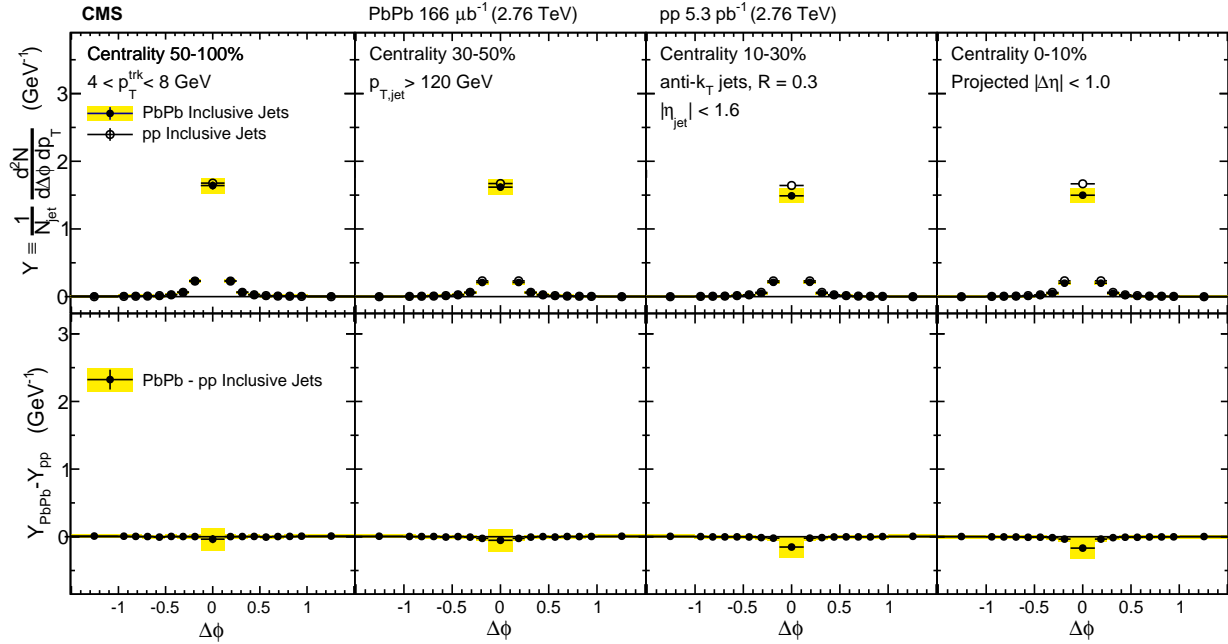


Figure 50. Symmetrized $\Delta\phi$ distributions (projected over $|\Delta\eta| < 1$) of background-subtracted particle yields correlated to PbPb and pp inclusive jets with $p_T > 120$ GeV are shown in the top panels for tracks with $4 < p_T^{\text{trk}} < 8$ GeV. The difference in PbPb and pp per-jet yields is shown in the bottom panels. The total systematic uncertainties are shown as shaded boxes, and statistical uncertainties are shown as vertical bars (often smaller than the symbol size).

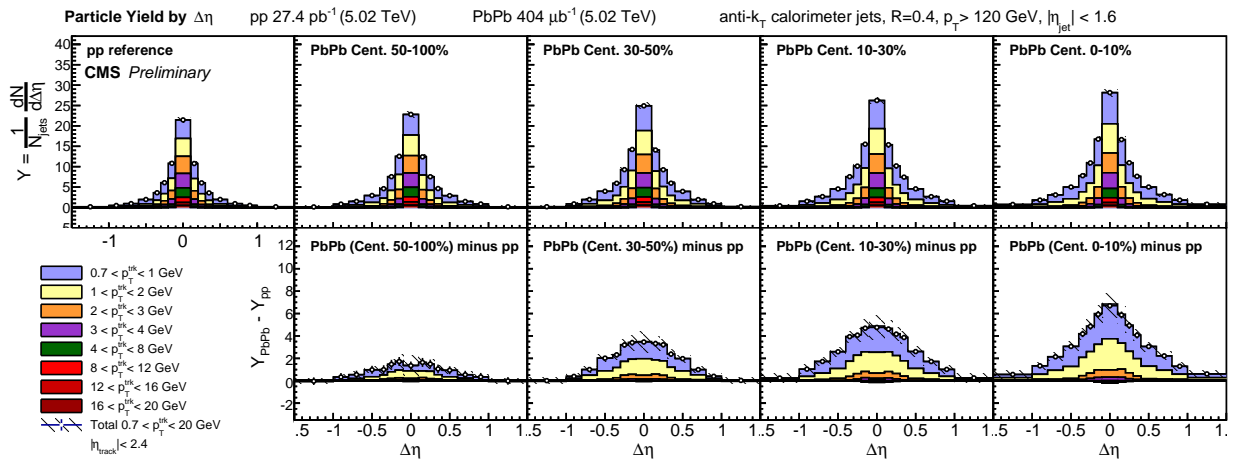


Figure 51. Top row: distributions of charged particle yields correlated to jets with $p_T > 120$ GeV as a function of $\Delta\eta$ (projected over $|\Delta\phi| < 1$), shown differentially for all p_T^{trk} bins for pp, peripheral PbPb, and central PbPb data. Bottom row: PbPb minus pp difference in these distributions. Hatched lines on p_T^{trk} -inclusive points show total systematic uncertainties.

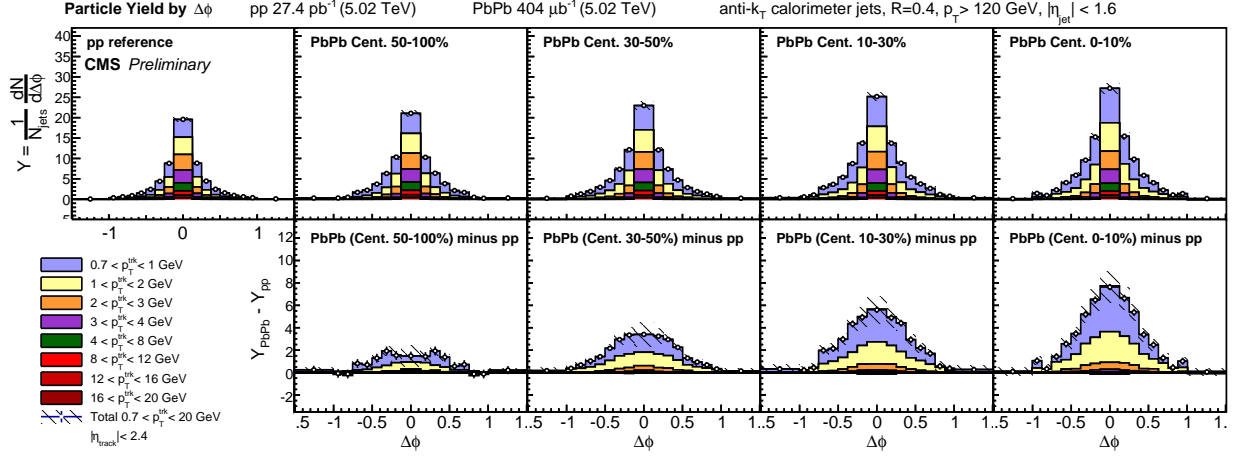


Figure 52. Top row: distributions of charged particle yields correlated to jets with $p_{\text{T}} > 120 \text{ GeV}$ as a function of $\Delta\phi$ (projected over $|\Delta\eta| < 1$), shown differentially for all $p_{\text{T}}^{\text{trk}}$ bins for pp, peripheral PbPb, and central PbPb data. Bottom row: PbPb minus pp difference in these distributions. Hatched lines on $p_{\text{T}}^{\text{trk}}$ -inclusive points show total systematic uncertainties.

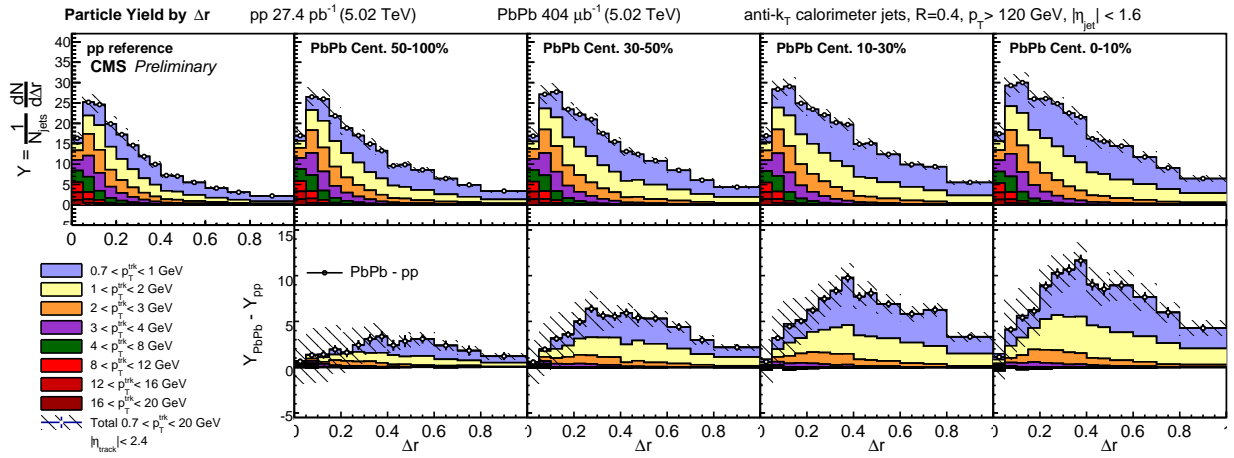


Figure 53. Top row: distributions of charged particle yields correlated to jets with $p_{\text{T}} > 120 \text{ GeV}$ as a function of Δr , shown differentially for all $p_{\text{T}}^{\text{trk}}$ bins. Bottom row: PbPb minus pp difference in these distributions. Hatched lines on $p_{\text{T}}^{\text{trk}}$ -inclusive points show total systematic uncertainties.

To summarize the magnitude of the modifications to particle yields in PbPb relative to pp collisions, integrated yields as a function of p_T^{trk} are presented in the top panel of Fig. 54. The bottom panel of Fig. 54 shows differences PbPb–pp in total integrated particle yields in each p_T^{trk} class for results at 5.02 TeV compared to 2.76 TeV results. This quantifies the low- p_T excess in central PbPb collisions to as many as 4 additional particles (in central PbPb relative to pp reference) per unit of p_T^{trk} in the lowest p_T^{trk} bin. This excess decreases smoothly with p_T^{trk} in each centrality bin, until the 4–8 GeV central PbPb bin is consistent with or slightly depleted relative to pp reference. For tracks with $p_T^{\text{trk}} > 8$ GeV, there is no evident modification in PbPb compared to pp. Excess yields do not exhibit significant dependence on collision energies; particle yields at low- p_T^{trk} are consistently larger at 5.02 TeV than at 2.76 TeV, but within the systematic uncertainties of the two measurements.

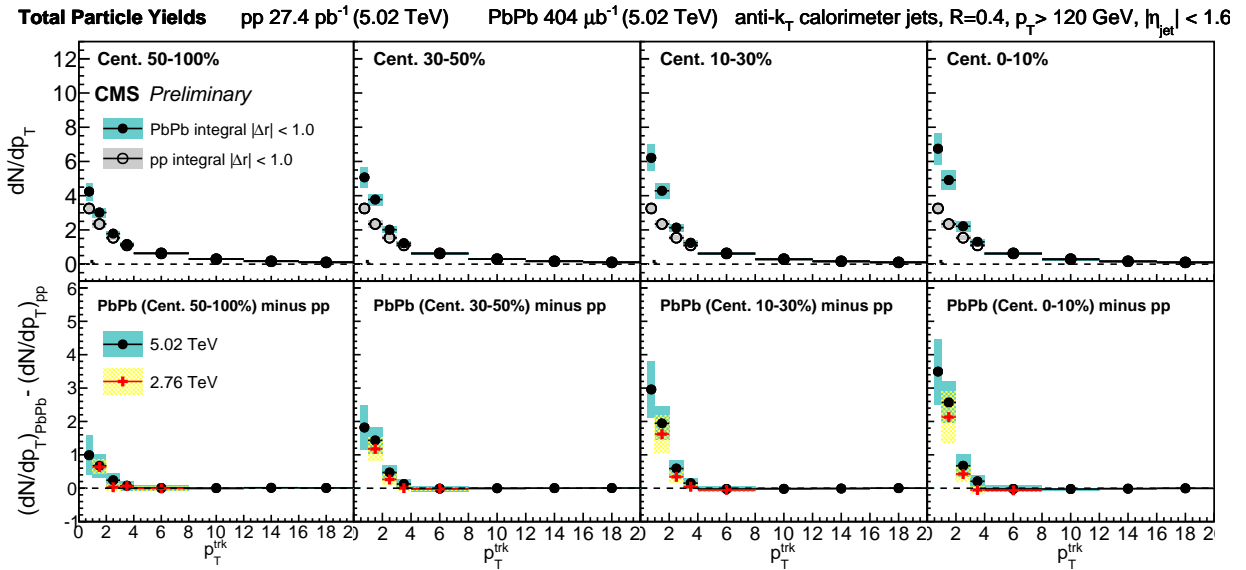


Figure 54. Top row: integrated yields of charged particle yields correlated to jets with $p_T > 120$ GeV as a function of p_T^{trk} bins for PbPb data, compared to pp reference. Bottom row: integrated excess yield, PbPb minus pp. New measurements of excess yields at 5.02 TeV are compared to those measured at 2.76 TeV.

1294 **10.2 Dijet correlation results at 2.76 TeV**

1295 In the studies of charged-particle yields correlated to an inclusive sample of jets with $p_T > 120$
1296 GeV presented above, jet quenching is evident in the redistribution of p_T^{trk} from harder to softer
1297 particles, and particularly in the observed centrality-dependent excess of low- p_T^{trk} particle yields. Jet
1298 quenching effects may be further probed by considering charged-particle yields correlated to each
1299 jet axis in dijet events. Requiring events with two back-to-back jets (leading jet $p_{T,1} > 120$ GeV,
1300 subleading jet $p_{T,2} > 50$ GeV, $\Delta\phi_{1,2} > \frac{5\pi}{6}$), we construct separate correlations to the leading and
1301 the subleading jet axes. In pp data, most dijets are balanced while in central PbPb a greater fraction
1302 of dijet pairs are unbalanced (as discussed in Sec. 8.4), suggesting that central PbPb data contains
1303 a significant fraction of dijet pairs in which the highest- and second-highest- p_T hard-scattering
1304 products had similar transverse momenta, but in which one jet experienced a greater path-length
1305 through the medium and correspondingly greater quenching. This is expected to correspond to a
1306 “surface-bias” toward leading jets with very short path-lengths through the medium, that might
1307 be expected to cause minimal quenching in the leading jet sample. It is therefore interesting to
1308 separately compare charged-particle distributions with respect to the leading and subleading jet
1309 axes in PbPb and pp data to look for evidence of path-length dependence in jet quenching.

1310 Figures 55 and 56 show these correlation patterns in $\Delta\eta$ and $\Delta\phi$, respectively, for the
1311 $1 < p_T^{\text{trk}}$ GeV range in which the greatest quenching was evident in the 2.76 TeV inclusive jet
1312 studies. As expected, quenching effects are greater for subleading than leading jets, as evident in
1313 larger excesses of soft particles in subleading jet correlations (while retaining the same centrality
1314 trends and gaussian-like distributions observed for the inclusive jet sample). However, leading jets
1315 exhibit evidence of quenching as well, showing similar soft-particle excesses to those observed in
1316 the inclusive sample. To quantitatively compare subleading and leading jet modifications to those
1317 in the inclusive jet sample, Fig. 57 shows integrated particle yields for all three jet samples at 2.76
1318 TeV. Here it is clear that leading jets show similar PbPb–pp modifications to those observed in the
1319 inclusive sample, with approximately 2 excess particles in PbPb compared to pp data at lowest- p_T^{trk} ,
1320 while the subleading jet sample shows as many as 4 excess particles in PbPb compared to pp data
1321 at lowest- p_T^{trk} .

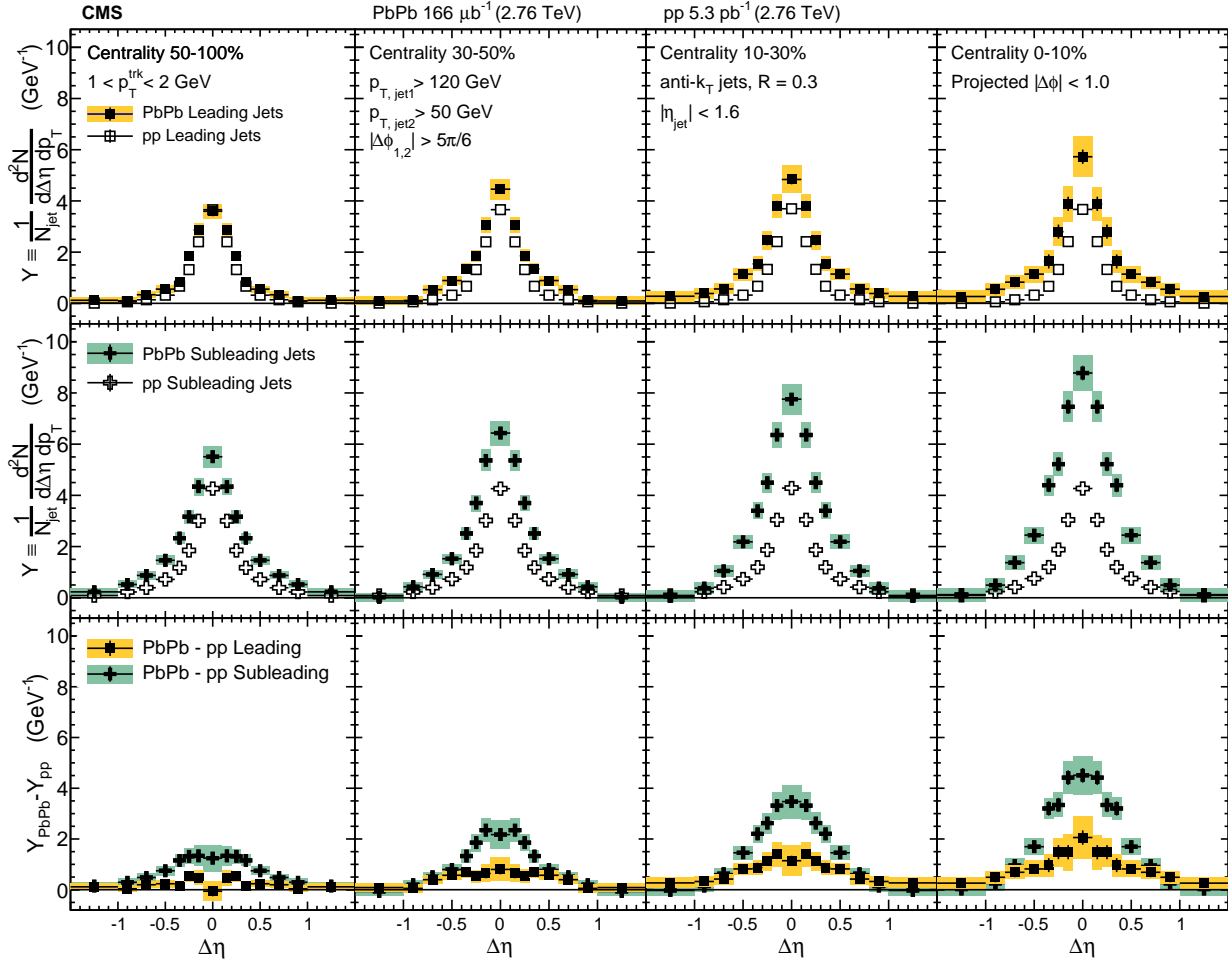


Figure 55. The top panels show the $\Delta\eta$ distributions (projected over $|\Delta\phi| < 1$) of charged-particle background-subtracted yields correlated to PbPb and pp leading jets with $p_{T,\text{jet}1} > 120$ GeV. The middle panels show the same distributions for subleading jets with $p_{T,\text{jet}2} > 50$ GeV, and the bottom panels show the difference PbPb minus pp for both leading and subleading jets. The total systematic uncertainties are shown as shaded boxes, and statistical uncertainties are shown as vertical bars (often smaller than the symbol size).

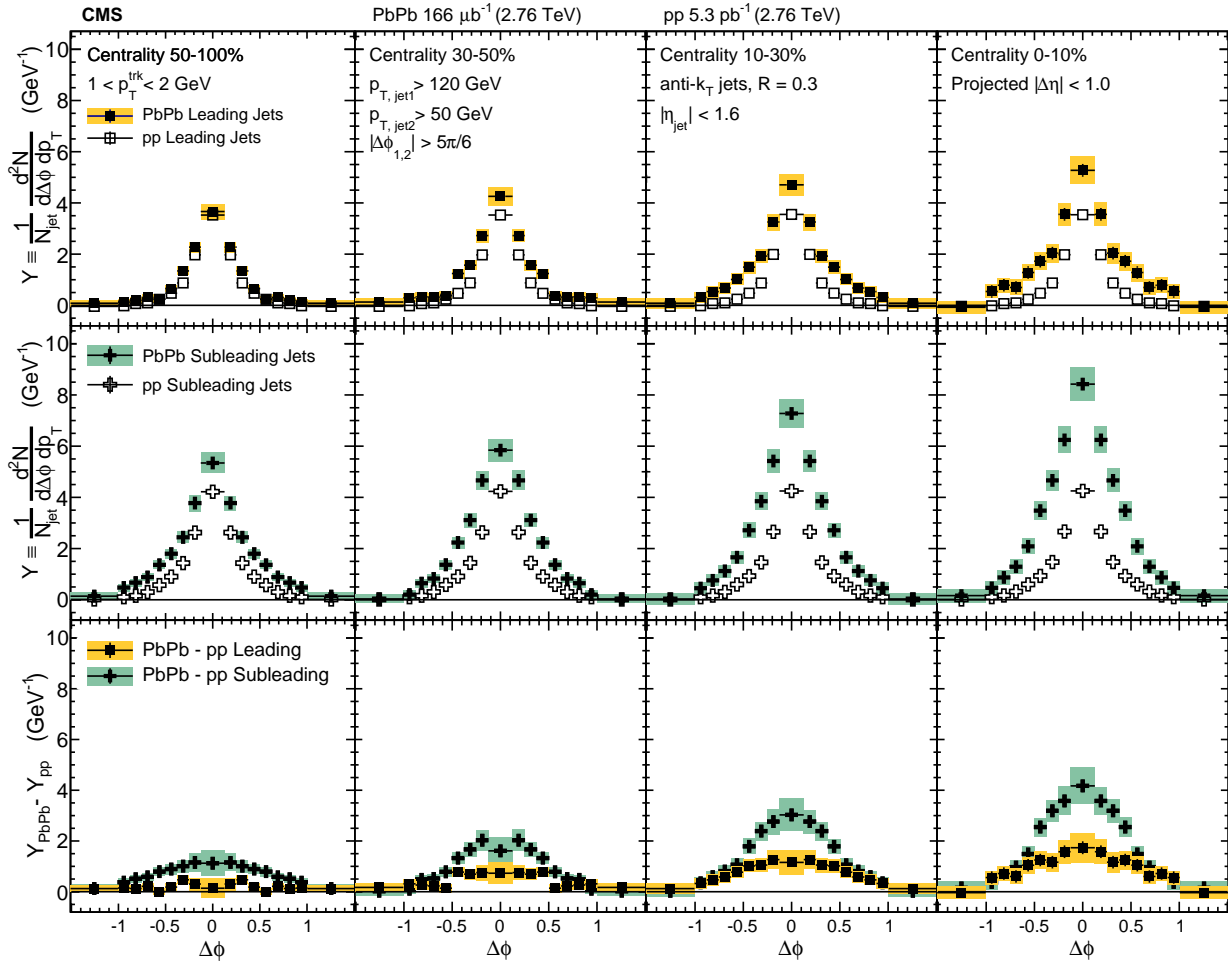


Figure 56. The top panels show the $\Delta\phi$ distributions (projected over $|\Delta\eta| < 1$) of charged-particle background-subtracted yields correlated to PbPb and pp leading jets with $p_{T,\text{jet}1} > 120$ GeV. The middle panels show the same distributions for subleading jets with $p_{T,\text{jet}2} > 50$ GeV, and the bottom panels show the difference PbPb minus pp for both leading and subleading jets. The total systematic uncertainties are shown as shaded boxes, and statistical uncertainties are shown as vertical bars (often smaller than the symbol size).

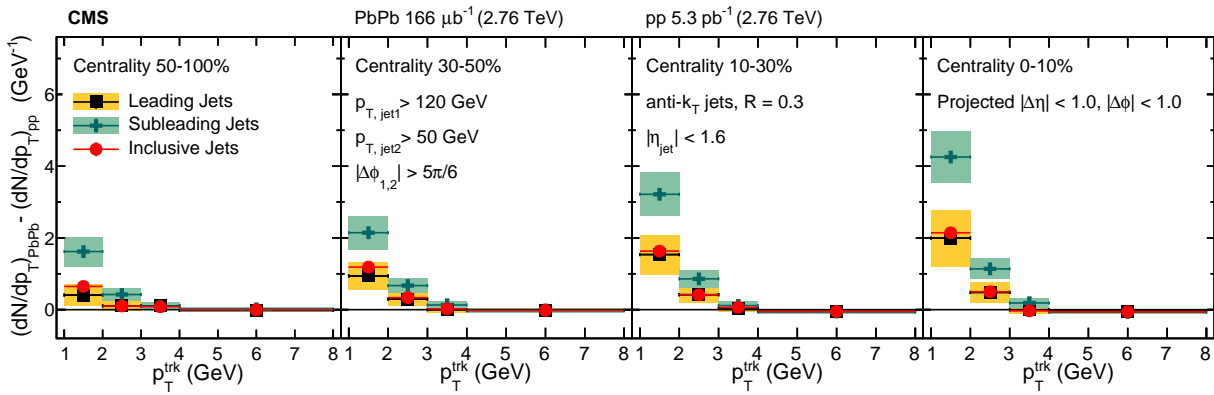


Figure 57. Total excess correlated yield observed in the PbPb data with respect to the reference measured in pp collisions, shown as a function of track p_T in four different centrality intervals (0–10%, 10–30%, 30–50%, 50–100%) for both leading jets with $p_{T,\text{jet}1} > 120$ GeV and subleading jets with $p_{T,\text{jet}2} > 50$ GeV. The total systematic uncertainties are shown as shaded boxes, and statistical uncertainties are shown as vertical bars (often smaller than the symbol size).

1322 In addition to characterizing the magnitude of jet quenching products (via the centrality-
1323 dependent excess of low- p_T^{trk} tracks greatest in correlations to subleading jets but also present in
1324 leading jet correlations), modifications to charged-particle correlated yields may also be character-
1325 ized by their widths. These studies are relevant to look for the presence and extent of jet peak
1326 broadening due to medium interactions, and can be used to distinguish between different models
1327 for jet-medium interaction and medium-modified jet radiation. In order to characterize correlation
1328 widths, correlations are fit to double-gaussian functions (all $\Delta\eta$ fits are shown in Appendix D for
1329 illustration), and the width (σ) of these fits is obtained as the range in $|\Delta\eta|$ or $|\Delta\phi|$ containing
1330 67% of the total yield under the fit curve. To obtain systematic uncertainties on these fits, points
1331 are varied up and down by their systematic uncertainties, and widths are re-calculated from these
1332 varied distributions.

1333 Figures 58 and 59 show correlation widths in $\Delta\eta$ and $\Delta\phi$ for leading jets in PbPb and
1334 pp data at 2.76 TeV. At low- p_T^{trk} there is a significant broadening evident in central PbPb data
1335 when compared to pp data, with this broadening decreasing in more peripheral collisions and with
1336 increasing p_T^{trk} (with similar trends to those exhibited by correlated yield magnitudes). Widths
1337 and width modifications are similar in $\Delta\eta$ and $\Delta\phi$, but slightly broader in $\Delta\phi$ for PbPb data.
1338 These leading jet correlation widths and width modifications may also be compared to subleading
1339 jet correlation widths and width modifications, shown in Figs. 60 and 61. In peripheral PbPb
1340 data subleading and leading correlation widths are similar, but subleading jet PbPb correlation
1341 widths exhibiting less centrality dependence than leading jet correlation widths so that leading jet
1342 correlations in central PbPb data are slightly broader than subleading jet correlations (but
1343 not significantly so, when taking into account the systematic uncertainties on both measurements).
1344 Subleading jet peaks in pp data are, however, significantly broader than leading jet peaks in pp
1345 data—as is to be expected since the kinematic selection defining subleading jet as that with lower- p_T ,
1346 also implies that subleading jets will on average have softer fragmentation than leading jets. Since
1347 subleading pp jets are broader than leading pp jets while subleading and leading jets have similar
1348 widths in PbPb, the jet peak broadening quantified as the PbPb–pp difference in widths is greater
1349 for leading jets than for subleading jets.

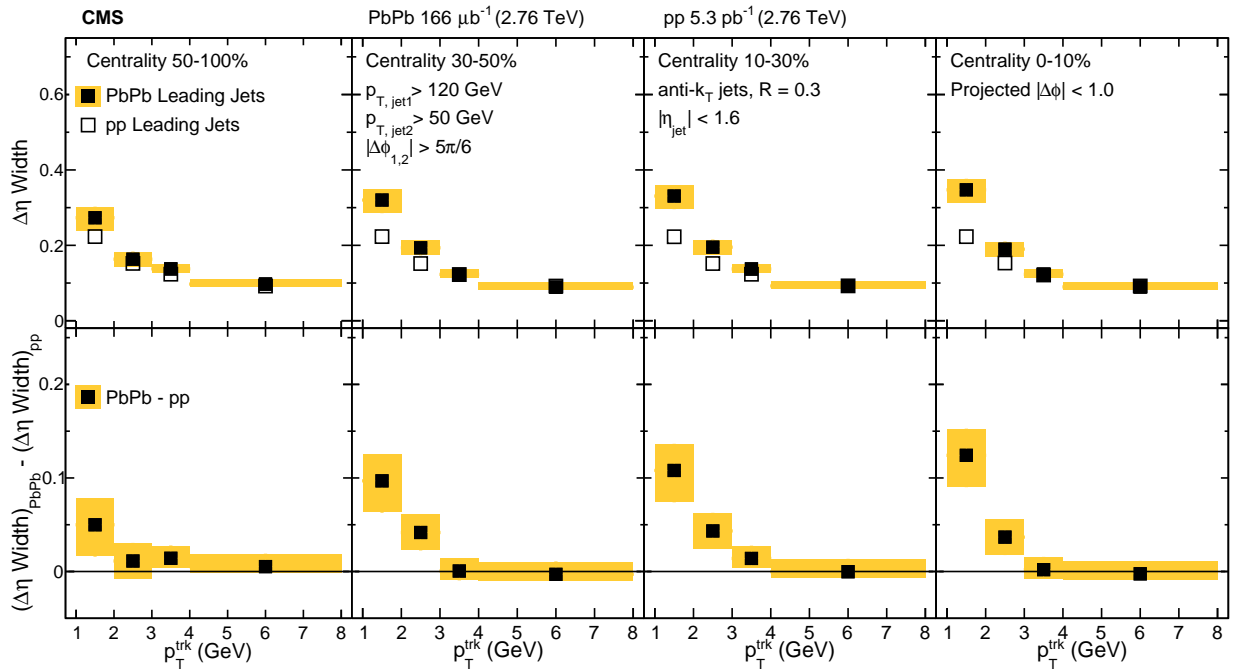


Figure 58. Comparison of the widths in PbPb and pp of the $\Delta\eta$ charged-particle distributions correlated to leading jets with $p_{\text{T},\text{jet}1} > 120 \text{ GeV}$, as a function of $p_{\text{T}}^{\text{trk}}$. The bottom row shows the difference of the widths in PbPb and pp data. The shaded band corresponds to systematic uncertainty, and statistical uncertainties are smaller than symbol size.

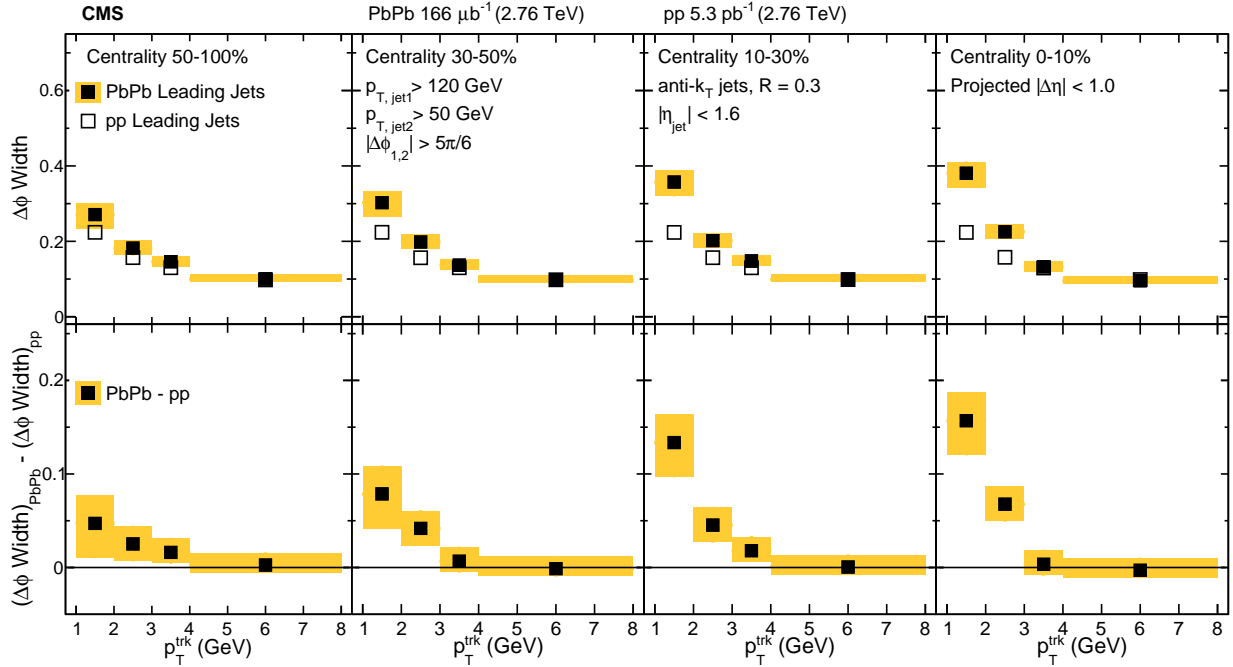


Figure 59. Comparison of the widths in PbPb and pp of the $\Delta\phi$ charged-particle distributions correlated to leading jets with $p_{T,\text{jet}1} > 120$ GeV, as a function of p_T^{trk} . The bottom row shows the difference of the widths in PbPb and pp data. The shaded band corresponds to systematic uncertainty, and statistical uncertainties are smaller than symbol size.

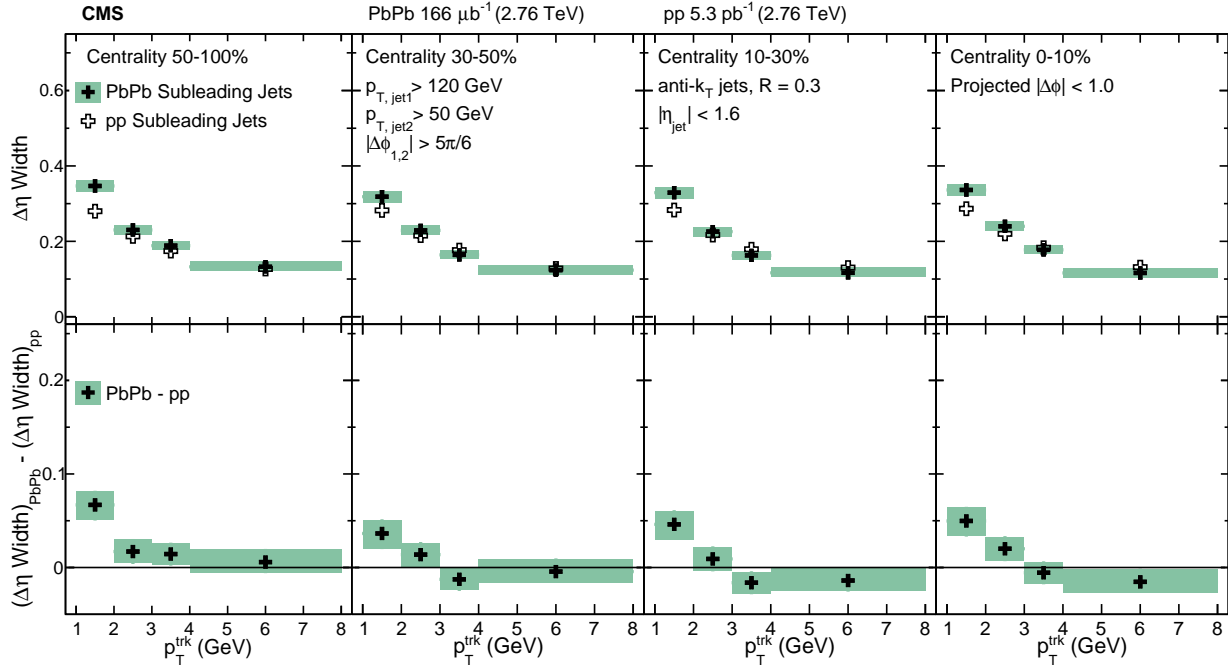


Figure 60. Comparison of the widths in PbPb and pp of the $\Delta\eta$ charged-particle distributions correlated to leading jets with $p_{T,\text{jet}2} > 50 \text{ GeV}$, as a function of p_T^{trk} . The bottom row shows the difference of the widths in PbPb and pp data. The shaded band corresponds to systematic uncertainty, and statistical uncertainties are smaller than symbol size.

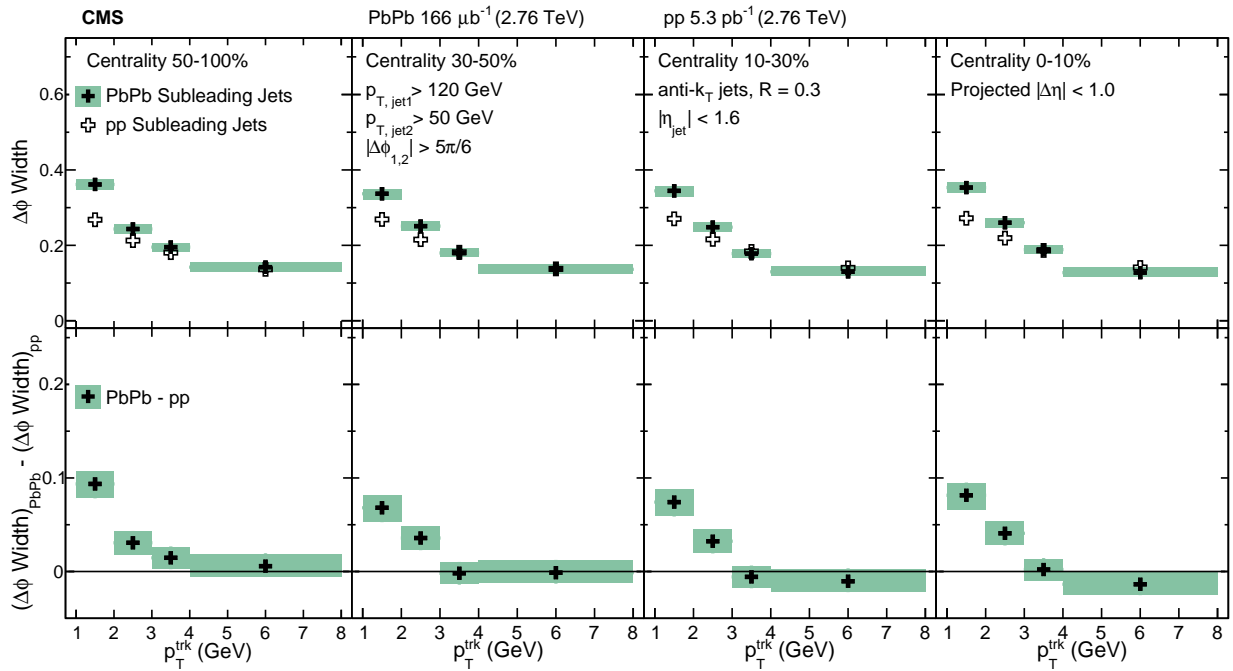


Figure 61. Comparison of the widths in PbPb and pp of the $\Delta\phi$ charged-particle distributions correlated to leading jets with $p_{T,\text{jet}2} > 50$ GeV, as a function of $p_{T,\text{track}}$. The bottom row shows the difference of the widths in PbPb and pp data. The shaded band corresponds to systematic uncertainty, and statistical uncertainties are smaller than symbol size.

1350 **10.3 Jet shapes at 2.76 TeV and 5.02 TeV**

1351 A common observable to characterize and compare the widths of jet peaks is the jet shape $\rho_{\Delta r}$,
 1352 measuring the fraction of total jet transverse momentum as a function of distance Δr from the jet
 1353 axis. As discussed in Sec. 4, previous CMS measurements of jet shape [31] have gained particular
 1354 attention from the theoretical community in efforts to constrain models of jet energy loss. Jet shape
 1355 measurements to large angles ($\Delta r = 1$, compared to previous measurements to only $\Delta r = 0.3$) may
 1356 be obtained from correlation studies, extending measurements to the full range of the jet peak
 1357 and offering the capability of distinguishing between theoretical predictions based on earlier, more
 1358 narrow, measurements.

1359 In the correlation technique, jet shapes are obtained by weighting correlations by p_T^{trk} , and
 1360 integrating the resulting (background-subtracted) 2D jet-peak momentum distributions in annuli
 1361 with radial width $\Delta r = 0.05$, where each has an inner radius of $r_a = \Delta r - \delta r/2$ and an outer radius
 1362 of $r_b = \Delta r + \delta r/2$. For this measurement, an inclusive high- p_T^{trk} bin is included to capture particles
 1363 with $20 < p_T^{\text{trk}} < 300$ GeV. The resulting transverse momentum profile of the jet is defined as:

$$P(\Delta r) = \frac{1}{\delta r} \frac{1}{N_{\text{jets}}} \sum_{\text{jets}} \sum_{\text{tracks} \in (r_a, r_b)} p_T^{\text{trk}} \quad (27)$$

1364 This profile is then normalized to unity within $\Delta r = 1$ to produce the jet shape $\rho(\Delta r)$:

$$\rho(\Delta r) = \frac{1}{\delta r} \frac{\sum_{\text{jets}} \sum_{\text{tracks} \in (r_a, r_b)} p_T^{\text{trk}}}{\sum_{\text{jets}} \sum_{\text{tracks}} p_T^{\text{trk}}} \quad (28)$$

1365 The top row of Fig. 62 presents the inclusive jet transverse momentum profile $P(\Delta r)$ in pp
 1366 and PbPb data at 5.02 TeV, while the middle row shows the jet shape $\rho(\Delta r)$, normalized to unity
 1367 within $\Delta r = 1$. Here again redistribution of energy from small to large angles from the jet cone is
 1368 evident in PbPb relative to pp reference, as seen in the dipping then rising trend in the jet shape
 1369 ratio $\rho(\Delta r)_{\text{PbPb}}/\rho(\Delta r)_{\text{pp}}$ presented in the bottom row.

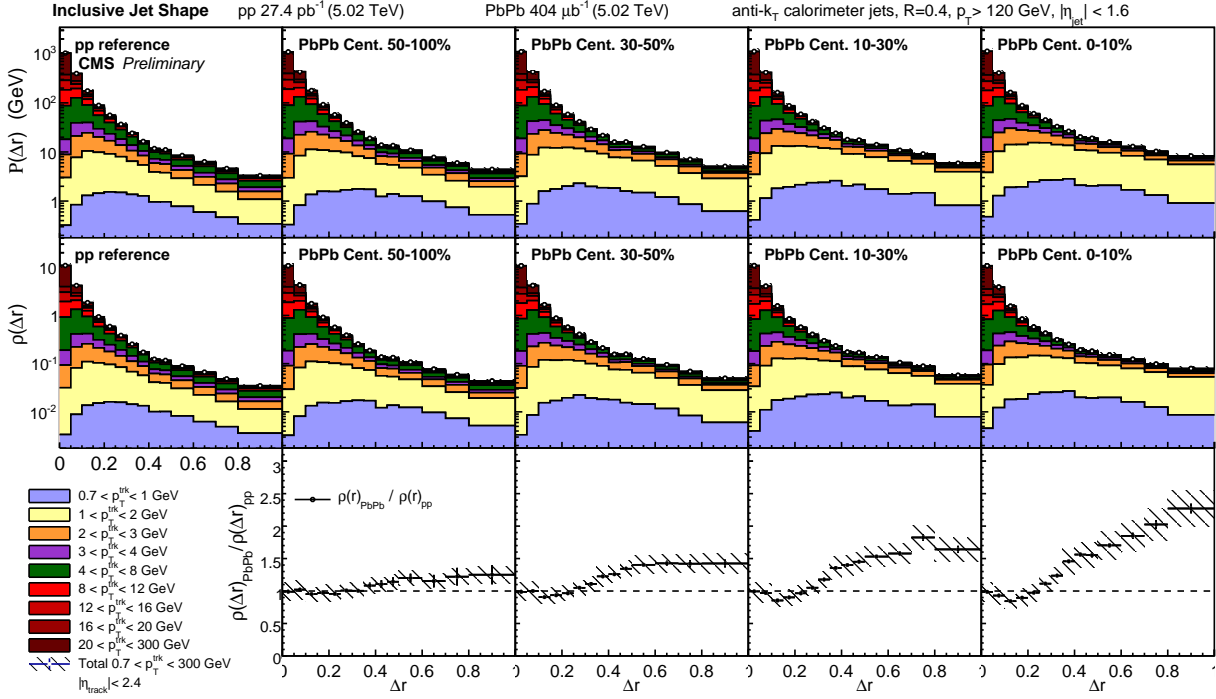


Figure 62. Top row: Transverse momentum profile of inclusive jets $P(\Delta r)$ in pp and PbPb data at 5.02 TeV, shown differentially in p_T^{trk} . Middle row: jet shapes $\rho(\Delta r)$ (normalized to unity over $\Delta r < 1$) in PbPb and pp. Bottom row: jet shape ratio $\rho(\Delta r)_{\text{PbPb}} / \rho(\Delta r)_{\text{pp}}$. Hatched lines on p_T^{trk} -inclusive points show total systematic uncertainties.

In addition to studies of inclusive jet shapes, it is also interesting to consider the jet shapes and jet shape modifications of leading and subleading jets in dijet events. These studies are carried out with the same selection of 2.76 TeV dijet events used for the correlation studies presented in 10.2. In this case, for consistency with a previous CMS study measured the jet shape $\rho(\Delta r)$ within the jet cone radius $\Delta r = 0.3$ [31] at 2.76 TeV, these leading and subleading jet shape measurements at 2.76 TeV are normalized to integrate to unity with in the radius $\Delta r < 0.3$. In Fig. 63, the leading jet shape measured with this correlation technique is compared to the published CMS reference and extend this measurement to $\Delta r = 1$, noting that the leading jet shape is consistent within uncertainties with the previous measurement for an inclusive jet selection of all jets with $p_T > 100$ GeV. A new measurement of subleading jet shape in Fig. 64 is then presented. As noted in the correlation width measurements discussed in Sec. 10.2, subleading jets in pp data are broader than leading jets in pp data. Therefore, although the PbPb-to-pp *modifications* are similar for leading and subleading jets, the more steeply falling pp leading jet shape results in a greater *relative*

1383 modification shown in the jet shape ratio $\rho_{\text{PbPb}}(\Delta r)/\rho_{\text{pp}}(\Delta r)$ for leading than for subleading jets.
 1384 Similarly, when comparing jet shape measurements at 2.76 TeV to those at 5.02 TeV, it is relevant
 1385 to note that the pp reference is broader at 5.02 TeV than at 2.76 TeV, likely due to the greater
 1386 fraction of gluon versus quark jets that pass the kinematic selections of the analysis at the higher
 1387 center-of-mass energy.

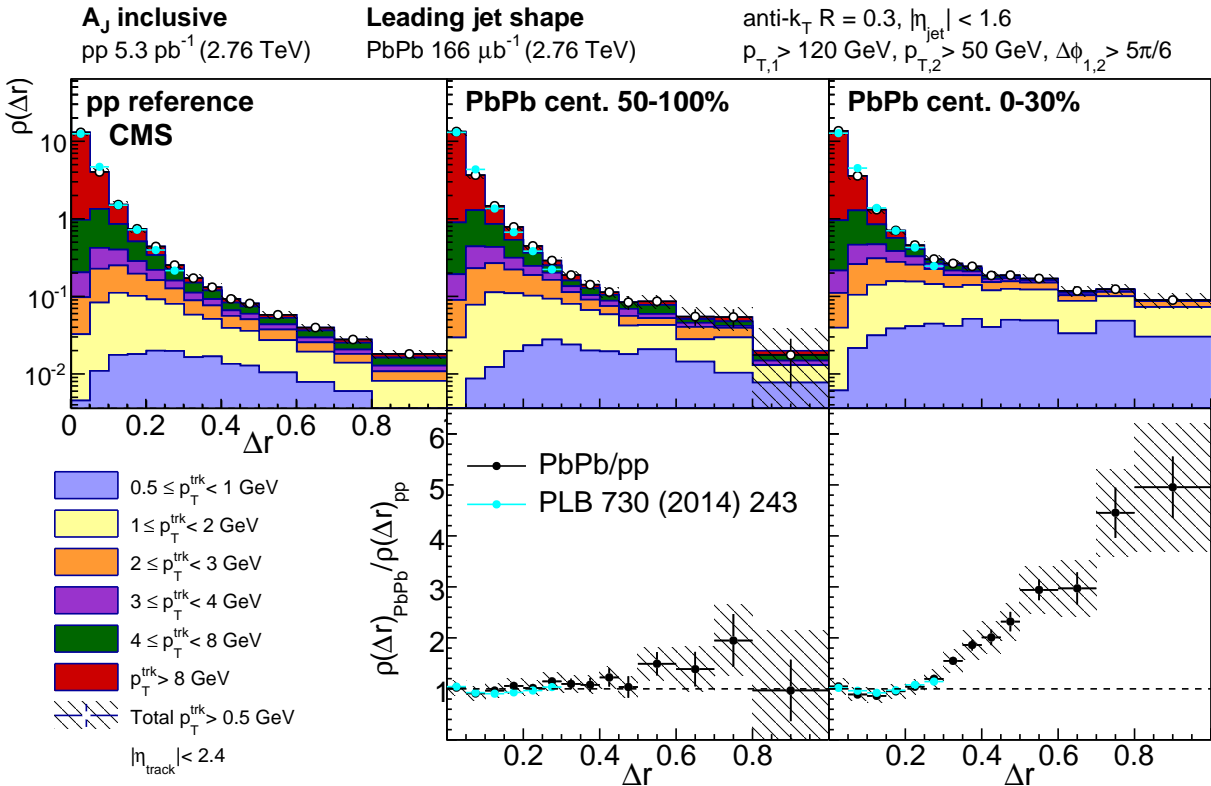


Figure 63. Top row: leading jet shape $\rho(\Delta r)$ for pp reference and central and peripheral PbPb data, shown for all tracks with $p_{T}^{\text{trk}} > 0.5$ GeV and decomposed by track transverse momentum. Shapes are normalized to unity over the region $r < 0.3$ for consistency with the published reference shown (Ref. [31]). Bottom row: leading jet shape ratio $\rho(\Delta r)_{\text{PbPb}}/\rho(\Delta r)_{\text{pp}}$, again with published reference.

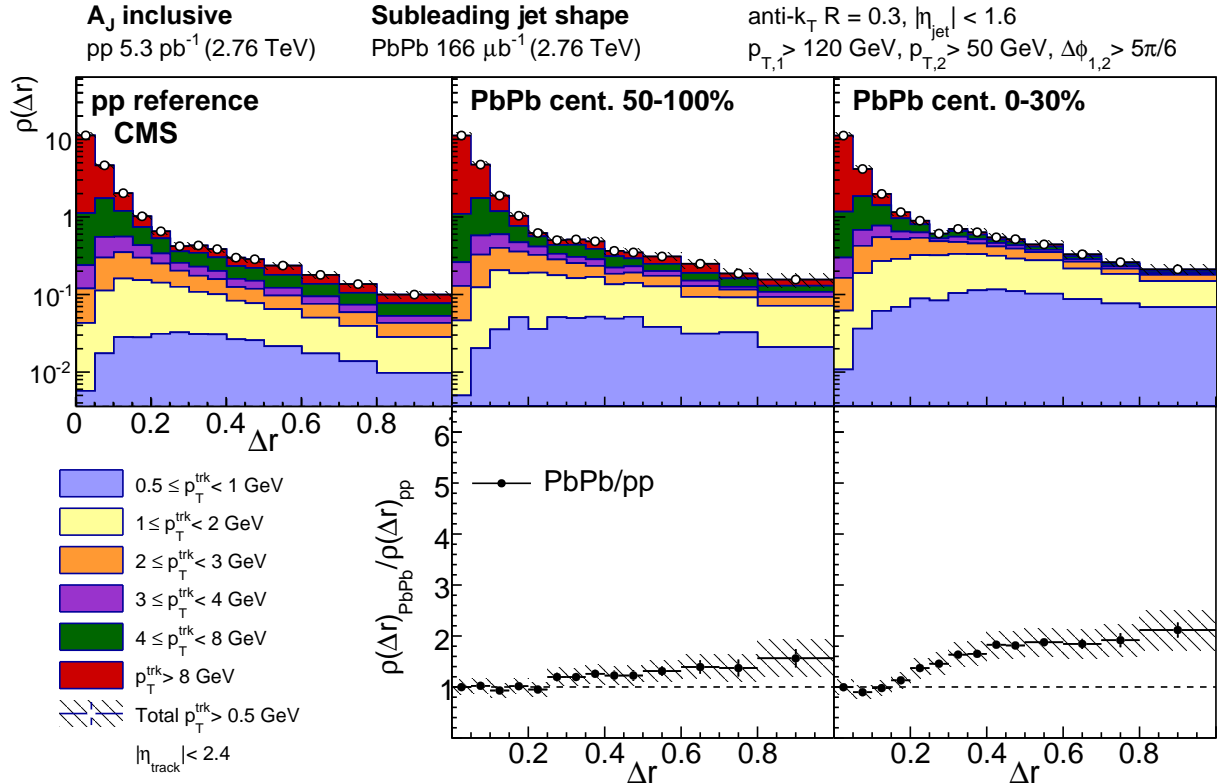


Figure 64. Top row: subleading jet shape $\rho(\Delta r)$ for pp reference and central and peripheral PbPb data, shown for all tracks with $p_T > 0.5$ GeV and decomposed by track transverse momentum, normalized to unity over the region $\Delta r < 0.3$. Bottom row: subleading jet shape ratio $\rho(\Delta r)_{\text{PbPb}} / \rho(\Delta r)_{\text{pp}}$.

1388 **10.4 Decomposition of hemisphere momentum balance in dijet events at 2.76 TeV**

1389 The dijet results at 2.76 TeV presented in this analysis are complimented by other CMS measure-
1390 ments conducted on the same data using the “missing- p_T ” hemisphere momentum balance method
1391 presented in Ref. [54] and discussed in Secs. 3 and 4. In this analysis, a “dijet” axis is constructed
1392 by averaging the leading jet and subleading jet axes (these are separated by $\Delta\phi_{1,2} = \pi$ on average,
1393 but are not necessarily parallel in each event due to 3-jet events) to construct a dijet axis, dividing
1394 the event into leading and subleading hemispheres with respect to this axis, and comparing the
1395 hemisphere-wide distributions of p_T^{trk} (projected, in this case, onto the combined dijet axis) to ob-
1396 tain the subleading-to-leading balancing distribution as a function of distance from the dijet axis
1397 Δr . The jet track correlation technique may be used to obtain this same measurement (comparing
1398 subleading-to-leading distributions on average rather than event-by-event, and making use of the
1399 fact that the subleading and leading jet axes are *on average* perfectly back-to-back). When this
1400 cross-check is performed *without background subtraction*, the two techniques yield consistent results,
1401 despite methodological differences and differences in jet- η cuts. This hemisphere-wide missing- p_T
1402 technique is also used to extract differences in total particle yields between the leading and sublead-
1403 ing hemispheres, and shows an average excess of 4–5 particles with p_T^{trk} in the subleading hemisphere
1404 compared to the leading hemisphere [54]. In the dijet correlation studies presented in this analysis
1405 *with background subtraction*, however, only approximately 2 additional particles were found cor-
1406 related to the subleading jet peak compared to the leading jet peak, as shown in Sec. 10.2. This
1407 apparent difference motivates a detailed examination and decomposition of the distribution of p_T^{trk}
1408 in dijet events in order to consider contributions to the hemisphere-wide momentum balance from
1409 both the leading and subleading jet peaks, and from the long-range correlated underlying event.

1410 For this investigation, the dijet samples of 2.76 TeV PbPb and pp data are each divided
1411 based on asymmetry parameter A_J to further illuminate quenching effects and to decompose the
1412 contributions to the hemisphere p_T^{trk} balance studied in Ref. [54]: a balanced sample with $A_J < 0.22$,
1413 and an “unbalanced” sample with $A_J > 0.22$. Transverse momentum distributions for each sample
1414 are constructed in $\Delta\eta - \Delta\phi$ for each sample, and are corrected for pair-acceptance effects. Like all
1415 particle density and p_T^{trk} correlations studied in this analysis, these show jet peaks on an underlying
1416 event that shows significant $\Delta\phi$ correlations but is flat in $\Delta\eta$. Correlations are therefore projected

1417 into $\Delta\phi$ for further study in order to preserve this underlying event structure. Studies will begin
1418 by considering the hemisphere-wide “missing- p_T ” distribution as a function of $\Delta\phi$, and will then
1419 decompose this distribution into jet peak and underlying event contributions, and finally consider
1420 the relative contributions from jet peaks and from the underlying event to the overall hemisphere
1421 p_T^{trk} balance for balanced and unbalanced dijets.

1422 Figures 65 and 66 present the hemisphere-wide balancing distribution of transverse momen-
1423 tum around the subleading versus the leading jet for balanced and unbalanced dijets respectively.
1424 For both selections, a wide excess of soft particles in the subleading versus leading hemisphere in
1425 central PbPb collisions relative to pp reference is evident, reflecting the greater quenching of the
1426 subleading jet. In the unbalanced selection, as required by momentum conservation, the signal is
1427 enhanced in both pp and PbPb data: in pp a large excess of particles with $p_T > 3$ GeV long-range
1428 is present on the subleading side, compensating for the lower momentum of the highest- p_T particles
1429 in the jet itself. In peripheral PbPb data the distribution is quite similar to pp reference, while
1430 in central PbPb data this balancing distribution consists mostly of soft particles $p_T < 3$ GeV,
1431 consistent with the findings of a previous CMS study [54]. To better demonstrate these medium
1432 modifications, the difference in yield between PbPb and pp collisions is shown in the bottom panels
1433 of Fig. 65 and Fig. 66.

1434 To better understand the redistribution of transverse momentum within the QGP, the
1435 distributions are then separated into three components as discussed above: the gaussian-like peaks
1436 about the leading and subleading jet axes, plus a component accounting for overall subleading-
1437 to-leading asymmetry in the $\Delta\phi$ -correlated long-range underlying event (measured in the region
1438 $1.5 < |\Delta\eta| < 2.5$). In Fig. 67 and Fig. 68, the jet peak components are shown for balanced and
1439 unbalanced jets respectively, presenting subleading results positive and leading results negative (in
1440 line with the hemisphere difference measurements in Fig. 66 and Fig. 65). Jet peak distributions
1441 after decomposition are projected over the full range $|\Delta\eta| < 2.5$, again for consistency with the
1442 hemisphere difference measurements. The top row of each panel first shows the overall distribution
1443 of momentum carried by particles with $p_T < 8$ GeV on about the jet peak. The middle two panels
1444 then assess modifications to the subleading and leading jets, respectively. Here there is evidence
1445 of quenching to both the subleading and the leading jet in central PbPb collisions relative to pp
1446 reference, with an excess of low- p_T^{trk} particles correlated to the jet axis in both the balanced and

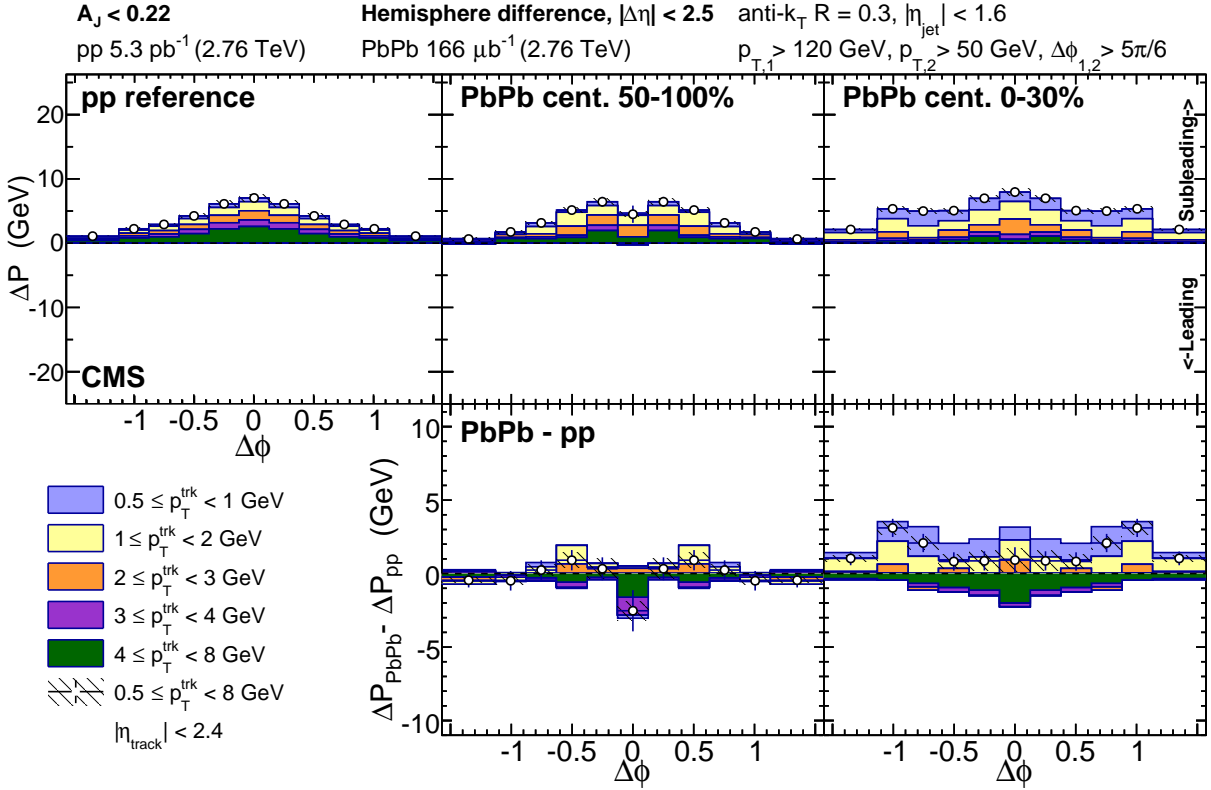


Figure 65. Top row: total hemisphere distribution in $\Delta\phi$ of excess transverse momentum about the subleading relative to the leading jet for balanced dijets with $A_J < 0.22$, shown differentially by track transverse momentum for pp reference, peripheral PbPb, and central PbPb data. Bottom row: PbPb–pp difference in these $\Delta\phi$ momentum distributions.

1447 unbalanced dijet selections, as observed in the charged particle density studies presented in Sec. 10.2.
 1448 In unbalanced dijets this enhancement of soft- p_T^{trk} particles turns into a depletion at higher- p_T^{trk} , and
 1449 is greater on the subleading than the leading side. To compare between hemispheres and assess the
 1450 jet peak contribution to the overall hemisphere momentum balance, the double difference PbPb–pp,
 1451 subleading–leading is presented in the bottom panel. Here it is evident that the low- p_T^{trk} excess
 1452 in central PbPb collisions is larger on the subleading than the leading side of the dijet system,
 1453 but larger subleading-to-leading excess only accounts for only a portion of the total momentum
 1454 redistribution in unbalanced dijet events.

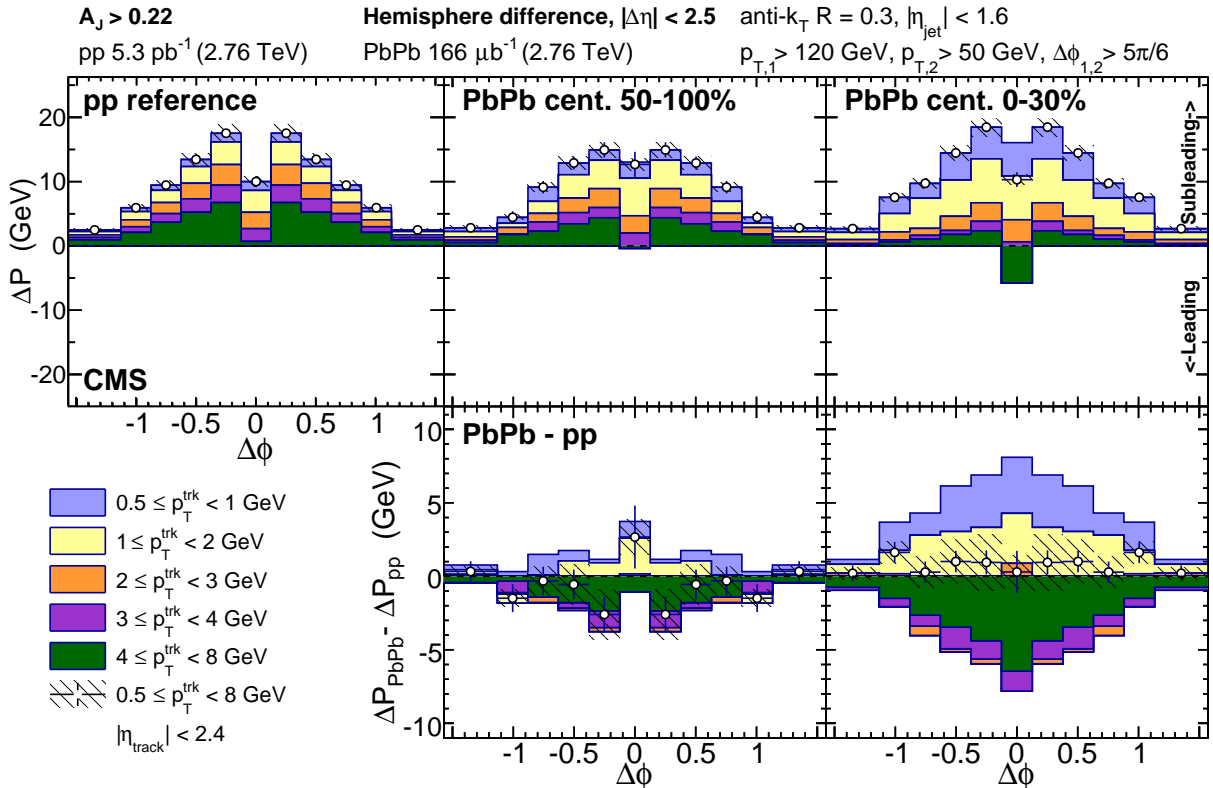


Figure 66. Top row: total hemisphere distribution in $\Delta\phi$ of excess transverse momentum about the subleading relative to the leading jet for balanced dijets with $A_J > 0.22$, shown differentially by track transverse momentum for pp reference, peripheral PbPb, and central PbPb data. Bottom row: PbPb-pp difference in these $\Delta\phi$ momentum distributions.

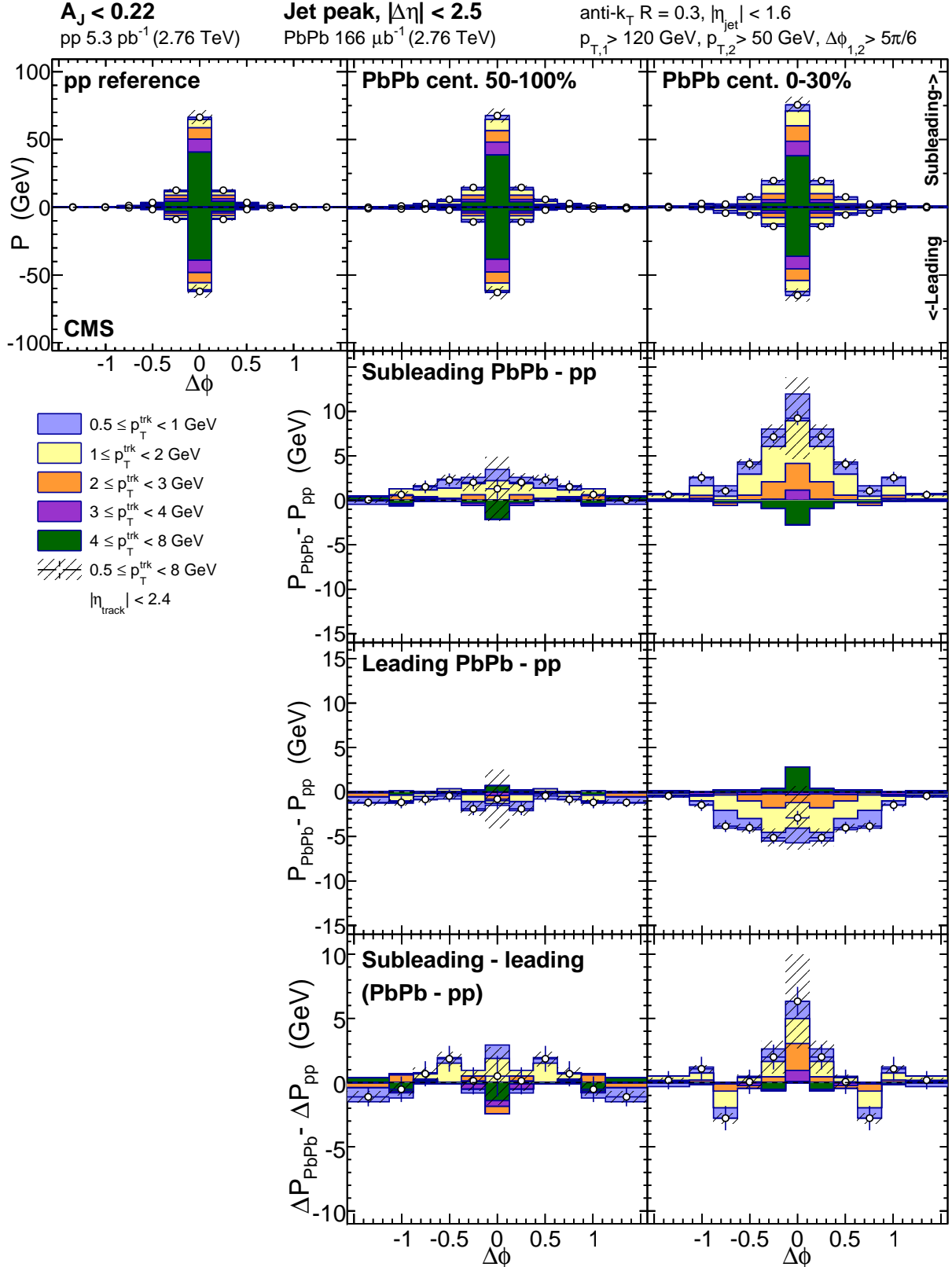


Figure 67. Top row: jet-peak (long-range subtracted) distribution in $\Delta\phi$ of transverse momentum about the subleading (plotted positive) and leading (plotted negative) jets for balanced dijets with $A_J < 0.22$. Middle rows: PbPb–pp momentum distribution differences for subleading and leading jets. Bottom row: PbPb–pp, subleading–leading double difference in these $\Delta\phi$ momentum distributions.

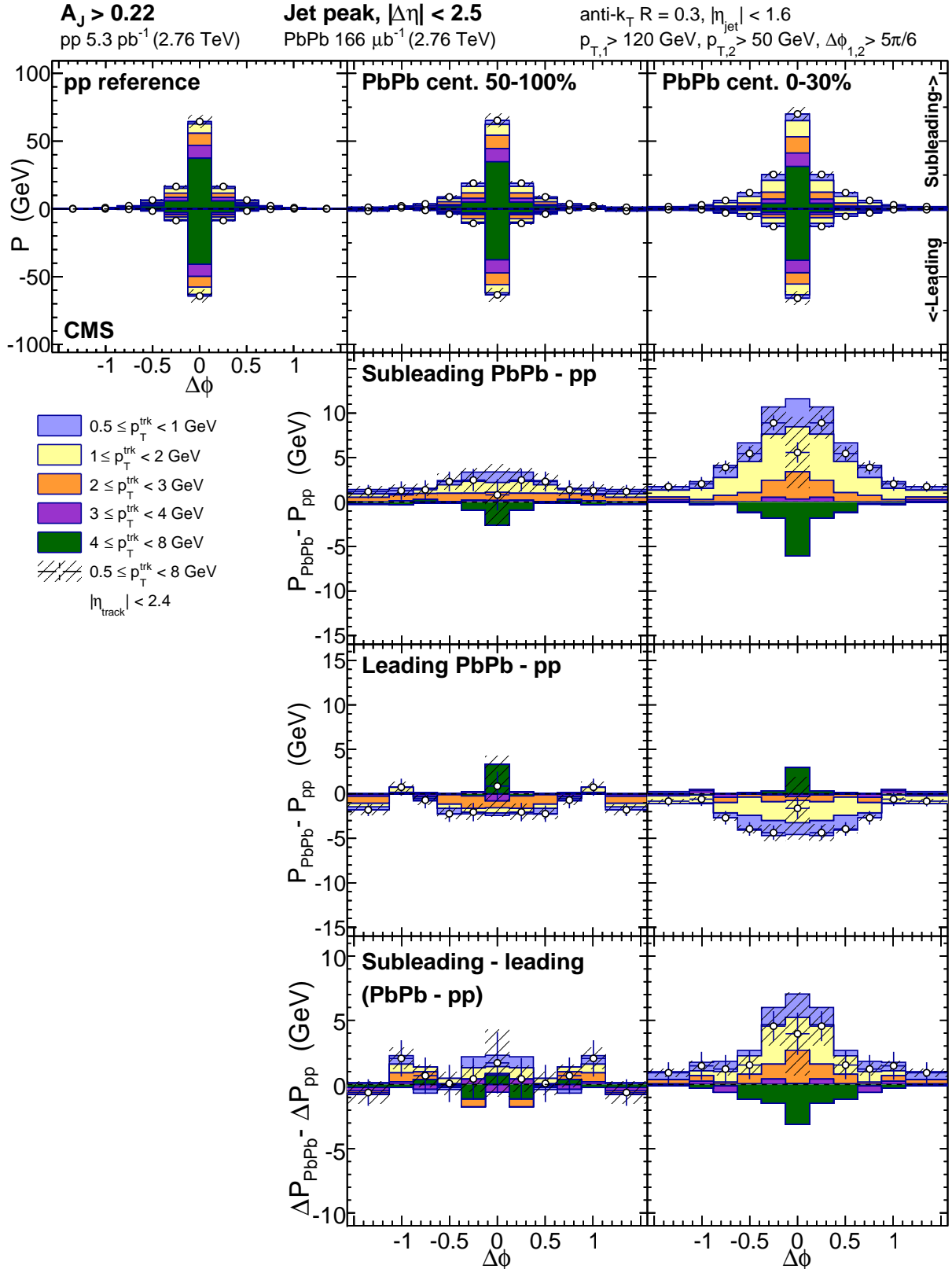


Figure 68. Top row: jet-peak (long-range subtracted) distribution in $\Delta\phi$ of transverse momentum about the subleading (plotted positive) and leading (plotted negative) jets for balanced dijets with $A_J > 0.22$. Middle rows: PbPb-pp momentum distribution differences for subleading and leading jets. Bottom row: PbPb-pp, subleading-leading double difference in these $\Delta\phi$ momentum distributions.

These jet-related studies are complemented by an analysis of the long-range subleading to leading asymmetry, presented in Fig. 69 and Fig. 70 for balanced and unbalanced jets respectively. The long-range correlated background in balanced dijet events is symmetric in pp and peripheral PbPb data, while in central PbPb data there is a small excess of low- p_T^{trk} particles. In unbalanced dijets, however, there is significant asymmetry already in pp reference, with a large correlated excess of particles in all p_T classes less than 8 GeV on the subleading relative to leading side of the underlying event. This asymmetry reflects the presence of other hard-scattering products in the subleading hemisphere dijet event, as required by momentum conservation when selecting asymmetric dijets in vacuum-like collisions. In the presence of the strongly interacting medium; however, this underlying event asymmetry in asymmetric dijet events changes notably. In peripheral PbPb collisions there is already some depletion of momentum carried by high- p_T^{trk} particles, and in central pp collisions subleading-to-leading underlying event excesses with $p_T^{\text{trk}} > 2$ GeV vanish nearly completely. To assess the contribution of this long-range asymmetry to the total hemisphere imbalance, the double difference PbPb–pp, subleading–leading is plotted on the bottom panel as for (and on the same scale as) the double difference shown for the jet peaks. To assess the overall hemisphere momentum balance attributed to this long-range asymmetry, the hemisphere integral ($|\Delta\phi| < \pi/2$ and $|\Delta\eta| < 2.5$) is presented in Fig. 71 for balanced versus unbalanced dijets. For unbalanced dijets, the the overall asymmetry rises with track- p_T pp reference, but falls with track- p_T for central PbPb data.

Finally, to show the relative contributions to overall hemisphere momentum balance from the leading and subleading jet peaks as well as from the long-range underlying event asymmetry, a summary of hemisphere-integrated excess (PbPb–pp) yield for balanced and unbalanced dijets in central PbPb collisions is shown in Fig. 72 and Fig. 73 for central and peripheral collisions respectively. The top panels of Fig. 72 present total PbPb minus pp differences in transverse momentum associated with the subleading jet (plotted positive) and leading jet (plotted negative). Modifications to the distribution of tracks with $p_T < 3$ GeV are evident for both the leading and subleading jet peaks, with a greater enhancement of low- p_T^{trk} particles associated with the subleading jet. These total jet peak modifications in central PbPb collisions are not significantly different in unbalanced versus balanced dijets. The bottom panels of Fig. 72 present these jet-peak modifications together with the long-range modifications evident in Fig. 71 to show the decomposed

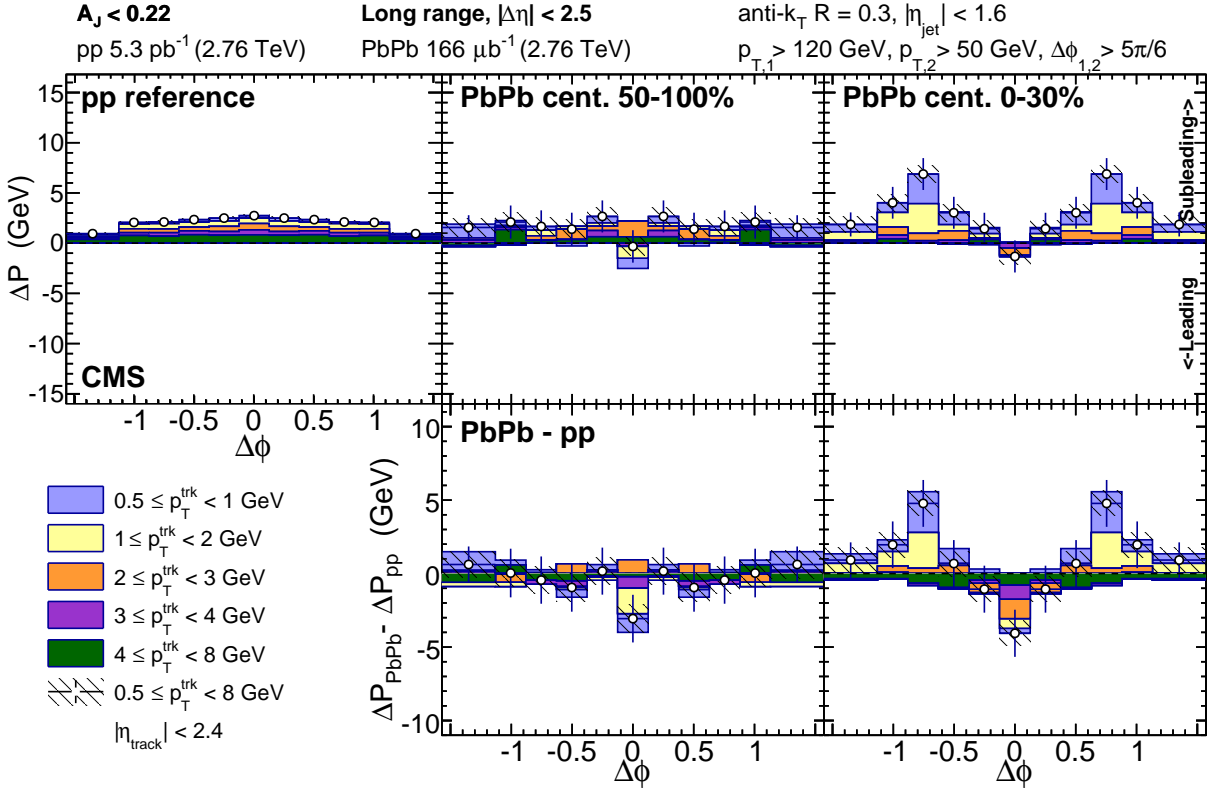


Figure 69. Top row: long-range distribution in $\Delta\phi$ of excess transverse momentum in the subleading relative to leading sides for balanced dijets with $A_J < 0.22$. Bottom row: PbPb–pp difference in these $\Delta\phi$ long-range momentum distributions.

1485 hemisphere-wide differences in associated transverse momentum in each p_T^{trk} range. Unlike the jet
 1486 peak contributions, the long-range PbPb versus modifications differ outside of uncertainties between
 1487 balanced and unbalanced dijets: here the depletion of high- p_T^{trk} particles in unbalanced PbPb versus
 1488 pp dijets corresponds to the reduced contribution from third jets (which are prominently evident
 1489 in the long-range distribution for pp unbalanced dijet events) in central PbPb unbalanced dijet
 1490 events. Figure 73 presents the same hemisphere-integrated PbPb minus pp excess information for
 1491 peripheral collisions for comparison to the central results shown in Fig. 72. Some possible small
 1492 modifications are already evident in this 50-100% centrality range, but these differences between
 1493 peripheral PbPb and pp results are in most cases smaller than systematic uncertainties.

1494 The decomposition of integrated jet peak and long-range correlated p_T^{trk} shown in Fig. 72
 1495 and Fig. 73 clarify the relationship between the jet peak correlation studies presented in this analysis
 1496 and the missing- p_T measurements presented in Ref. [54]: as shown through this detailed decomposi-

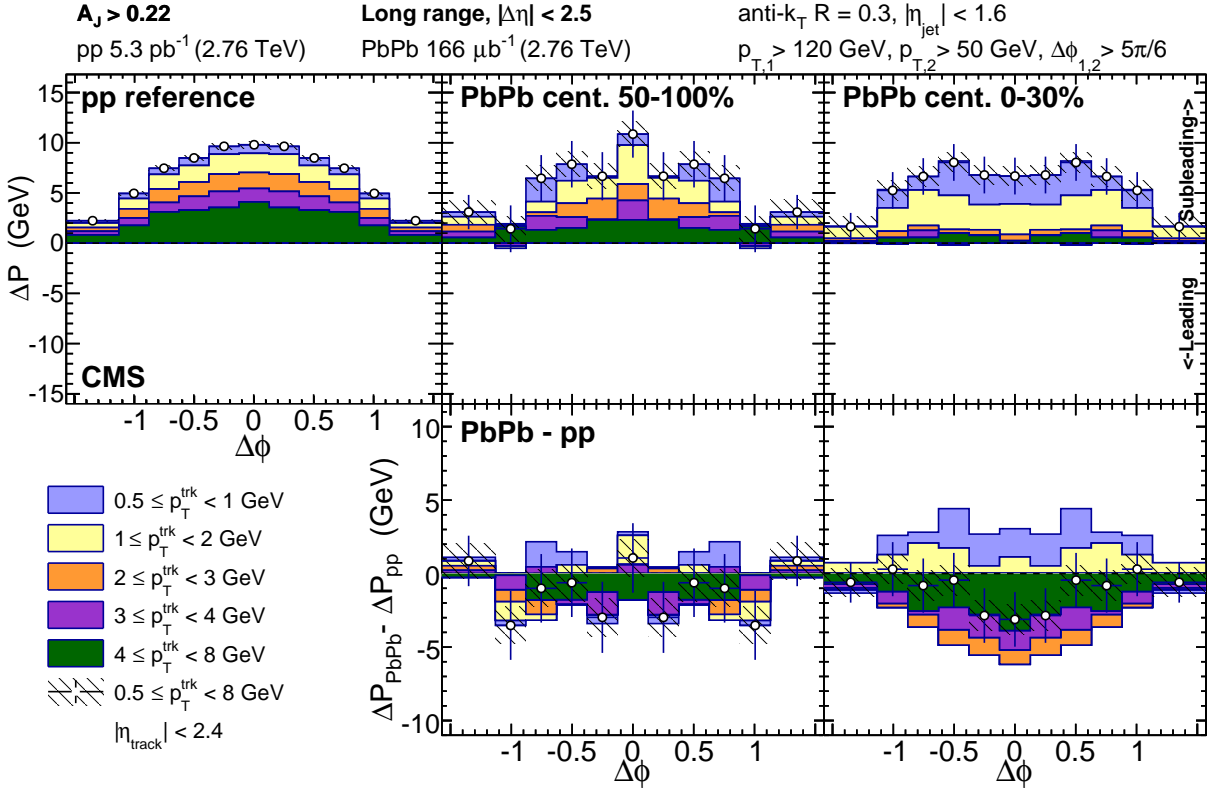


Figure 70. Top row: long-range distribution in $\Delta\phi$ of excess tranverse momentum in the subleading relative to leading sides for balanced dijets with $A_J > 0.22$. Bottom row: PbPb–pp difference in these $\Delta\phi$ long-range momentum distributions.

1497 tion, comparing hemisphere distributions as a whole include contributions from the subleading and
 1498 leading jet peaks studied in correlation studies, but also a contribution from the underlying event.
 1499 In both PbPb and pp data, the underlying event partially cancels with hemisphere subtraction:
 1500 contributions from combinatoric background and even flow harmonics (V_2 etc.) will cancel, while
 1501 contributions from 3rd jets and odd flow harmonics (V_1, V_3 etc.) will not. As we have seen, in
 1502 pp the non-cancelling underlying event is dominated by 3rd jets, especially in the unbalanced dijet
 1503 selection in which their presence is kinematically required. In PbPb (where the contribution from
 1504 3rd jet events is smaller), this underlying event has evident contributions from odd flow harmonics
 1505 as well, reflecting coupling of jets to the event reaction plane.

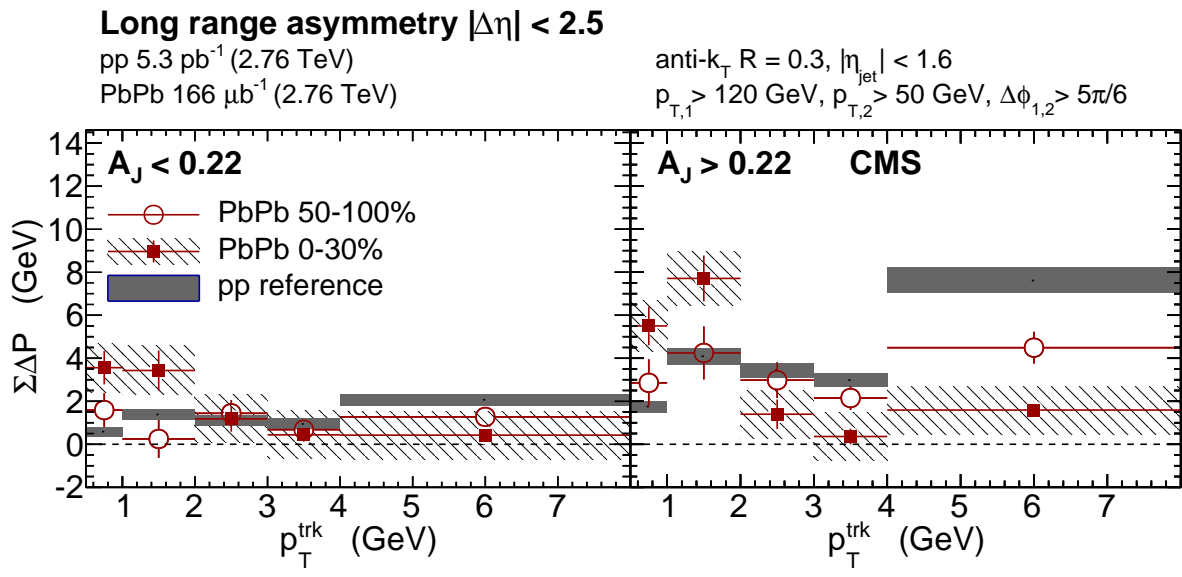


Figure 71. Integrated transverse momentum in the long-range $\Delta\phi$ -correlated distribution as a function of track- p_T integrated over $|\Delta\phi| < \pi/2$ and $|\Delta\eta| < 2.5$ and for pp reference, peripheral PbPb and central PbPb data for balanced compared to unbalanced dijets.

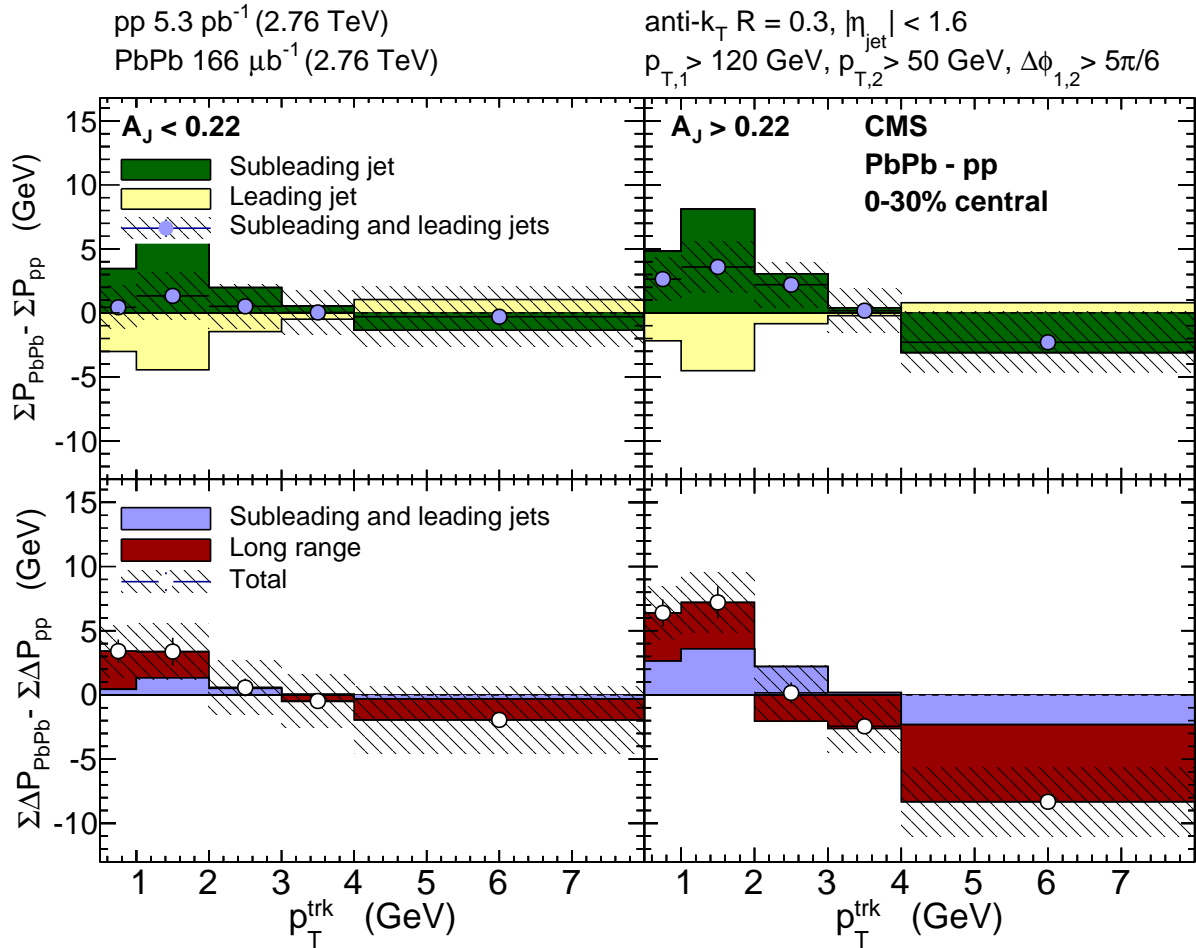


Figure 72. Modifications of jet-hadron correlated transverse momentum in central PbPb collisions with respect to pp reference, integrated $|\Delta\phi| < \pi/2$, $|\Delta\phi| < 2.5$. Top row: subleading and leading jet peak PbPb-pp. Bottom row: relative contributions from jet peaks and long-range asymmetry to the double difference PbPb-pp, subleading-leading in total hemisphere transverse momentum.

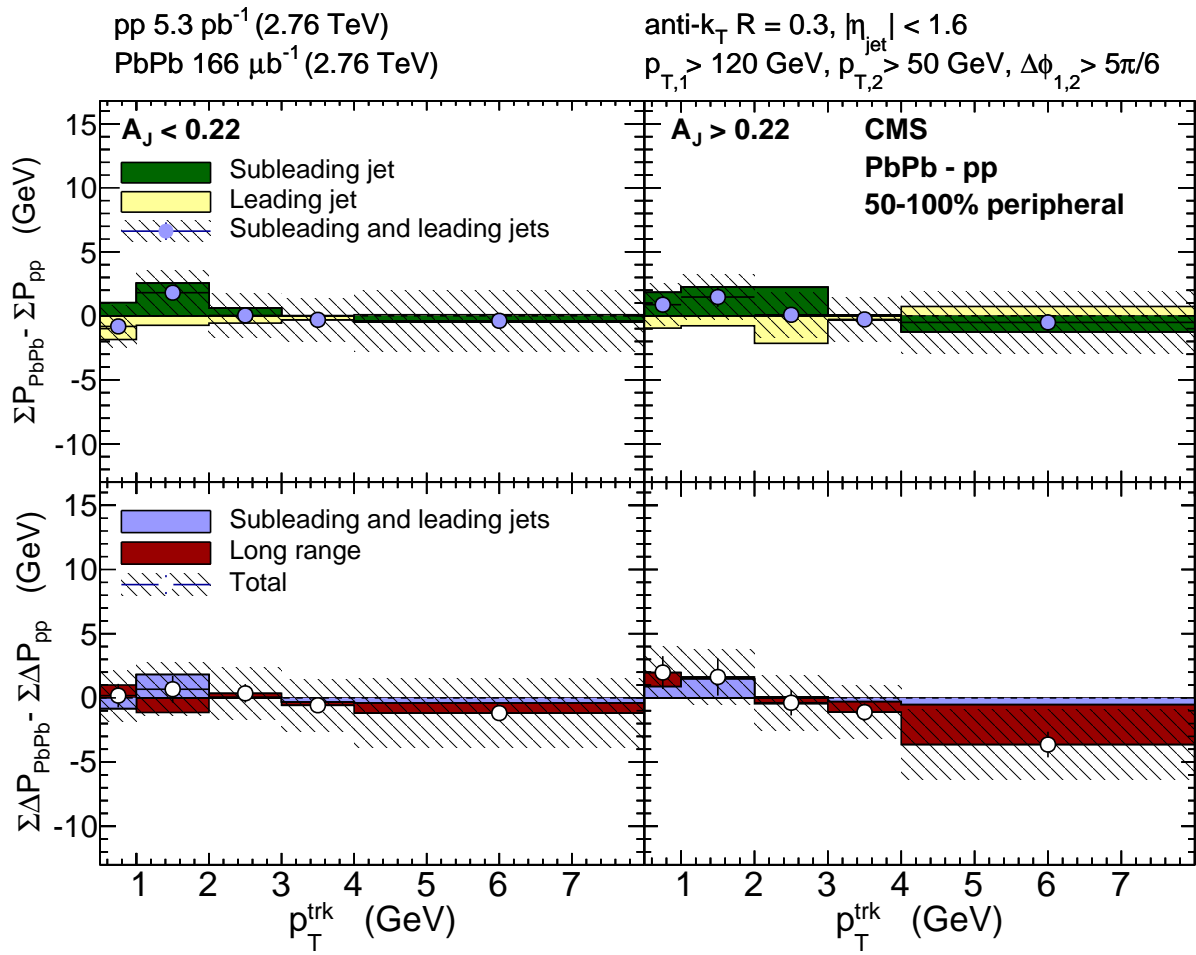


Figure 73. Modifications of jet-hadron correlated transverse momentum in peripheral PbPb collisions with respect to pp reference, integrated $|\Delta\phi| < \pi/2$, $|\Delta\phi| < 2.5$. Top row: subleading and leading jet peak PbPb-pp. Bottom row: relative contributions from jet peaks and long-range asymmetry to the double difference PbPb-pp, subleading-leading in total hemisphere transverse momentum.

1506 **10.5 Theory implications of these results**

11 CONCLUSION

REFERENCES

- 1509 [1] O. K. Kalashnikov and V. V. Klimov. Phase transition in the quark-gluon plasma. *Physics*
 1510 *Letters B*, 88:328–330, December 1979.
- 1511 [2] Edward V. Shuryak. Quantum Chromodynamics and the Theory of Superdense Matter. *Phys.*
 1512 *Rept.*, 61:71–158, 1980.
- 1513 [3] Siegfried Bethke. World Summary of α_s (2012). 2012. [Nucl. Phys. Proc. Suppl. 234, 229 (2013)].
- 1514 [4] J. D. Bjorken. Highly relativistic nucleus-nucleus collisions: The central rapidity region. *Phys.*
 1515 *Rev. D*, 27:140–151, Jan 1983.
- 1516 [5] Ulrich W. Heinz and Maurice Jacob. Evidence for a new state of matter: An Assessment of
 1517 the results from the CERN lead beam program. 2000.
- 1518 [6] I. Arsene et al. Quark-gluon plasma and color glass condensate at RHIC? The perspective
 1519 from the BRAHMS experiment. *Nucl. Phys. A*, 757:1, 2005.
- 1520 [7] K. Adcox et al. Formation of dense partonic matter in relativistic nucleus nucleus collisions at
 1521 RHIC: Experimental evaluation by the PHENIX collaboration. *Nucl. Phys. A*, 757:184, 2005.
- 1522 [8] B. B. Back et al. The PHOBOS perspective on discoveries at RHIC. *Nucl. Phys. A*, 757:28,
 1523 2005.
- 1524 [9] John Adams et al. Experimental and theoretical challenges in the search for the quark gluon
 1525 plasma: The STAR collaboration’s critical assessment of the evidence from RHIC collisions.
 1526 *Nucl. Phys. A*, 757:102, 2005.
- 1527 [10] Miklos Gyulassy. Introduction to qcd thermodynamics and the quark-gluon plasma. *Progress*
 1528 *in Particle and Nuclear Physics*, 15:403 – 442, 1985.
- 1529 [11] Sourav Sarkar, Helmut Satz, and Bikash Sinha. The physics of the quark-gluon plasma. *Lect.*
 1530 *Notes Phys.*, 785:pp.1–369, 2010.
- 1531 [12] Helmut Satz. Extreme states of matter in strong interaction physics. An introduction. *Lect.*
 1532 *Notes Phys.*, 841:1–239, 2012.

- 1533 [13] M. A. Stephanov. QCD phase diagram: An Overview. *PoS*, LAT2006:024, 2006.
- 1534 [14] Panagiota Foka and Małgorzata Anna Janik. An overview of experimental results from ultra-
1535 relativistic heavy-ion collisions at the cern lhc: Bulk properties and dynamical evolution.
1536 *Reviews in Physics*, 1:154 – 171, 2016.
- 1537 [15] Amaresh Jaiswal and Victor Roy. Relativistic hydrodynamics in heavy-ion collisions: general
1538 aspects and recent developments. *Adv. High Energy Phys.*, 2016:9623034, 2016.
- 1539 [16] Ulrich Heinz, Chun Shen, and Huichao Song. The viscosity of quark-gluon plasma at RHIC
1540 and the LHC. *AIP Conf. Proc.*, 1441:766–770, 2012.
- 1541 [17] Michael L. Miller, Klaus Reygers, Stephen J. Sanders, and Peter Steinberg. Glauber modeling
1542 in high energy nuclear collisions. *Ann. Rev. Nucl. Part. Sci.*, 57:205, 2007.
- 1543 [18] David G. d'Enterria. Hard scattering cross-sections at LHC in the Glauber approach: From
1544 pp to pA and AA collisions. 2003.
- 1545 [19] A. Majumder and M. Van Leeuwen. The Theory and Phenomenology of Perturbative QCD
1546 Based Jet Quenching. *Prog. Part. Nucl. Phys. A*, 66:41, 2011.
- 1547 [20] Sergei A. Voloshin, Arthur M. Poskanzer, and Raimond Snellings. Collective phenomena in
1548 non-central nuclear collisions. 2008.
- 1549 [21] Serguei Chatrchyan et al. Long-range and short-range dihadron angular correlations in central
1550 PbPb collisions at a nucleon-nucleon center of mass energy of 2.76 TeV. *JHEP*, 07:076, 2011.
- 1551 [22] Serguei Chatrchyan et al. Multiplicity and transverse momentum dependence of two- and
1552 four-particle correlations in pPb and PbPb collisions. *Phys. Lett.*, B724:213–240, 2013.
- 1553 [23] J. D. Bjorken. Energy loss of energetic partons in QGP: possible extinction of high p_t jets in
1554 hadron-hadron collisions. FERMILAB-PUB-82-059-THY, 1982.
- 1555 [24] David d'Enterria. Jet quenching. *Landolt-Boernstein, Springer-Verlag*, Vol. 1-23A:99, 2010.
- 1556 [25] Nestor Armesto. Nuclear shadowing. *J. Phys.*, G32:R367–R394, 2006.

- 1557 [26] K. Aamodt. Suppression of Charged Particle Production at Large Transverse Momentum in
 1558 Central PbPb Collisions at $\sqrt{s_{\text{NN}}} = 2.76$ TeV. *Phys. Lett. B*, 696:30, 2011.
- 1559 [27] Vardan Khachatryan et al. Charged-particle nuclear modification factors in PbPb and pPb
 1560 collisions at $\sqrt{s_{\text{NN}}} = 5.02$ TeV. *JHEP*, 04:039, 2017.
- 1561 [28] Georges Aad et al. Measurements of the Nuclear Modification Factor for Jets in Pb+Pb
 1562 Collisions at $\sqrt{s_{\text{NN}}} = 2.76$ TeV with the ATLAS Detector. *Phys. Rev. Lett.*, 114(7):072302,
 1563 2015.
- 1564 [29] Vardan Khachatryan et al. Measurement of inclusive jet cross-sections in pp and PbPb colli-
 1565 sions at $\sqrt{s_{\text{NN}}}=2.76$ TeV. *Phys. Rev. C*, 2016.
- 1566 [30] Serguei Chatrchyan et al. Measurement of jet fragmentation in PbPb and pp collisions at
 1567 $\sqrt{s_{\text{NN}}} = 2.76$ TeV. *Phys. Rev. C*, 90:024908, 2014.
- 1568 [31] Serguei Chatrchyan et al. Modification of jet shapes in PbPb collisions at $\sqrt{s_{\text{NN}}} = 2.76$ TeV.
 1569 *Phys. Lett. B*, 730:243, 2014.
- 1570 [32] C. Adler et al. Disappearance of back-to-back high- p_{T} hadron correlations in central Au+Au
 1571 collisions at $\sqrt{s_{\text{NN}}} = 200$ GeV. *Phys. Rev. Lett.*, 90:082302, 2003.
- 1572 [33] K. Aamodt et al. Particle-yield modification in jet-like azimuthal di-hadron correlations in
 1573 Pb-Pb collisions at $\sqrt{s_{\text{NN}}} = 2.76$ TeV. *Phys. Rev. Lett.*, 108:092301, 2012.
- 1574 [34] Georges Aad et al. Observation of a Centrality-Dependent Dijet Asymmetry in Lead-Lead
 1575 Collisions at $\sqrt{s_{\text{NN}}} = 2.76$ TeV with the ATLAS Detector at the LHC. *Phys. Rev. Lett.*,
 1576 105:252303, 2010.
- 1577 [35] Serguei Chatrchyan et al. Observation and studies of jet quenching in PbPb collisions at $\sqrt{s_{\text{NN}}}$
 1578 = 2.76 TeV. *Phys. Rev. C*, 84:024906, 2011.
- 1579 [36] Lyndon Evans and Philip Bryant. LHC Machine. *JINST*, 3:S08001, 2008.
- 1580 [37] S. Chatrchyan et al. The CMS experiment at the CERN LHC. *JINST*, 3:S08004, 2008.
- 1581 [38] Tai Sakuma and Thomas McCauley. Detector and event visualization with sketchup at the
 1582 cms experiment. *Journal of Physics: Conference Series*, 513(2):022032, 2014.

- 1583 [39] Serguei Chatrchyan et al. Description and performance of track and primary-vertex recon-
 1584 struction with the CMS tracker. *JINST*, 9(10):P10009, 2014.
- 1585 [40] Vardan Khachatryan et al. Performance of photon reconstruction and identification with the
 1586 CMS detector in proton-proton collisions at $\sqrt{s_{\text{NN}}} = 8$ TeV. *JINST*, 10:P08010, 2015.
- 1587 [41] Vardan Khachatryan et al. The CMS trigger system. *JINST*, 12:P01020, 2017.
- 1588 [42] CMS Collaboration. Momentum flow relative to dijets in pbpb collisions at 2.76 tev. *CMS*
 1589 *Analysis Note (Internal)*, AN-14-024, 2014.
- 1590 [43] CMS Internal. Study of high- p_t charged particle suppression in pbpb compared to pp collisions
 1591 at 5.02 tev. 2016.
- 1592 [44] Gavin P. Salam. Towards Jetography. *Eur. Phys. J.*, C67:637–686, 2010.
- 1593 [45] Matteo Cacciari, Gavin P. Salam, and Gregory Soyez. The anti- k_t jet clustering algorithm.
 1594 *JHEP*, 04:063, 2008.
- 1595 [46] Matteo Cacciari, Gavin P. Salam, and Gregory Soyez. FastJet user manual. *Eur. Phys. J. C*,
 1596 72:1896, 2012.
- 1597 [47] Olga Kodolova, I. Vardanian, A. Nikitenko, and A. Oulianov. The performance of the jet
 1598 identification and reconstruction in heavy ions collisions with CMS detector. *Eur. Phys. J. C*,
 1599 50:117, 2007.
- 1600 [48] Serguei Chatrchyan et al. Studies of jet quenching using isolated-photon+jet correlations in
 1601 PbPb and pp collisions at $\sqrt{s_{\text{NN}}} = 2.76$ TeV. *Phys. Lett. B*, 718:773, 2013.
- 1602 [49] Serguei Chatrchyan et al. Measurement of jet fragmentation into charged particles in pp and
 1603 PbPb collisions at $\sqrt{s_{\text{NN}}} = 2.76$ TeV. *JHEP*, 10:087, 2012.
- 1604 [50] CMS. Identification and Filtering of Uncharacteristic Noise in the CMS Hadron Calorimeter.
 1605 *JINST*, 5:T03014, 2010.
- 1606 [51] Torbjorn Sjöstrand, Stephen Mrenna, and Peter Skands. PYTHIA 6.4 physics and manual.
 1607 *JHEP*, 05:026, 2006.

- 1608 [52] S. Agostinelli et al. GEANT4—a simulation toolkit. *Nucl. Instrum. and Methods A*, 506:250,
1609 2003.
- 1610 [53] I. P. Lokhtin and A. M. Snigirev. A model of jet quenching in ultrarelativistic heavy ion
1611 collisions and high- p_T hadron spectra at RHIC. *Eur. Phys. J. C*, 45:211, 2006.
- 1612 [54] Vardan Khachatryan et al. Measurement of transverse momentum relative to dijet systems in
1613 PbPb and pp collisions at $\sqrt{s_{\text{NN}}} = 2.76$ TeV. *JHEP*, 01:6, 2016.
- 1614 [55] S. Chatrchyan et al. Azimuthal anisotropy of charge particles at high transvere momenta in
1615 pb-pb collisions at $\sqrt{s_{\text{NN}}} = 2.76$ TeV. *Phys. Rev. Lett.*, 109:022301, 2012.
- 1616 [56] Serguei Chatrchyan et al. Centrality dependence of dihadron correlations and azimuthal
1617 anisotropy harmonics in PbPb collisions at $\sqrt{s_{\text{NN}}} = 2.76$ TeV. *Eur. Phys. J.*, C72:2012,
1618 2012.
- 1619 [57] K. Aamodt et al. Harmonic decomposition of two-particle angular correlations in Pb-Pb
1620 collisions at $\sqrt{s_{\text{NN}}} = 2.76$ TeV. *Phys. Lett. B*, 708:249, 2012.

APPENDICES

1622 A Jet kinematics

1623 The following sections summarize jet kinematics for inclusive jets and dijets at 2.76 TeV, for inclu-
 1624 sive jets at 5.02 TeV, and for dijets in each asymmetry class at 2.76 TeV.

1625 A.1 Jet kinematics at 2.76 TeV

1626 The kinematic observables of jets in pp and PbPb 2.76 TeV events (solid markers) are compared
 1627 with Monte Carlo (hatched marks). All spectra have been normalized to unity. Comparing the jet
 1628 spectra observed in PbPb data (pp data) and in PYTHIA+HYDJET (PYTHIA) samples, a reasonable
 1629 agreement in the overall shape is found.

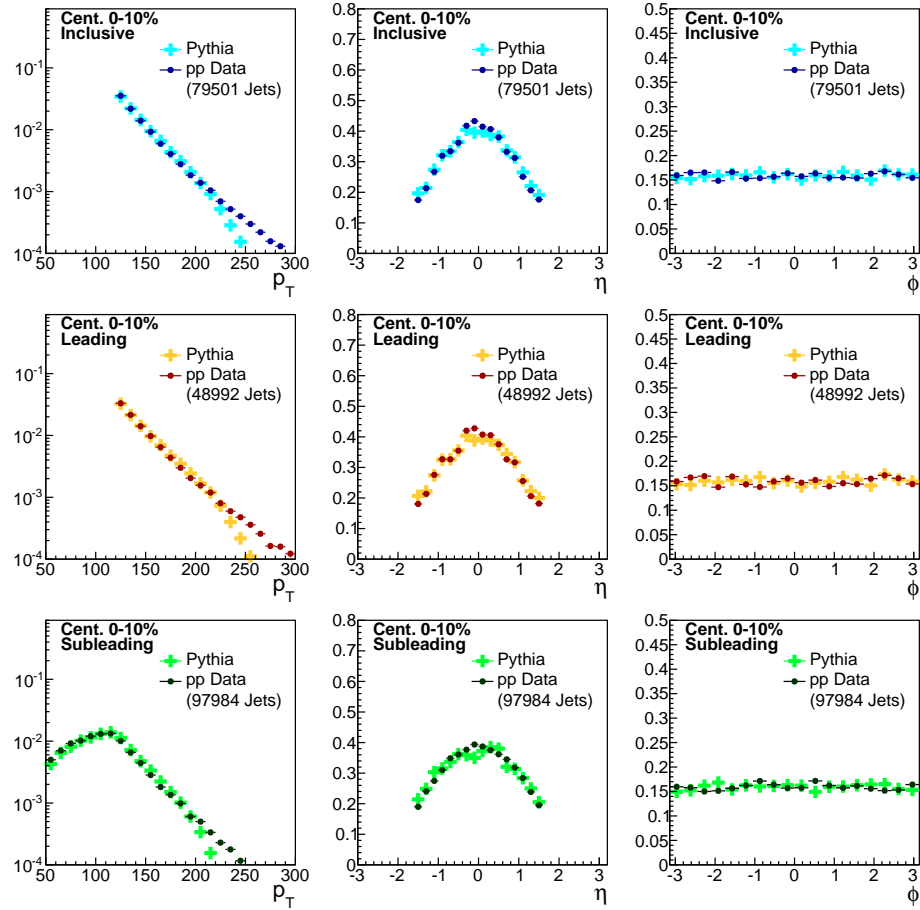


Figure 74. Distribution of transverse momentum, pseudorapidity, and azimuthal distribution of all jet selections for Pythia data compared to PYTHIA simulation.

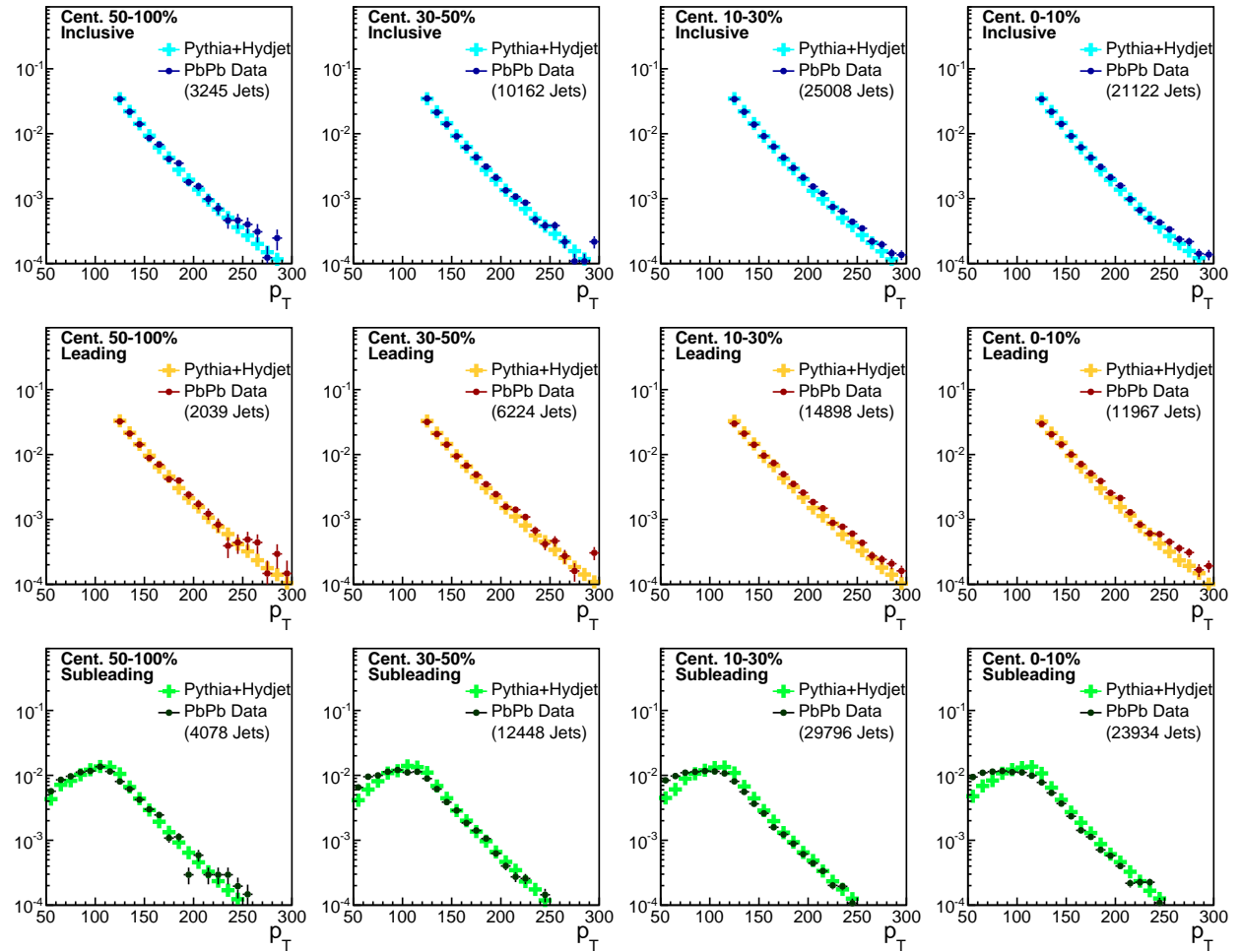


Figure 75. Transverse momentum distribution of all jet selections for PbPb data at 2.76 TeV compared to PYTHIA+HYDJET simulation.

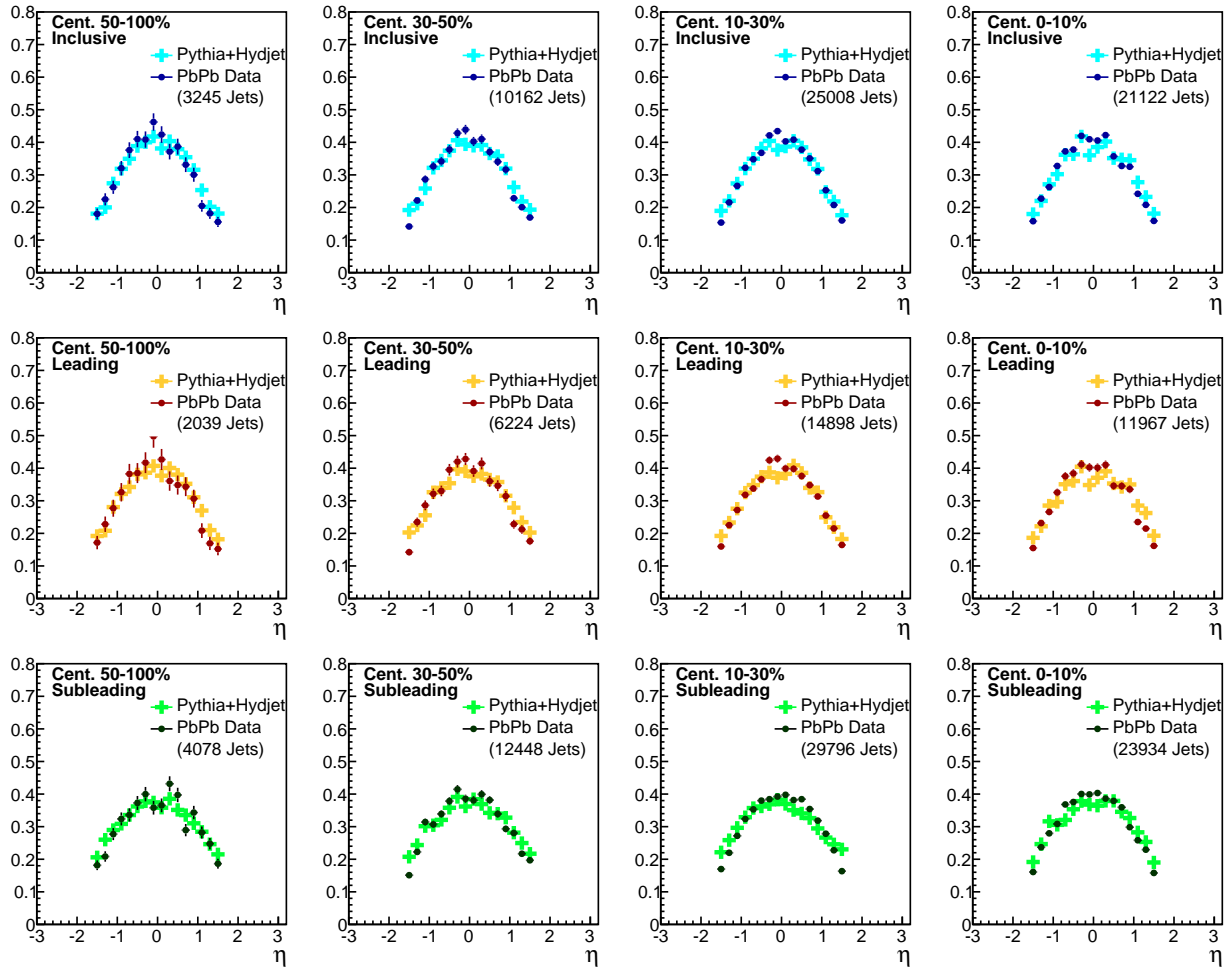


Figure 76. Pseudorapidity distribution of all jet selections for PbPb data at 2.76 TeV compared to PYTHIA + HYDJET simulation.

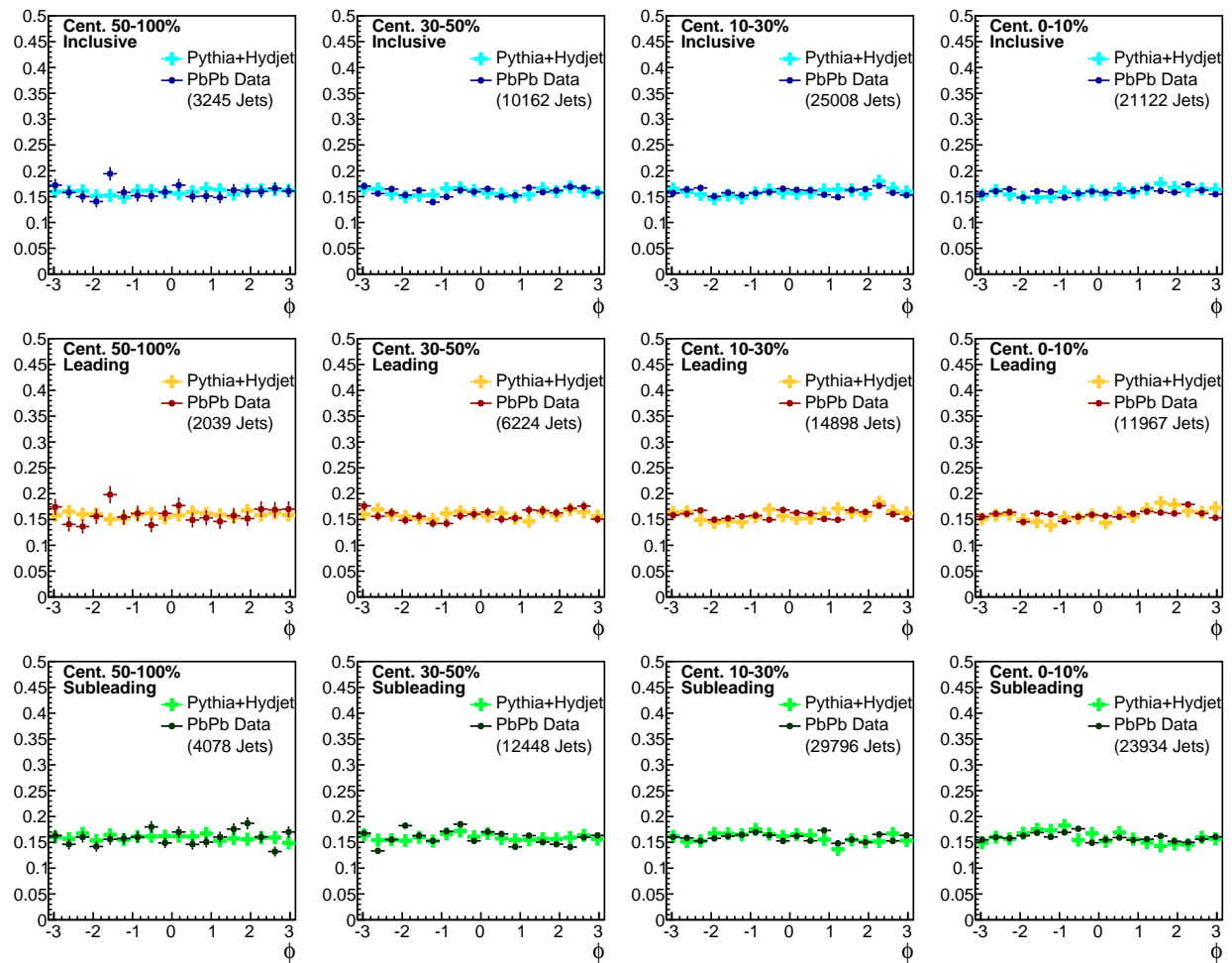


Figure 77. Azimuthal angle distribution of all jet selections for PbPb data at 2.76 TeV compared to PYTHIA+HYDJET simulation for each collision centrality bin.

1630 **A.2 Inclusive jet kinematics at 5.02 TeV**

1631 Jet p_T , η , and ϕ distributions for 5.02 TeV data, comparing PbPb data to PYTHIA+HYDJET and
 1632 pp data to PYTHIA simulation.

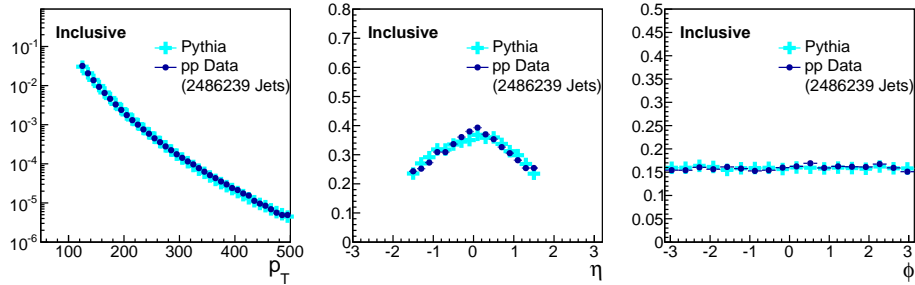


Figure 78. Distribution of pseudorapidity distribution of all jet selections for PbPb data compared to PYTHIA+HYDJet simulation for each collision centrality bin.

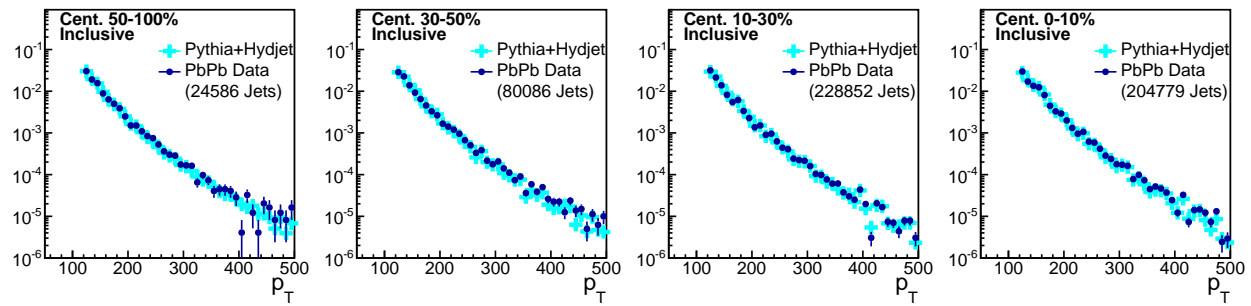


Figure 79. Transverse momentum distribution for PbPb data compared to PYTHIA+HYDJet simulation for each collision centrality bin.

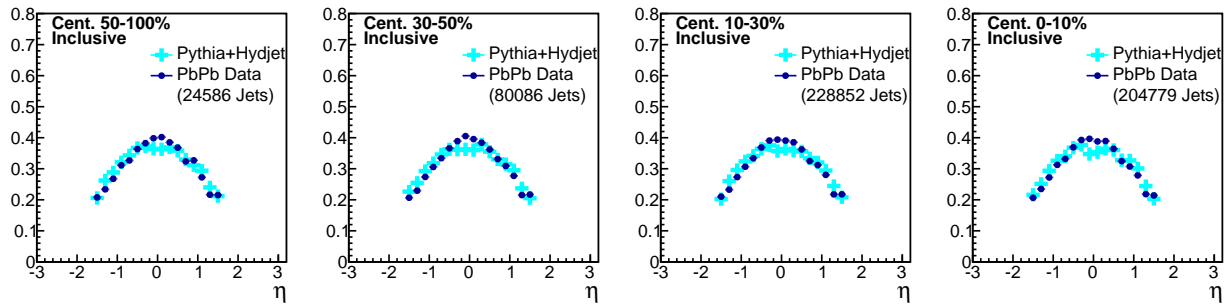


Figure 80. Jet η distribution for PbPb data compared to PYTHIA+HYDJet simulation for each collision centrality bin.

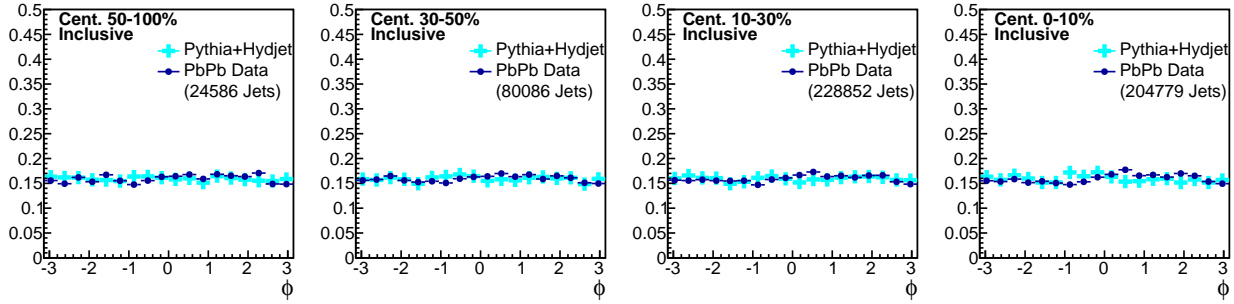


Figure 81. Jet ϕ distribution for PbPb data compared to PYTHIA+HYDJET simulation for each collision centrality bin.

¹⁶³³ **A.3 Dijet kinematics in asymmetry classes at 2.76 TeV**

¹⁶³⁴ In the figures below, jet transverse momentum, pseudorapidity, and azimuth are shown for our A_J -
¹⁶³⁵ inclusive sample, compared to each A_J selection in our analysis. Note that A_J -selection primarily
¹⁶³⁶ affects the subleading jet spectrum, while the leading jet spectrum is nearly unchanged. Jet η and
¹⁶³⁷ jet ϕ exhibit no significant A_J -dependence for leading or subleading jets. Distributions are shown
¹⁶³⁸ first for pp, and then for PbPb data at 2.76 TeV.

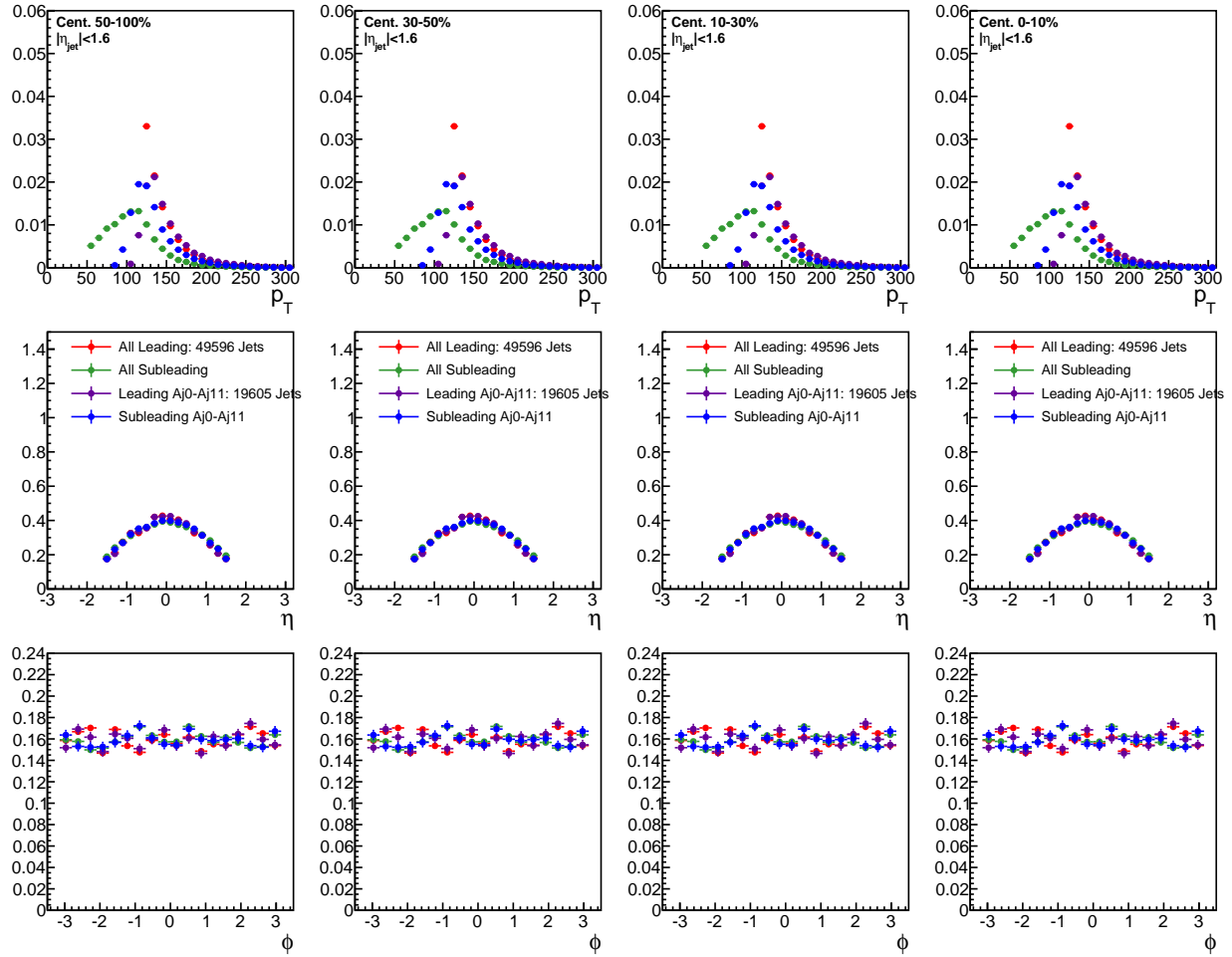


Figure 82. Jet p_T , η , and ϕ for all pp dijets and for pp dijets with A_J : $0 < A_J < 0.11$.

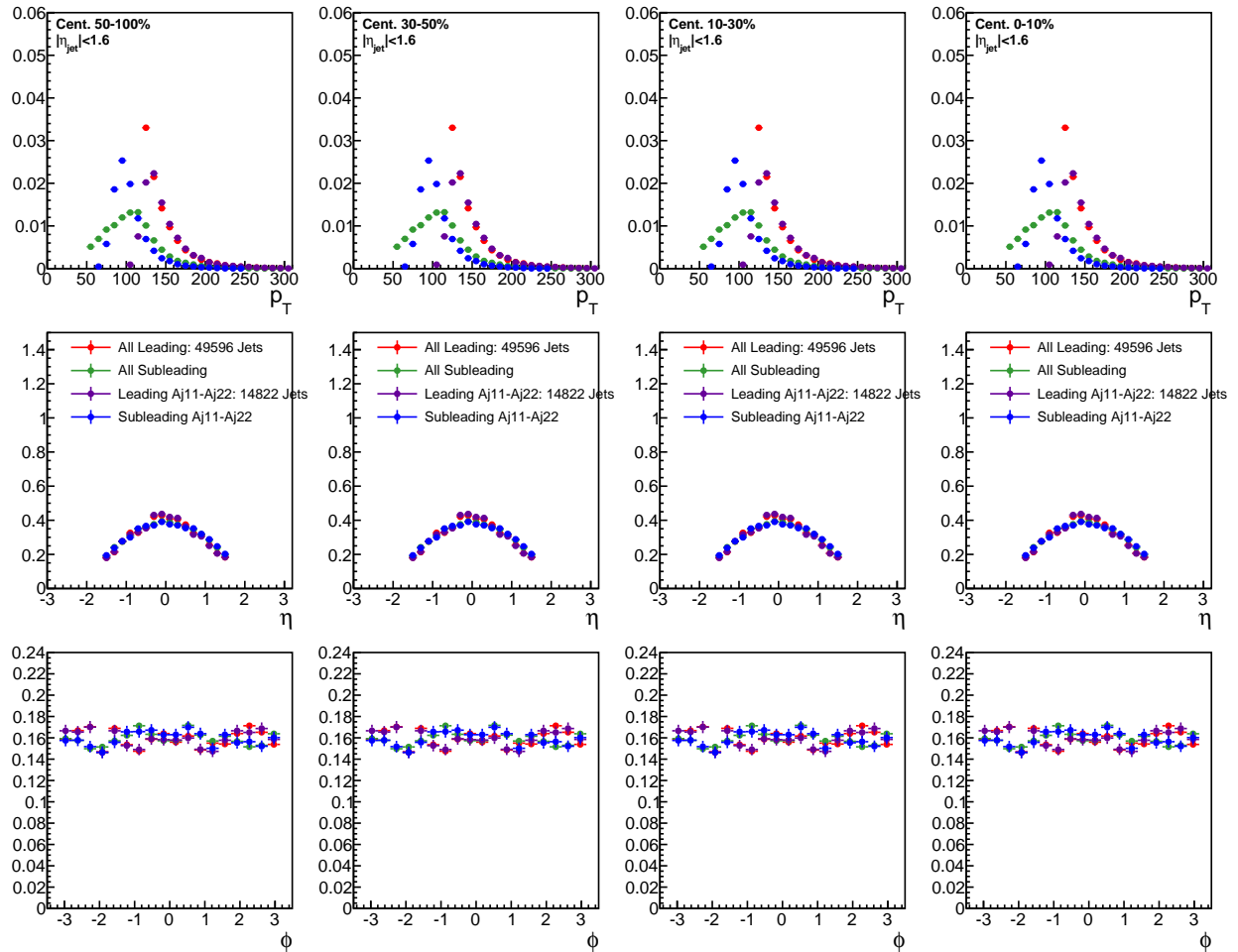


Figure 83. Jet p_T , η , and ϕ for all pp dijets and for pp dijets with A_J : $0.11 < A_J < 0.22$.

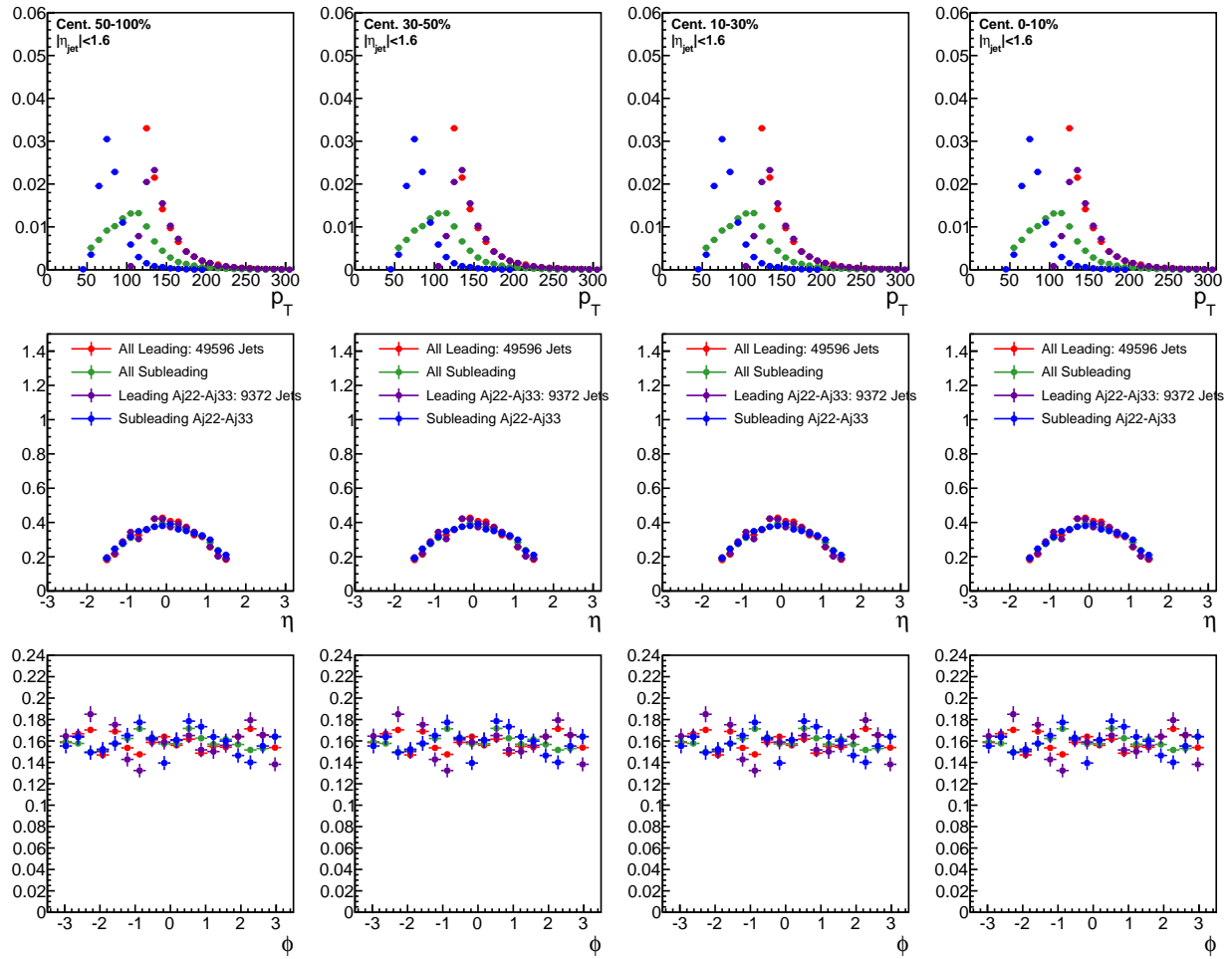


Figure 84. Jet p_T , η , and ϕ for all pp dijets and for pp dijets with A_J : $0.22 < A_J < 0.33$.

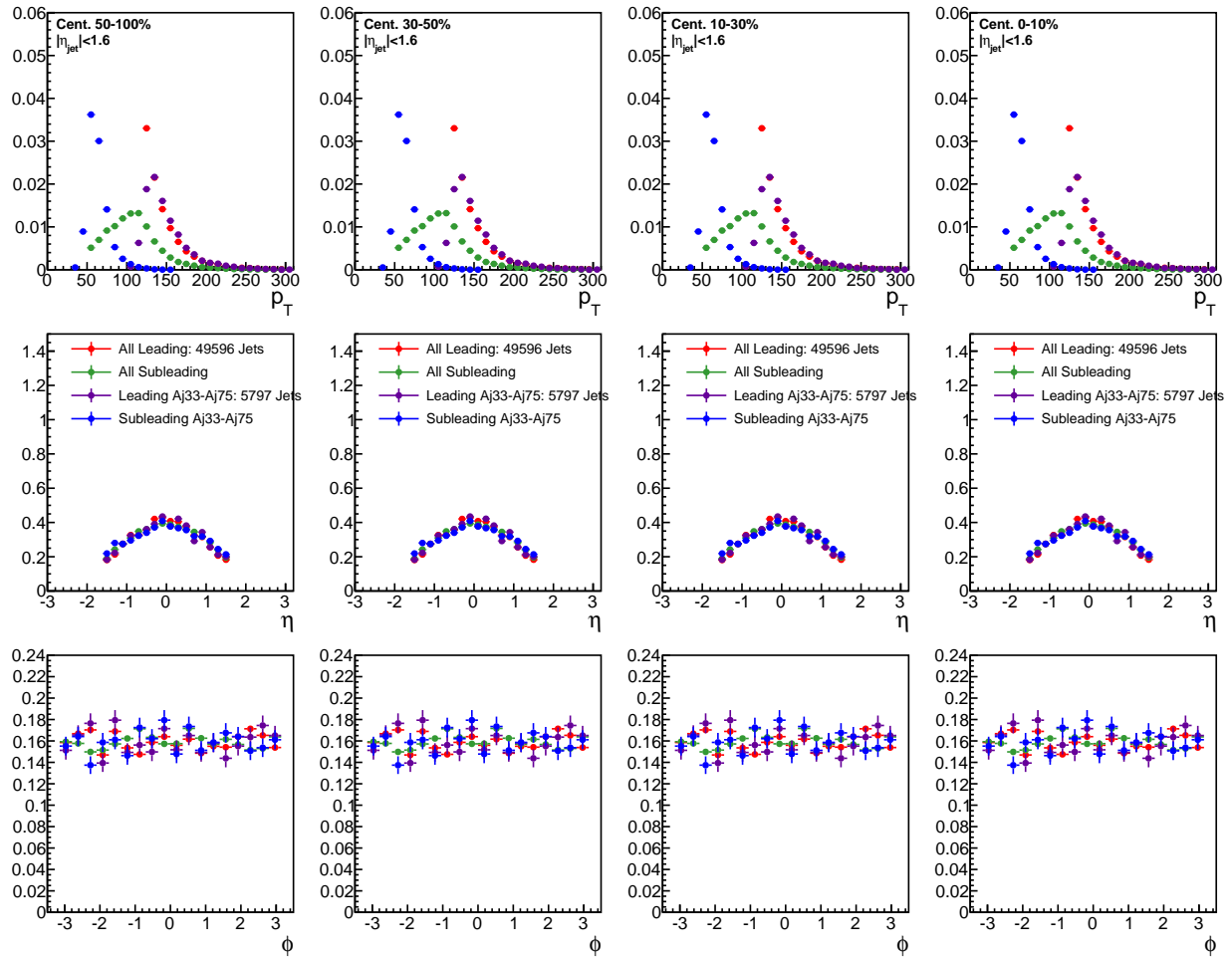


Figure 85. Jet p_T , η , and ϕ for all pp dijets and for pp dijets with A_J : $A_J > 0.33$.

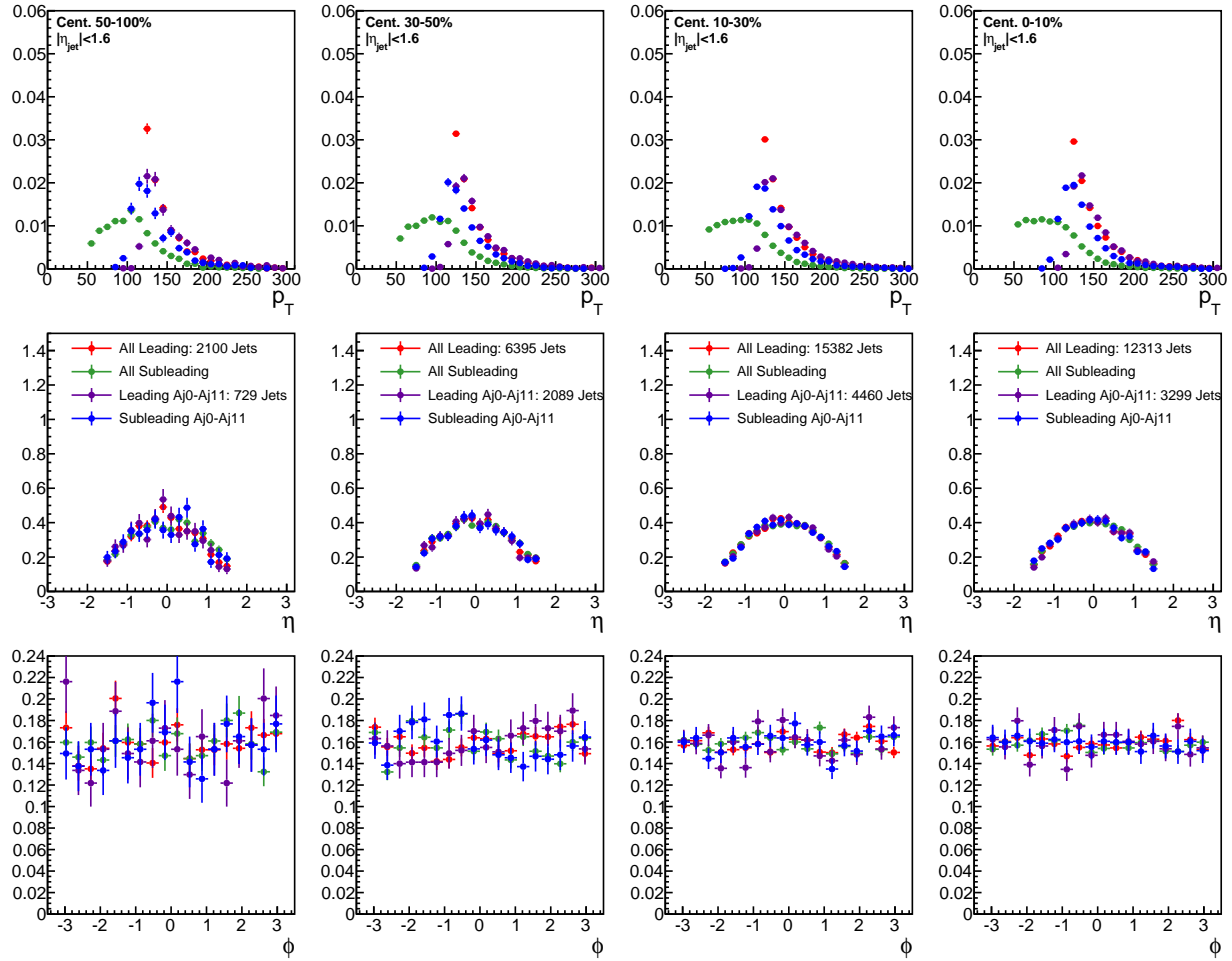


Figure 86. Jet p_T , η , and ϕ for all PbPb dijets and for PbPb dijets with $0 < A_J < 0.11$.

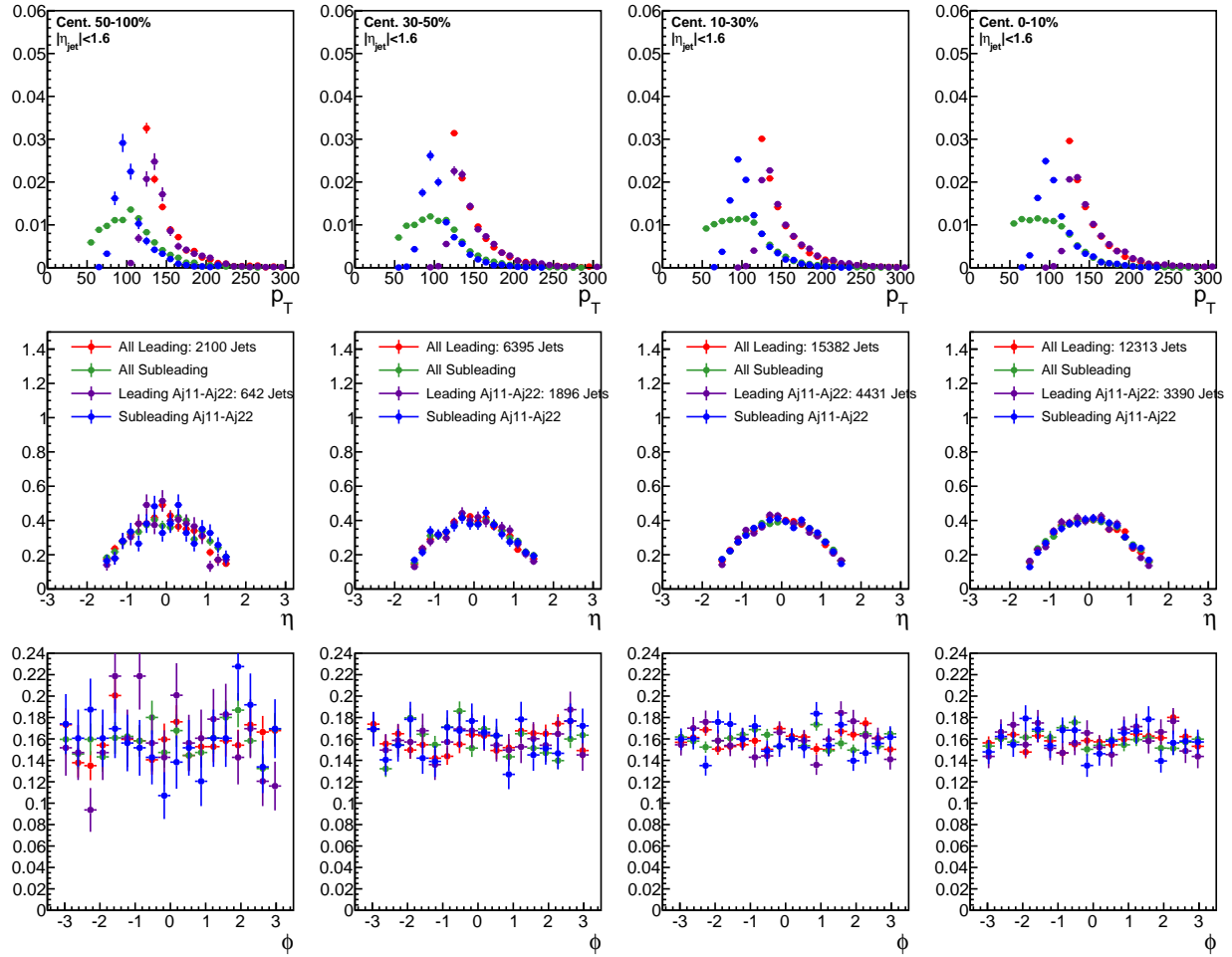


Figure 87. Jet p_T , η , and ϕ for all PbPb dijets and for PbPb dijets with $0.11 < A_J < 0.22$.

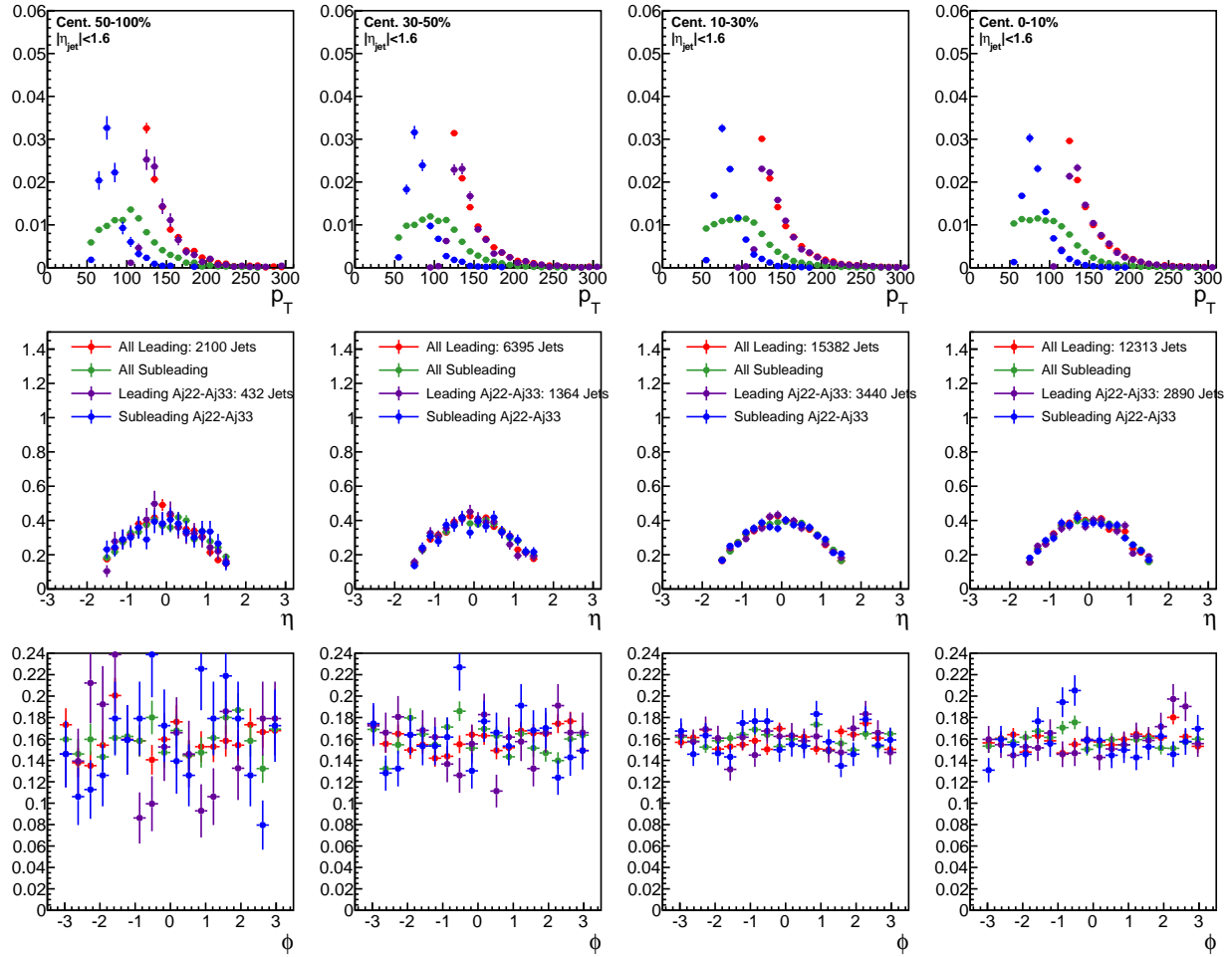


Figure 88. Jet p_T , η , and ϕ for all PbPb dijets and for PbPb dijets with $0.22 < A_J < 0.33$.

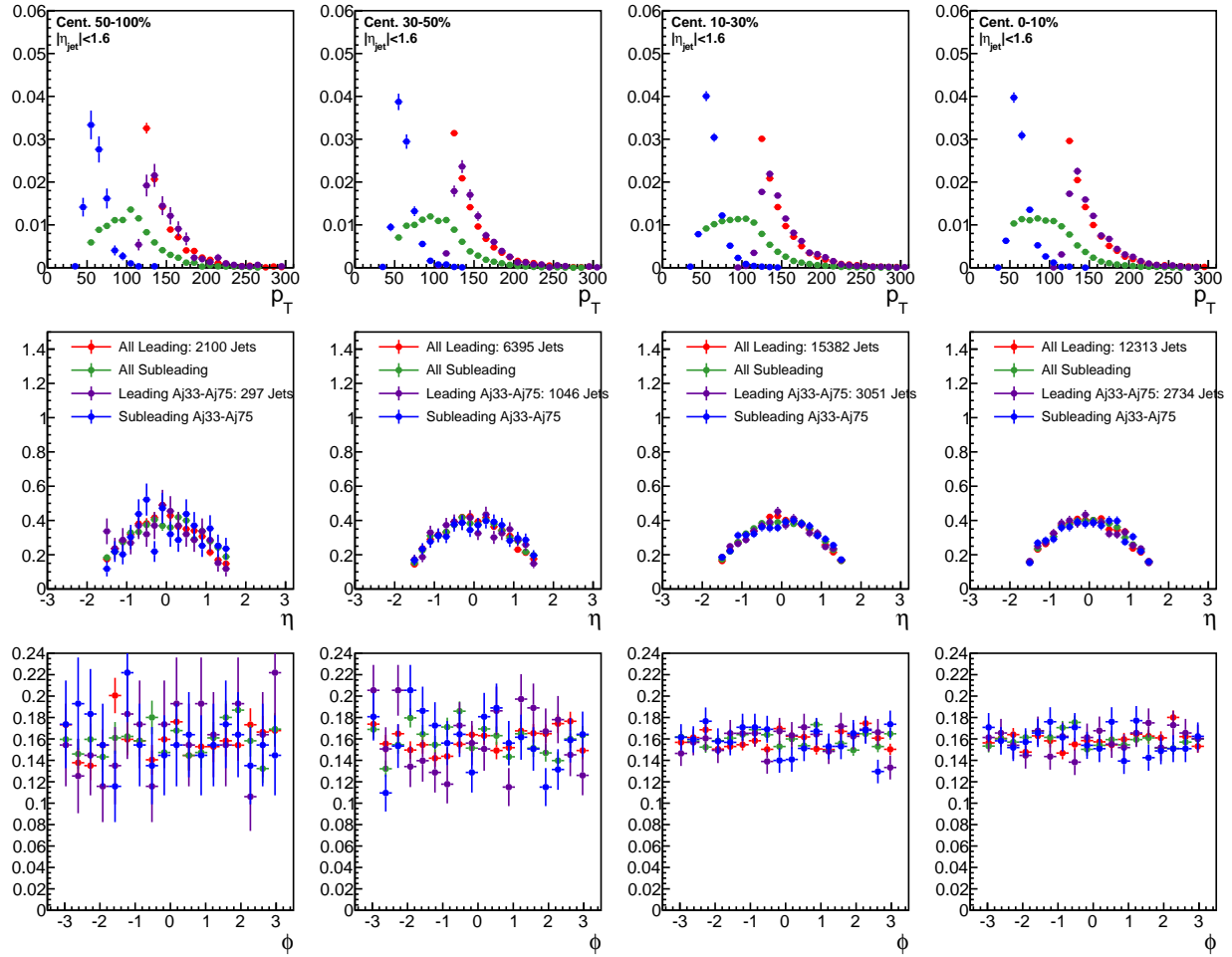


Figure 89. Jet p_T , η , and ϕ for all PbPb dijets and for PbPb dijets with $A_J > 0.33$.

1639 **B Background fitting details**

1640 Figures 90-93 show the two steps of fits involved in modeling the background distribution in
 1641 $\Delta\phi$, as discussed in section 9.3.

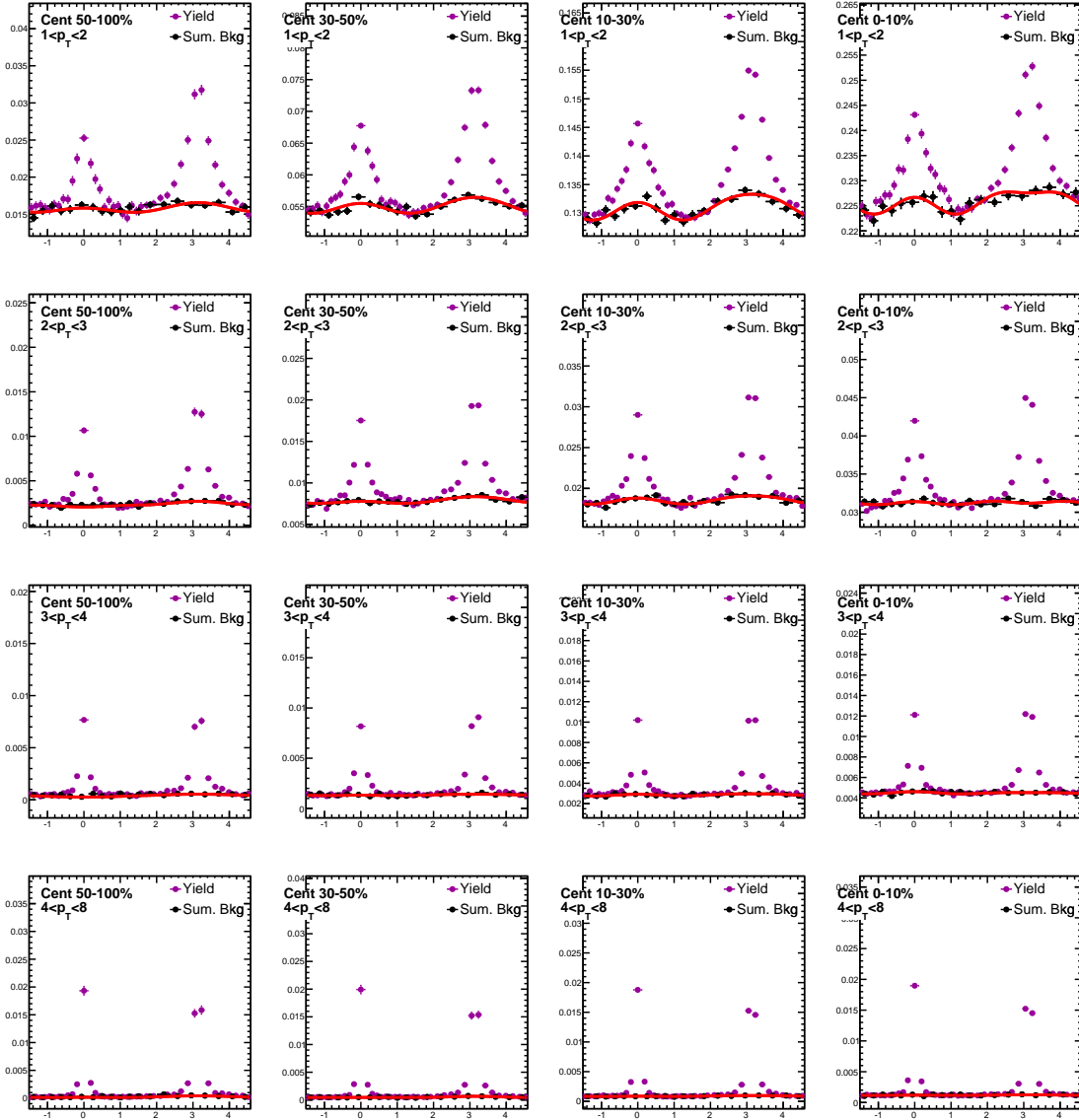


Figure 90. Dijet combined background $\Delta\phi$ distributions, estimated by projection over the region $1.5 < |\Delta\eta| < 3.0$. Here the "near-side" region $-\frac{\pi}{2} < \Delta\phi < \frac{\pi}{2}$ is taken from the leading jet correlation, while the "away-side" $-\frac{\pi}{2} < \Delta\phi < \frac{\pi}{2}$ is taken from the subleading jet correlation. The resulting combined background distribution is fit with the function $B^{dijet}(\Delta\phi) = B_0(1 + 2V_1\cos(\Delta\phi) + 2V_2\cos(2\Delta\phi) + 2V_3\cos(3\Delta\phi))$.

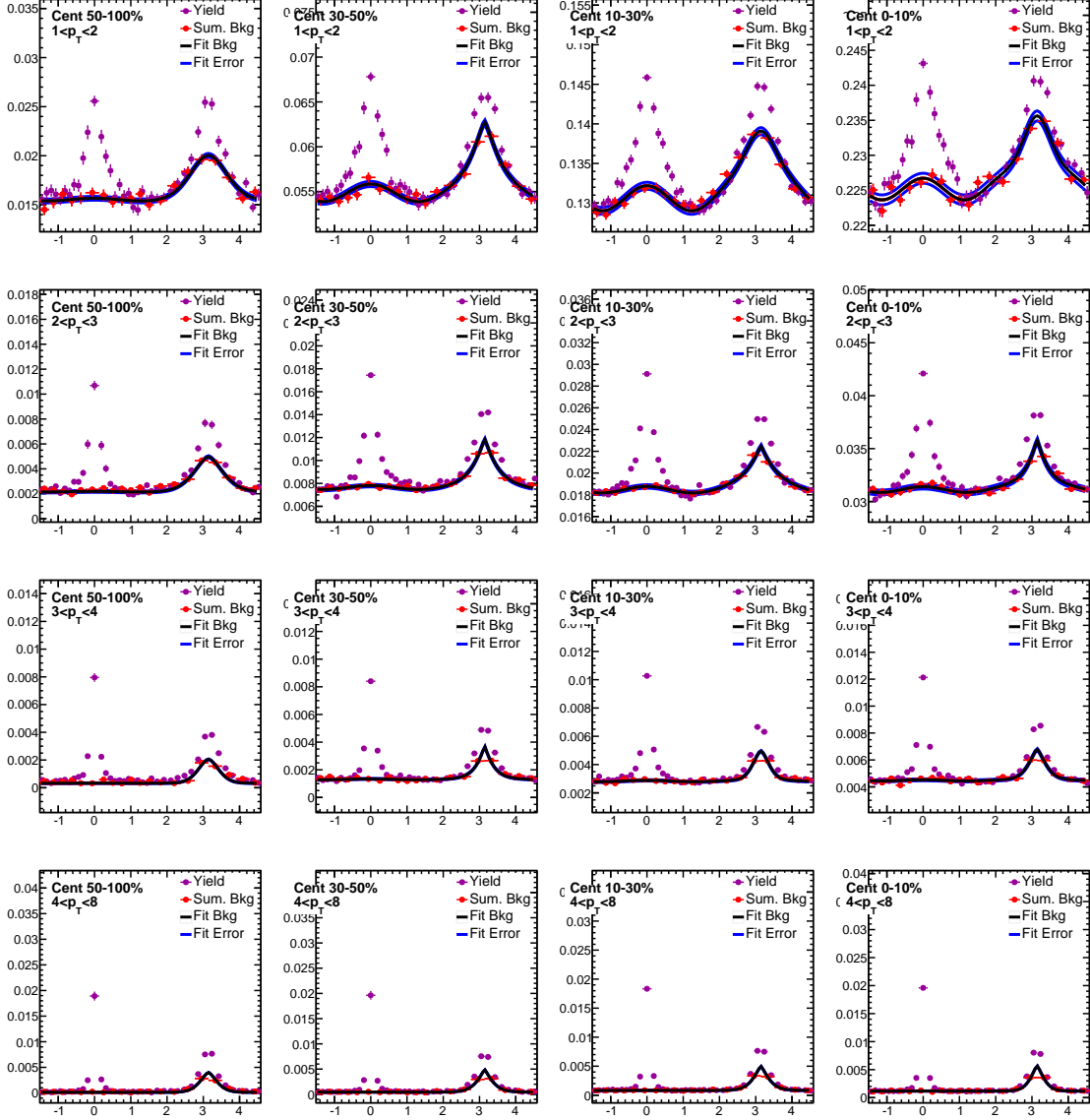


Figure 91. Background leading jet $\Delta\phi$ distributions, estimated by projection over the region $1.5 < |\Delta\eta| < 3.0$, is fit as shown. The 2D background distribution is estimated by propagating the black fit line in $\Delta\eta$, with uncertainty assigned by varying fit parameters by the appropriate fit error as shown in the blue error band.

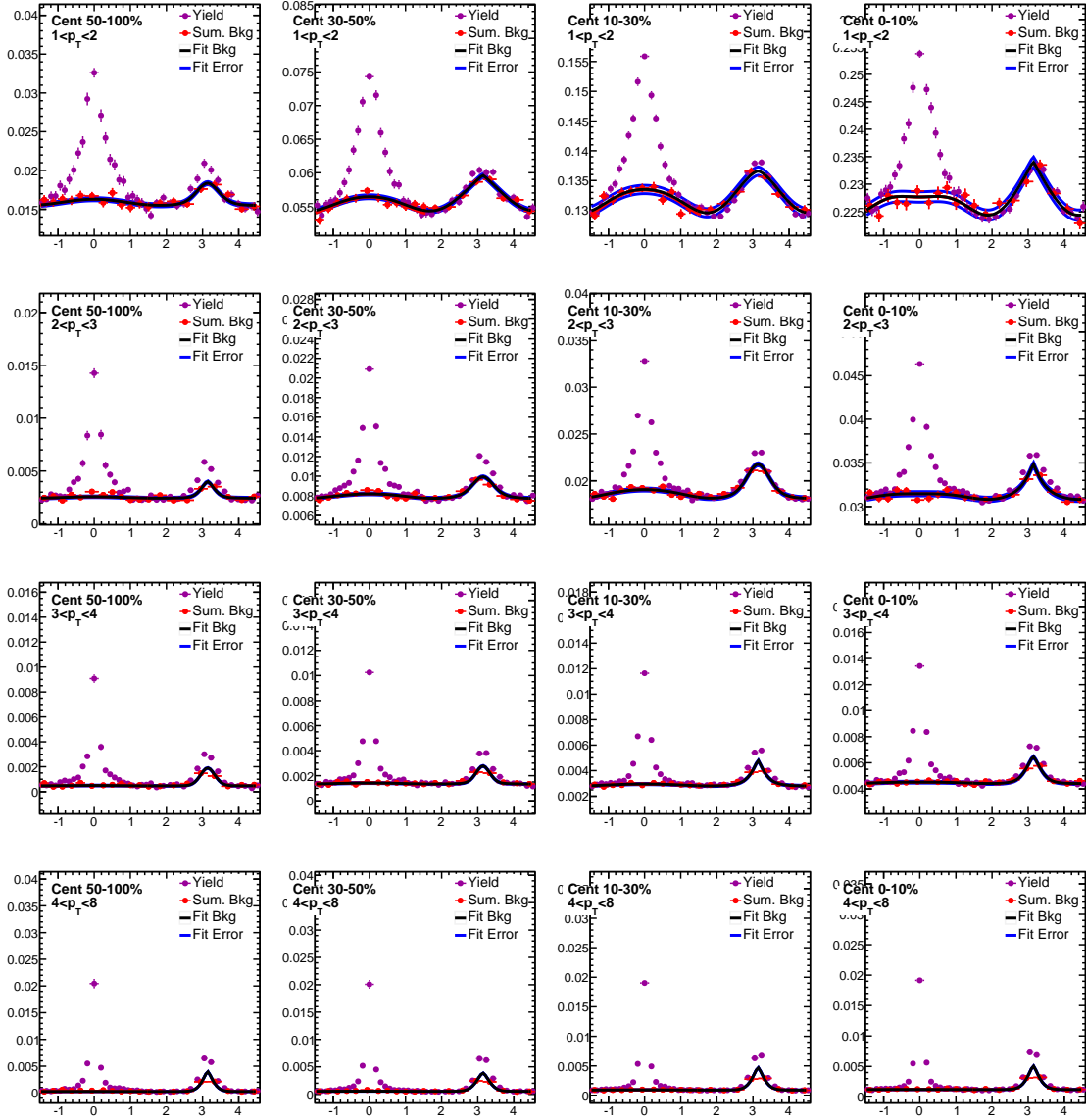


Figure 92. Background subleading jet $\Delta\phi$ distributions, estimated by projection over the region $1.5 < |\Delta\eta| < 3.0$, is fit as shown. The 2D background distribution is estimated by propagating the black fit line in $\Delta\eta$, with uncertainty assigned by varying fit parameters by the appropriate fit error as shown in the blue error band.

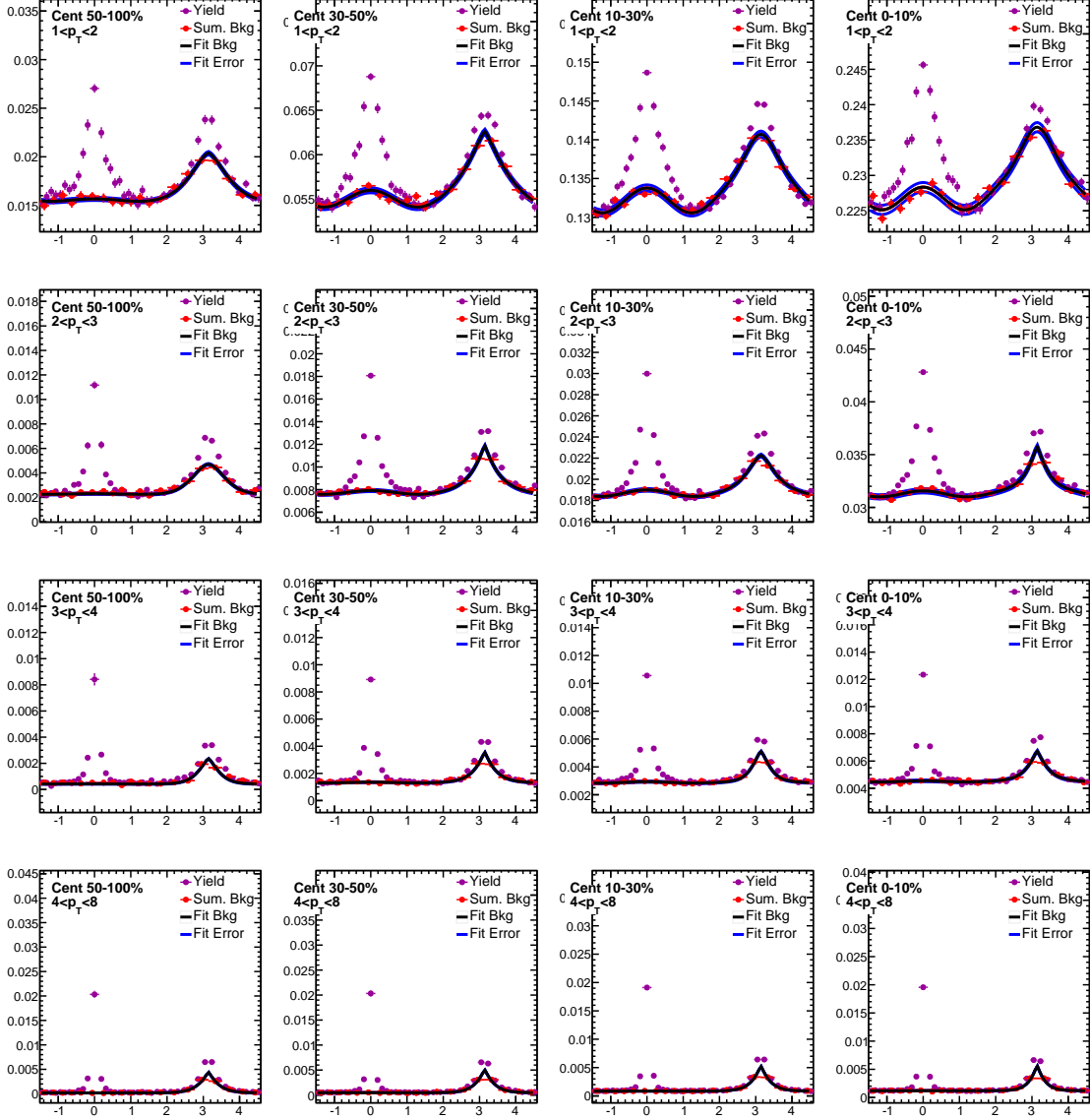


Figure 93. Background inclusive jet $\Delta\phi$ distributions, estimated by projection over the region $1.5 < |\Delta\eta| < 3.0$, is fit as shown. The 2D background distribution is estimated by propagating the black fit line in $\Delta\eta$, with uncertainty assigned by varying fit parameters by the appropriate fit error as shown in the blue error band.

1642 **C Pair acceptance and event decomposition systematic uncertainties**

1643 Figure 94 illustrates the estimation of pair-acceptance uncertainty, determined by considering the
 1644 sideband asymmetry in the $\Delta\eta$ distributions of background subtracted yield.

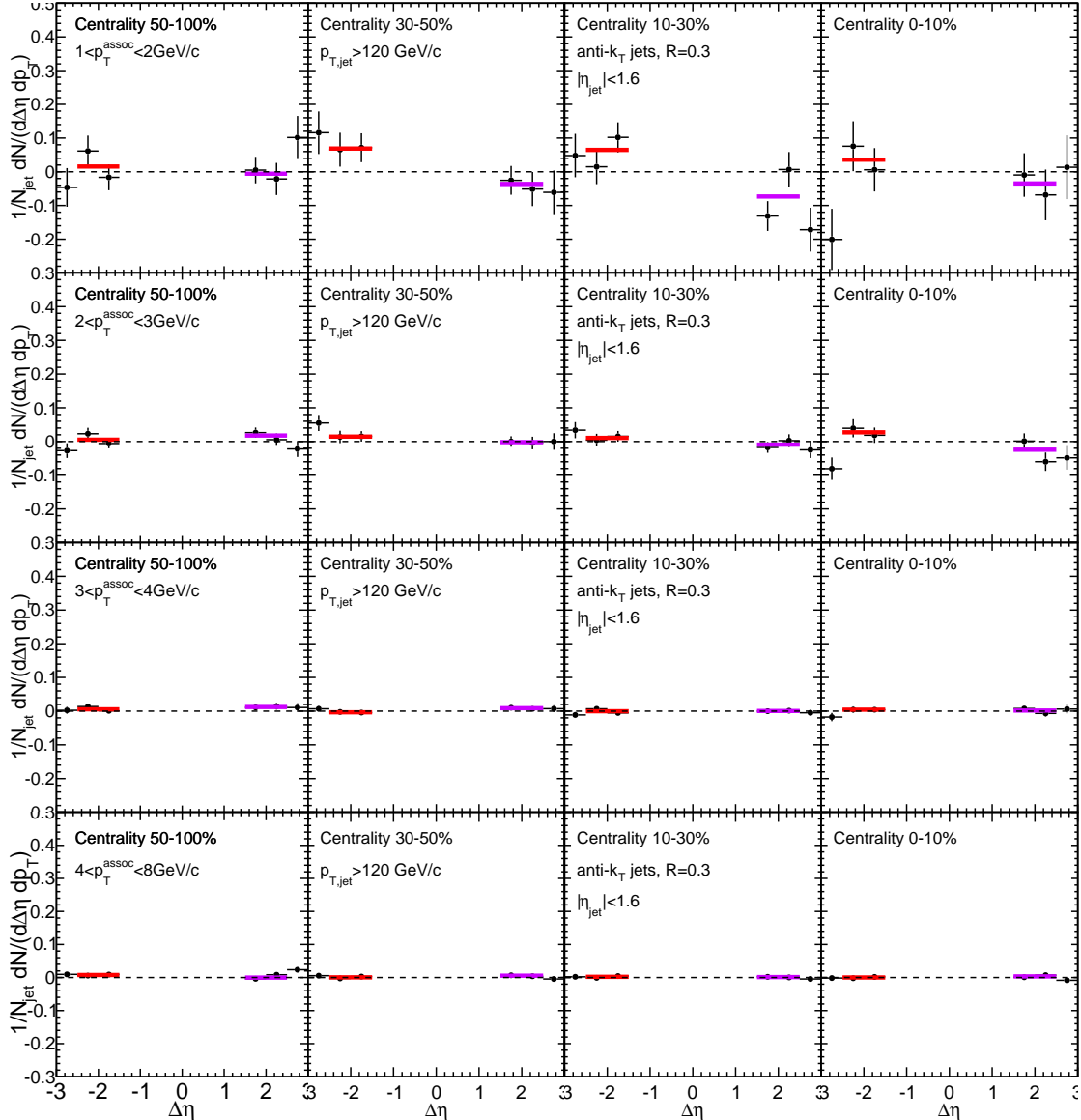


Figure 94. Background-subtracted inclusive jet $\Delta\eta$ distribution is shown for sideband region $1.5 < |\Delta\eta| < 3.0$ only. Each side is fit separately with a horizontal line, and the greater deviation from zero is assigned as systematic uncertainty arising from the pair-acceptance correction.

1645 Figure 95 illustrates the background-subtraction systematic uncertainty estimation: the average
 1646 content of the two $1.5 < \Delta\eta < 2.0$ bins is assigned as systematic uncertainty for each p_T and
 1647 centrality bin.

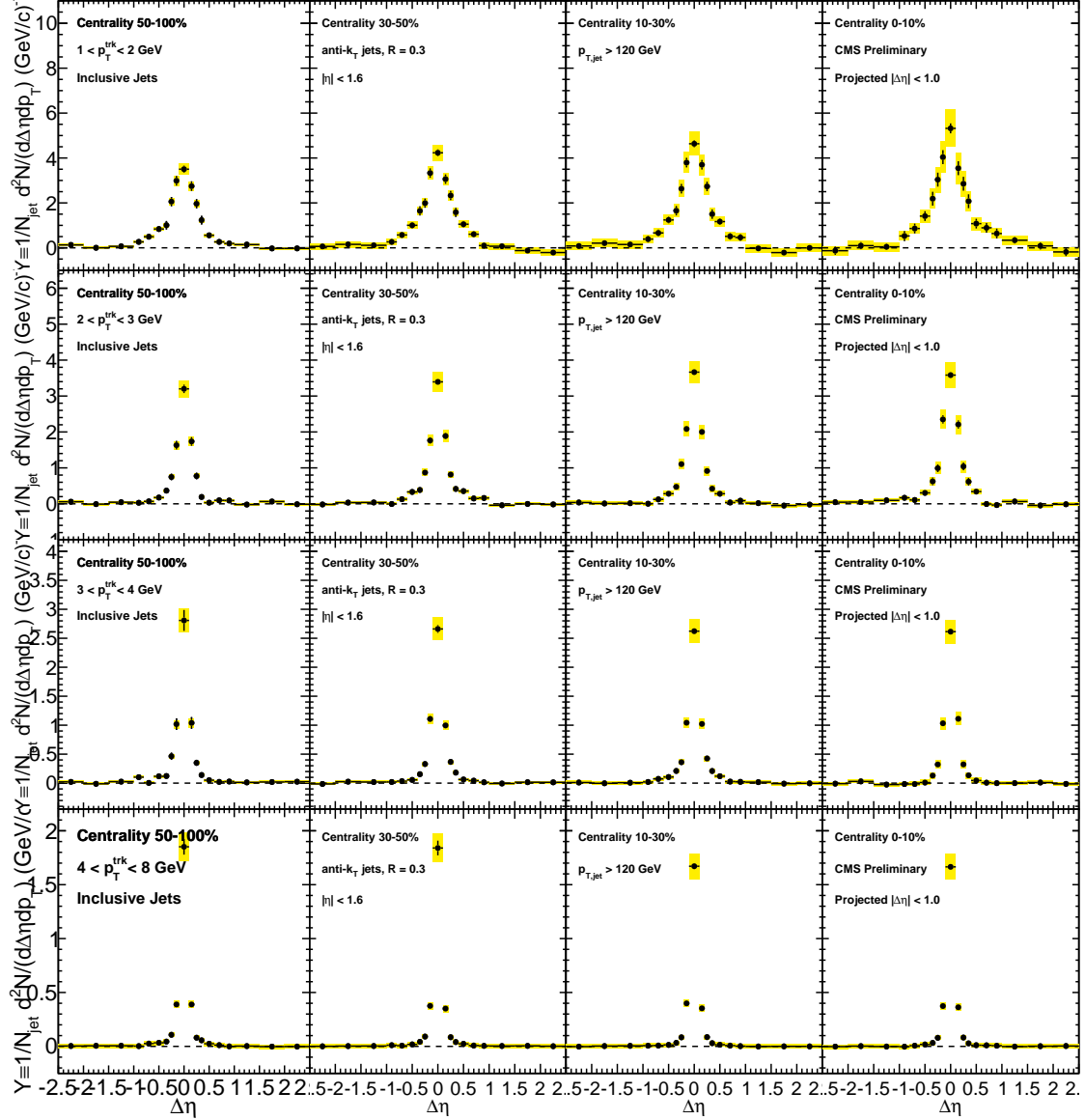


Figure 95. Inclusive jet correlated yield in $\Delta\eta$, shown to axis range $|\Delta\eta| < 2.0$. The deviation of the most peripheral points from zero is assigned as systematic uncertainty as discussed in the Systematic Uncertainty section above.

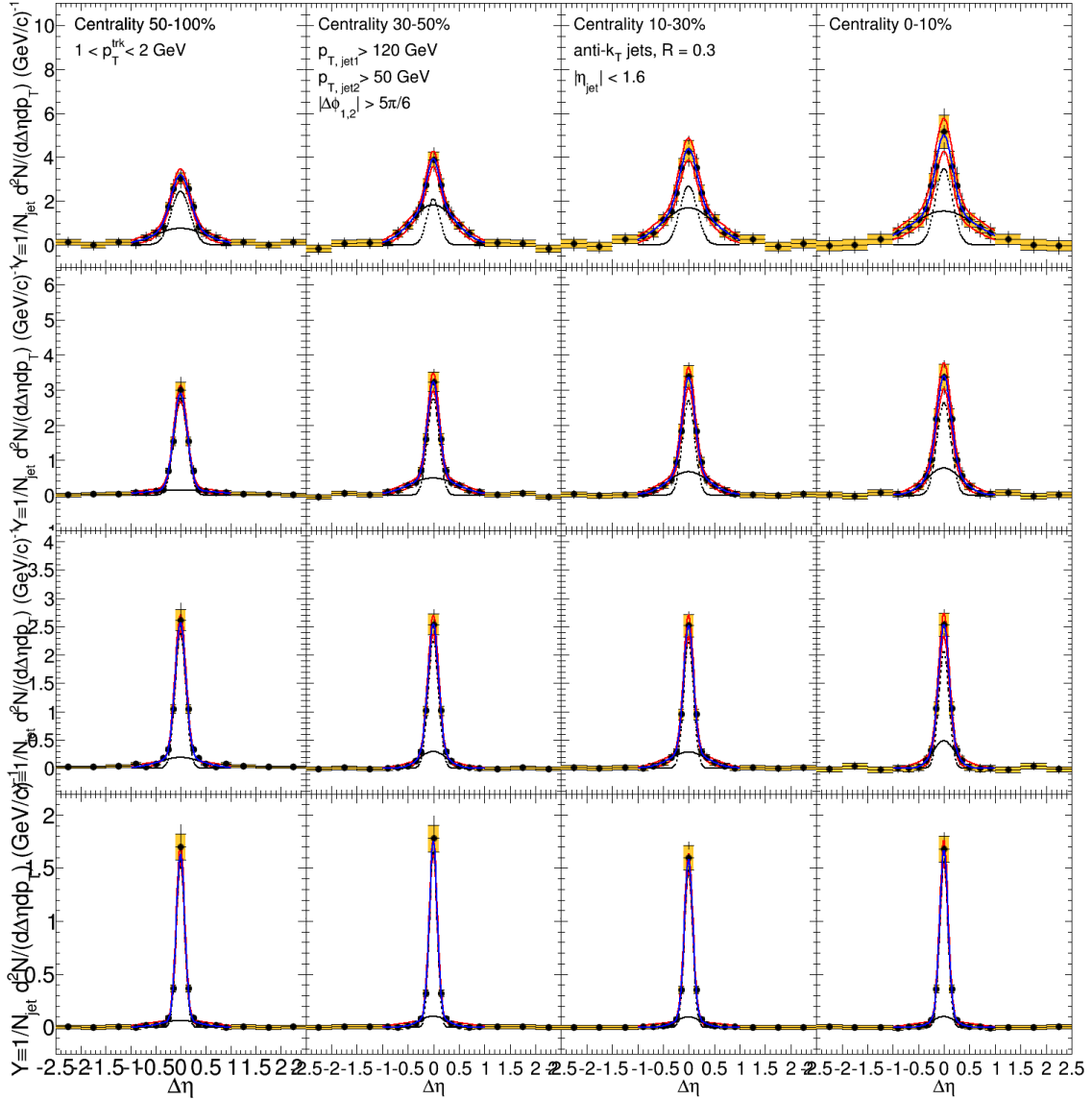


Figure 96. Illustration of the fits used to determine the distribution widths (shown here for leading jet PbPb $\Delta\eta$ correlations). Correlations are fit to a double gaussian (shown in blue, with black dashed lines indicating constituent gaussians), and width is taken as the $\Delta\eta$ value containing 67% of the total yield. Points are varied by their systematic errors and the fits are repeated (shown in red) to obtain the systematic error on the width.

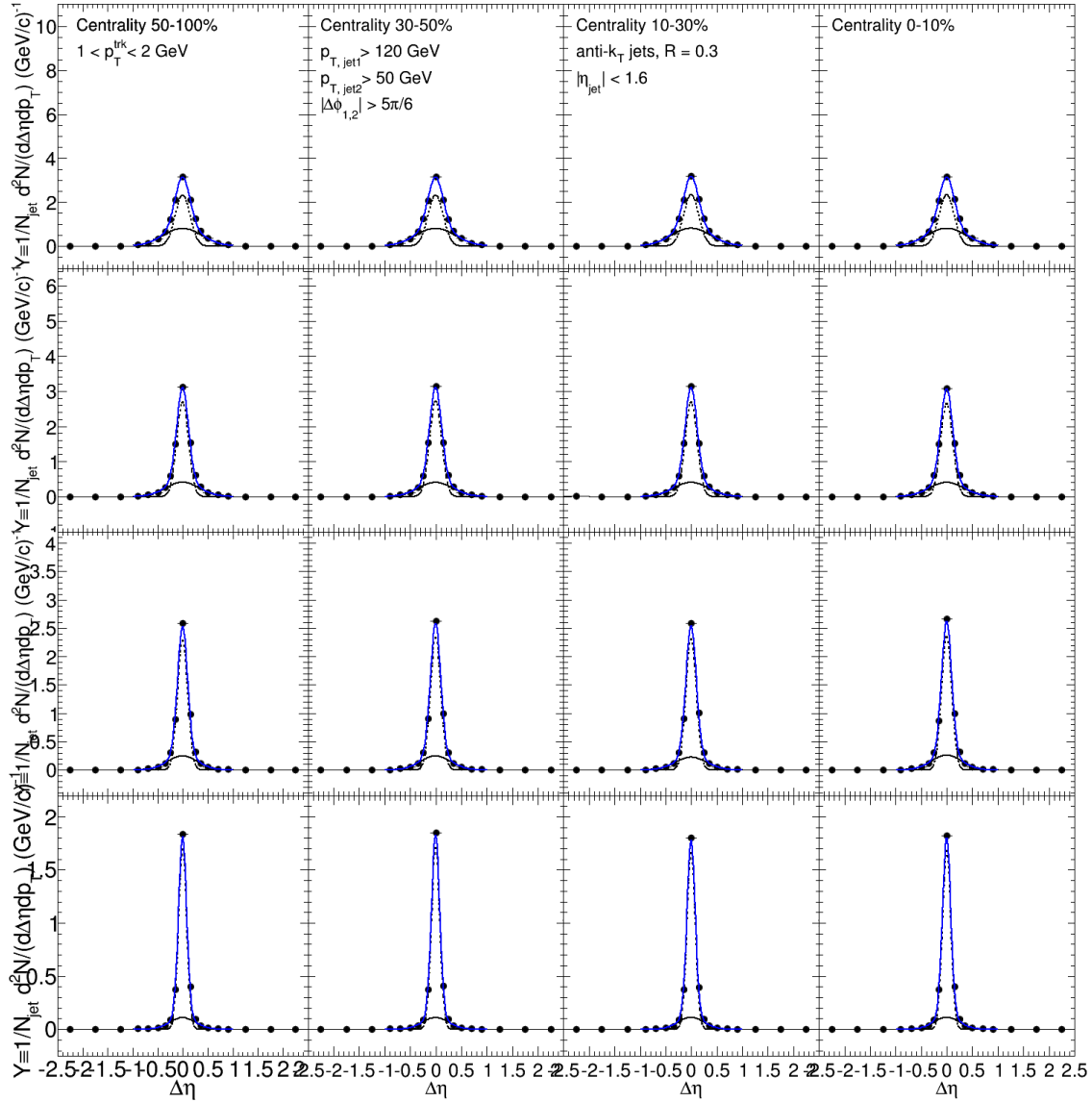


Figure 97. Illustration of the fits used to determine the distribution widths (shown here for leading jet pp $\Delta\eta$ correlations). Correlations are fit to a double gaussian (shown in blue, with black dashed lines indicating constituent gaussians), and width is taken as the $\Delta\eta$ value containing 67% of the total yield.

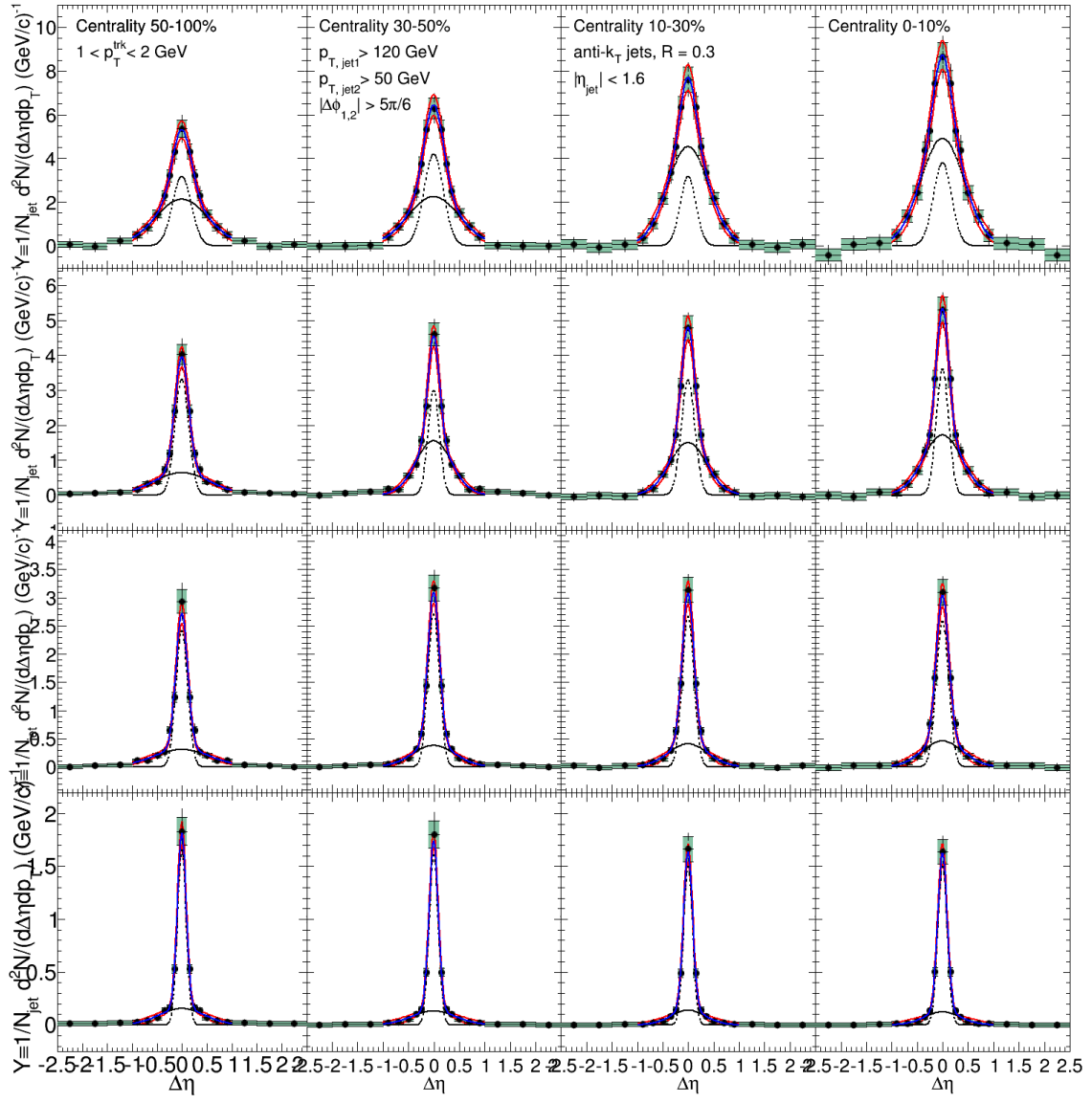


Figure 98. Illustration of the fits used to determine the distribution widths (shown here for sub-leading jet PbPb $\Delta\eta$ correlations). Correlations are fit to a double gaussian (shown in blue, with black dashed lines indicating constituent gaussians), and width is taken as the $\Delta\eta$ value containing 67% of the total yield. Points are varied by their systematic errors and the fits are repeated (shown in red) to obtain the systematic error on the width.

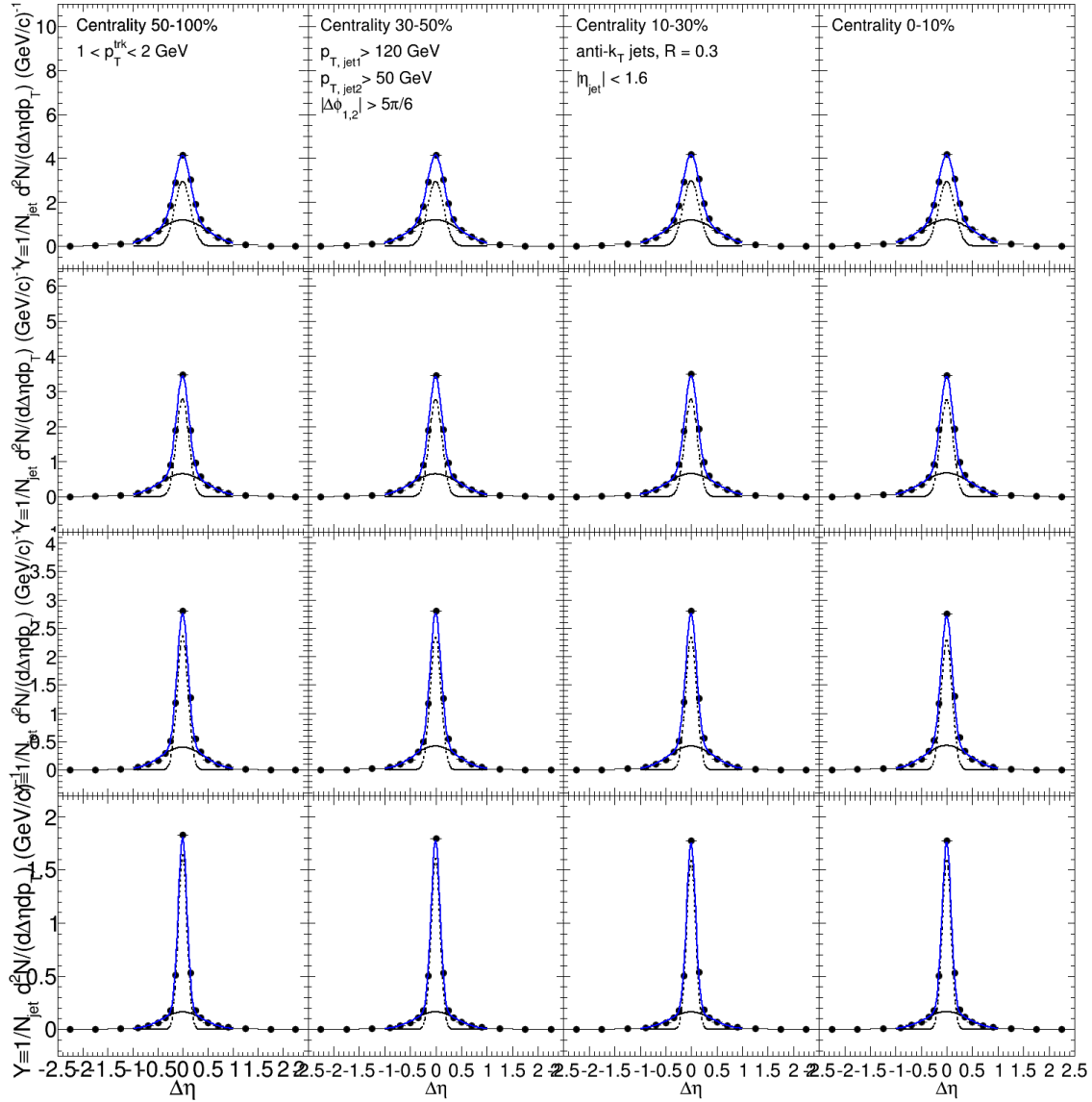


Figure 99. Illustration of the fits used to determine the distribution widths (shown here for sub-leading jet pp $\Delta\eta$ correlations). Correlations are fit to a double gaussian (shown in blue, with black dashed lines indicating constituent gaussians), and width is taken as the $\Delta\eta$ value containing 67% of the total yield.

VITA